NUMERICAL AND OPTICAL PERFORMANCE CHARACTERIZATION OF RANDOM ANTIREFLECTIVE SURFACE STRUCTURES ON DIFFRACTIVE OPTICAL ELEMENTS

by

Praneeth Gadamsetti

A dissertation submitted to the faculty of
The University of North Carolina at Charlotte
in partial fulfillment of the requirements
for the degree of Doctor of Philosophy in
Optical Science and Engineering

Charlotte

2023

Approved by:

_____
Dr. Menelaos Poutous

_____
Dr. Glenn Boreman

_____
Dr. Tino Hofmann

_____
Dr. Thomas Suleski

_____
Dr. Suzanne Boyd

ABSTRACT

PRANEETH GADAMSETTI. Numerical and Optical Performance Characterization of Random Antireflective Surface Structures on Diffractive Optical Elements. (Under the direction of DR. MENELAOS K. POUTOUS)

Antireflective structured surfaces (ARSS) are periodic, or random, distributions of three-dimensional nano-features fabricated directly on optical quality substrates, for the suppression of surface reflectivity from the dielectric boundary. Within the spectral band of efficient antireflective operation, the structures are sub-wavelength scale in cross-sectional diameter, and near-wavelength scale in height. As incident light passes from superstrate to substrate, the ARSS induce a synthetic index of refraction with a surface-average optical dielectric density, effectively matching the electromagnetic impedance on the surface separating the media, thus reducing Fresnel reflectivity. Published studies often model random ARSS as stratified homogenous dielectric layers, globally averaging the transverse feature distributions to a single optical index value per layer, and ignoring their distributed profiles.

In this work, the effects of pseudo-random deterministic transverse feature distributions within the ARSS and their antireflective properties were studied. Rigorous coupled wave analysis (RCWA) was used to compute the performance of periodic unit cell ARSS, superimposed on a binary-phase transmission grating as a function of the ARSS period, for TE and TM incident light polarization states, at normal angle of incidence. The results showed differences in performance between distinct ARSS distributions, despite their identical layer-averaged refractive index value. Sub-wavelength and near-wavelength scale unit-cell periodicities for ARSS with short autocorrelation lengths, show better overall anti-

reflectivity performance, compared to less complicated feature distributions with comparable effective-permittivity layers. Numerical simulations for specific randomly distributed ARSS features correlated with anti-reflective performance efficiencies.

In parallel, the fabrication process of random anti-reflective structures (rARSS) was optimized for fused silica optical flats, and then applied to deterministic phase-diffusing diffractive optical elements (DOE) to suppress Fresnel reflections. The goal of the effort was to examine the effects of rARSS application on existing optical components. Four commercially available DOE, a 2D spot array generator, a 1D spot array, a controlled-angle illumination diffuser, and a discrete-phase profile diffractive lens, were used to investigate the effects of rARSS on 3-dimensional segmented-phase topographies. Three diffractive diffusers were measured over the entire equatorial plane of incidence using a scatterometer, to determine changes from the original design illumination pattern due to the presence of rARSS beyond a simple transmission enhancement. The diffractive lens was measured using a power detector and a beam profiler to compare the focal spots before and after addition of rARSS in transmission and reflection. The tests verified significant reduction of Fresnel reflections by the rARSS on the surface of the DOE, without altering their original performance efficiency. Finally, the non-deterministic scatter effects due to inherent roughness of the rARSS on segmented phase profiles was characterized by comparing scatterometer measurements of optical flats and near-wavelength scale binary-phase gratings. It is shown that scatter effects because of rARSS presence on optical flats and binary-phase gratings were negligible, indicating rARSS can be applied as an effective anti-reflection treatment to pre-fabricated optical surfaces with complex topography without degrading their performance.

DEDICATION

This dissertation is dedicated to...

... my parents, who have always been, and continue to be, the most amazing role models. I would not have made it this far without their constant unconditional support and encouragement.

ACKNOWLEDGEMENTS

First and foremost, I would like to express my sincere gratitude to my advisor Dr. Menelaos Poutous for his continuous support for my Ph.D study. His guidance has immensely helped me throughout my research and writing of this dissertation. I am grateful for all the time and energy he has given to me in my time at UNC Charlotte and could not have imagined to have a better advisor and mentor for my Ph.D study.

Besides my advisor, I would like to thank the rest of my dissertation committee: Dr. Glenn Boreman, Dr. Tino Hofmann, Dr. Thomas Suleski and Dr. Suzanne Boyd, for their insightful comments and advice through the dissertation process. I greatly appreciate all of the time my committee has invested in me.

My sincere thanks for the Graduate assistantships funded by Nuspot Technologies LLC, Gamdan Optics Inc and Nanohmics Inc through a number of awards by DARPA, NSF and AFOSR for funding me during my graduate school career. I know that I am incredibly lucky to have been given such generous financial support and that without it completing this dissertation would have been much more difficult.

I would also like to thank the Center for Optoelectronics and Optical Communications for the use of its equipment and facilities. Thank you also to Mr. Scott Williams, Dr. Lou Deguzman, and Jeffery Thousand for their patient training sessions and frequent help with equipment issues.

Thank you to the past and the present members of the Optical Micro-structures Interfaces Laboratory, Karteek Kunala, David Gonzales, Uma Subhash, Subhasree Srinivas, Samir Paudel, Chris Wilson and Tom Hutchins, for all the training,

troubleshooting, brainstorming, and general support they have given me. I consider myself very lucky to have had such a supportive lab.

And finally, I am incredibly grateful to all my friends, and family for their continuous support and encouragement throughout this entire process. I would especially like to thank my parents for supporting me through writing this dissertation and my life in general. I truly could not have done this without you.

TABLE OF CONTENTS

LIST OF TABELS

LIST OF FIGURES

LIST OF ABBREVATIONS

ALD	Atomic layer deposition
AOI	Angle of incidence
ARS	Angle resolved scatter
BBAR	Broad band anti-reflection coating
BCl_3	Boron trichloride
BS	Beam splitter
BSDF	Bi-directional distribution function
C_4F_8	Octafluorocyclobutane
CHF_3	Trifluoromethane
CVD	Chemical vapor deposition
DDS	Deterministic design scatter
DOE	Diffractive optical element
EMT	Effective medium theory
GaAs	Gallium Arsenide
Ge	Germanium
GRIN	Gradient index profile
HWP	Half-waveplate
IBS	ion beam sputtering
ICP	Inductive coupled plasma
IEDO	Intensity equalized diffraction order
LP	Linear polarizer
MLAR	Multi-layer anti-reflection coating
NDDS	Near angle deterministic scatter
O_2	Oxygen
PAR	Perfect anti-reflection coating

PECVD	Plasma enhanced chemical vapor deposition
PVD	Physical vapor deposition
QQAR	Quarter-Quarter anti-reflection coating
rARSS	Random antireflection structured surface
RCWA	Rigorous coupled wave analysis
RF	Radio frequency
RIE	Reactive ion etching
SEM	Scanning electron microscope
SF_6	Sulfur hexafluoride
SLAR	Single layer anti-reflection coating
SWG	Subwavelength grating
TFAR	Thin film anti-reflection coating
WADS	Wide angle deterministic scatter
ZnS	Zinc sulphide

CHAPTER 1: INTRODUCTION

1.1 Methods of Anti-reflection

Light incident on smooth transparent surfaces experiences Fresnel reflections due to the discontinuity of the optical refractive index values at the interface. In various applications such as flat displays, photovoltaic devices, mobile screens and high-performance optical elements Fresnel reflections are undesired, and suppression of these reflections is required to increase the performance of the optical systems [1,2]. Thin film anti-reflection coatings (TFAR) are the most prominent technique used to suppress Fresnel reflections.

The simplest TFAR design is a Single-layer antireflection coating (SLAR) designed using materials of optical index preferably equal to the geometrical mean between the superstrate and substrate values ($\sqrt{n_s n_i}$), with a $m\lambda/4$ thickness (where m is an odd integer, and λ is the incident light wavelength). Reflected optical waves from the top and bottom surfaces of the thin film are phase matched to a difference of π, resulting in destructive interference between them as shown in Figure 1(a) [3,4]. Due to the fixed optical path length of SLAR films, satisfying the destructive interference conditions, these coatings are wave-band limited. Multilayer antireflective coatings (MLAR) are an alternative solution opted when the appropriate refractive index are not available and due to design flexibility can be engineered to have a better performance with respect to wider bandwidths and efficiencies when compared to SLAR as shown in Figure 2 (a). Changes in the optical path length of SLAR due to varying angle of incidence (AOI) effects the interference condition between the surfaces of the thin films and boundary conditions

making them inefficient at higher incidence angles (Equation 1) and sensitive to incident polarization as shown in Figure 2(b) [5].

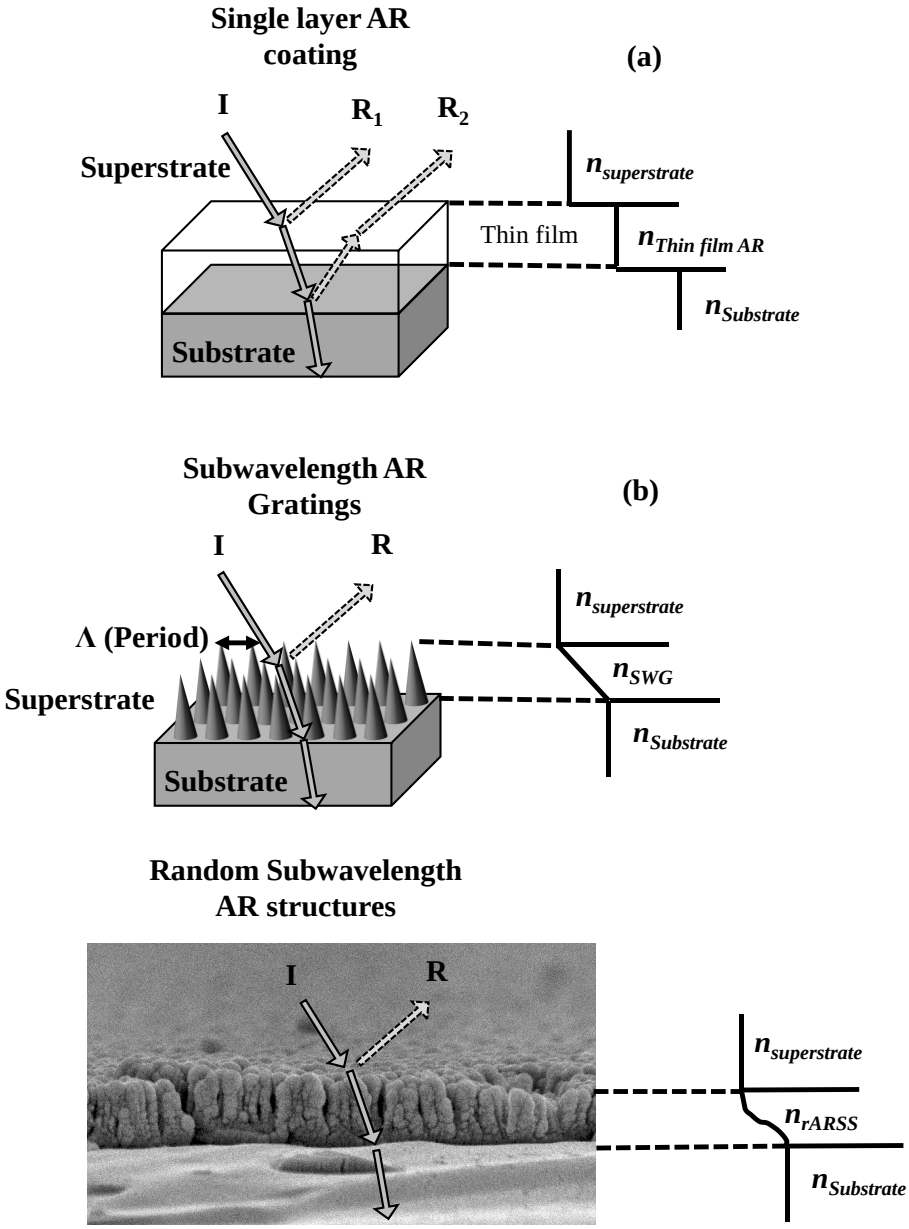

Figure 1 : Optical index variation from superstrate to substrate of three different antireflective surfaces. (a) Single layer AR coating, (b) Sub-wavelength AR gratings and (c) Random sub-wavelength structures.

$$T = 1 - \frac{(1-r^2)^2}{(1-r^2)^2 + 4r^2 sin(kd)^2} \quad (1)$$

In the above equation, r is the Fresnel reflection coefficient, k is the wavevector with in the thin film and $d = d_0 cos\theta$ is the thickness as a function of AOI.

An alternative to TFAR coatings is inhomogeneous film layers with gradient index profile (GRIN), which transition the optical index value gradually and monotonically from superstrate to that of substrate resulting in the suppression of the Fresnel reflections [6]. Although MLAR and GRIN coatings are desired for their superior performance, their fabrication and application on the optical surfaces can be complicated due to large number of layer deposition steps.

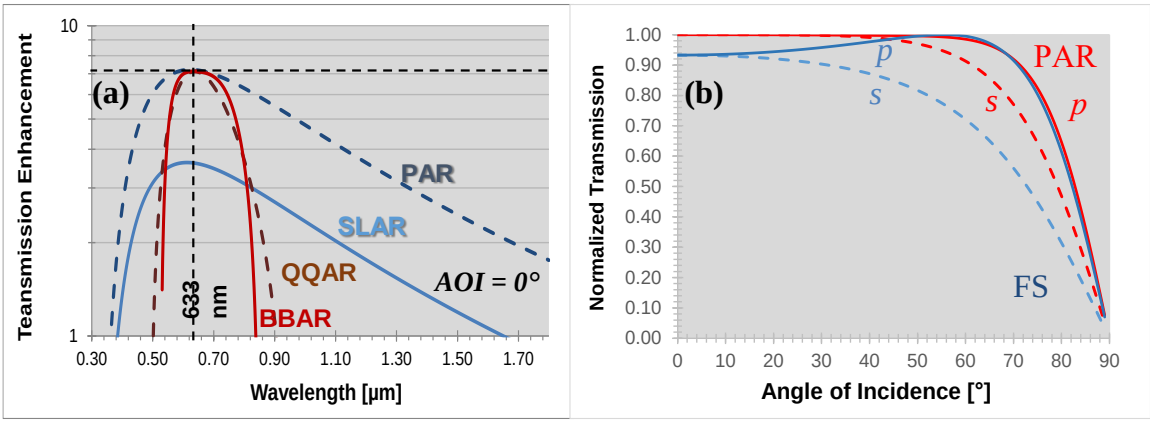

Figure 2 : Simulated transmission of AR thin film coatings. (a) Transmission enhancement of Anti-reflective thin film coatings comparing Perfect anti-reflective coating (PAR), Single layer anti-reflective coating (SLAR), Quarter-Quarter anti-reflective coating (QQAR) and Broad band anti-reflective coating (BBAR) at normal angle of incidence (AOI = 0º) for 633nm, (b) Normalized transmission as a function of angle of incidence for fused silica (FS) blank in comparison to PAR for S and P polarizations.

Periodic sub-wavelength gratings (SWG) are another solution to suppression of Fresnel reflections, fabricated on the substrate surface as shown in Figure 1(b). For incident

wavelengths longer than the spatial periods of the grating (Λ), only 0th diffracted order is non-evanescent in both transmission and reflection with all higher orders becoming evanescent, as evident by the grating equation (Equation 2) [7-9]. Optimizing the height of the grating to $\lambda/4n$, would result in a phase difference of π between the reflected orders leading to suppression of reflection, and specular transmission enhancement, a result similar to anti-reflective (AR) coatings. For incident wavelengths smaller than the gratings spatial period as shown in Figure 3(a), where the spatial period of the linear grating is fixed at 500nm the higher diffracted orders propagate, and the AR functionality of SWG does not manifest. SWG with dissimilar periods in the orthogonal transverse spatial axis leads to form birefringence, making the device dependent on the incident polarization state and AOI, although they have higher AOI acceptance compared to the AR thin film coatings as shown in Figure 3(b).

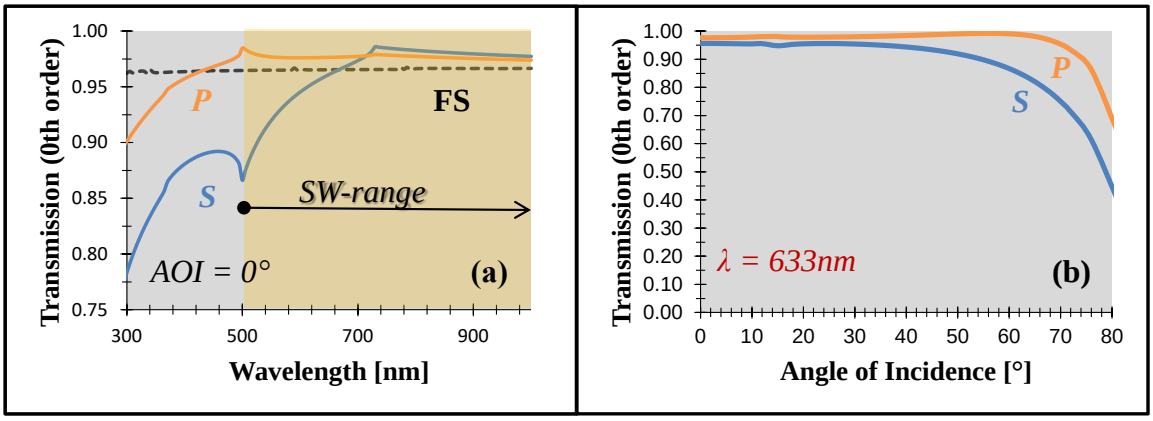

Figure 3 : Simulated 0th order transmission of 500nm period linear SWG on Fused silica. (a) 0th order transmission as a function of wavelength at normal angle of incidence (AOI = 0^{o}) for a wavelength range of 0.3µm to 1.0µm, (b) 0th order transmission as a function of angle of incidence at 633nm for S and P polarizations.

$$sin\theta_m - sin\theta_i = m(\lambda/\Lambda). \quad (2)$$

In the grating equation, θ_i is the angle of incidence, θ_m is the angle of m^{th} propagating order, λ is the incident wavelength and Λ is the period of the grating.

Random antireflective structured surfaces (rARSS) which are the focus of this dissertation are a different solution with densely packed non-periodic, sub-wavelength features fabricated on the substrate's surface, as shown in Figure 1(c). rARSS are usually modelled as an effective medium, using a multi-layered optical index stratified model, thereby simulating the reduction of reflection loses and increasing transmission through the substrate [10]. The depth and random distribution of these surface structures would define the range of broadband anti-reflection properties as shown in the Figure 4(a) with a maximum at 715nm. Reports have shown that the range of wavelengths of enhancement can be shifted to longer wavelengths by increasing their depth [11]. The transmission intensity of rARSS on fused silica substrate as a function of AOI at 633nm shows high

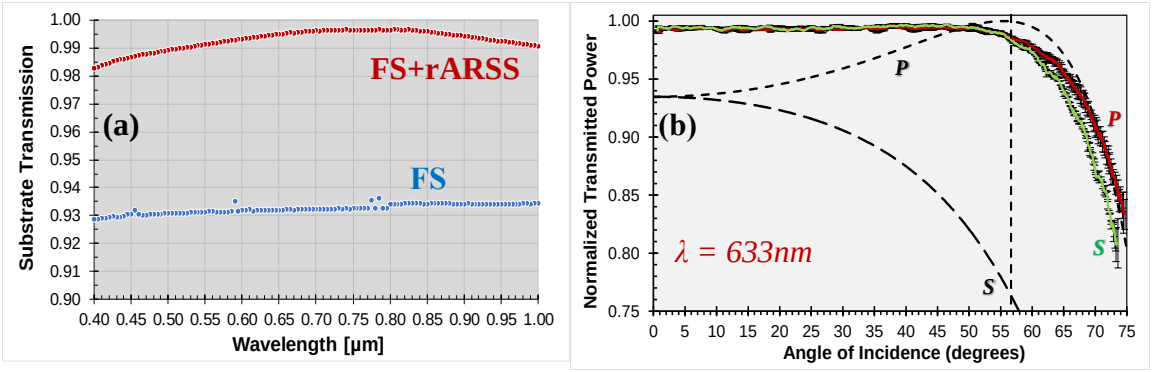

Figure 4 : Measured transmission of double-sided rARSS treatment on fused silica window. (a) Transmission as a function of wavelength at normal angle of incidence (AOI = 0º) for a wavelength range of 0.4µm to 1.0µm, (b) Transmission as a function of AOI for both incident light polarization states at an incident wavelength of 633 nm.

transmission to about Brewster's angle (55º) independent of incident polarization as shown in the Figure 4(b) [12, 13]. This polarization insensitivity observed at high AOI is unique to the rARSS due to their random distribution, where as SLAR and SWG shown a difference in their performance for S and P polarizations at about 30º AOI.

1.2 Fabrication techniques of anti-reflective subwavelength structures

Random antireflective structured surfaces (rARSS) are fabricated differently than the periodic SWG. Periodic SWG are fabricated through application of lithography techniques, where the substrate is initially coated with a photosensitive polymer (photoresist) and an image of periodic geometry is exposed on to the masking layer using contact or non-contact lithography methods. The exposed photoresist is stripped using a developer to create a photoresist mask (positive process). The resist lithograph is then further etched to transfer the pattern into the surfaces of the substrate, followed by a resist stripping step where

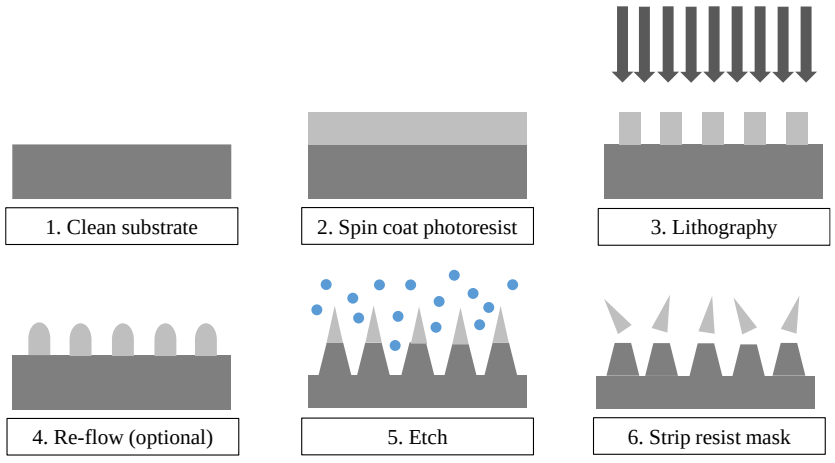

Figure 5 : Schematic depicting common fabrication steps for periodic surface structures onto a substrate. It should be noted the step 3 can be interference, conventional or, direct-write lithography.

remaining resist is stripped off, leaving behind a periodic SWG as shown in Figure 5 [14, 15].

In literature various methods for fabricating rARSS are reported, which can be grouped into two major categories: top down and bottom up fabrication methods [3]. The bottom-up fabrication methods involve growing cross-sectional nanoscale pillars or porous layers directly on to the substrate's surface, which is achieved using different techniques such as solution processing and physical or chemical vapor deposition (CVD) [16-18]. Top-down methods unlike bottom up methods use dry etching or wet etching to fabricate the structures into the substrate.

This dissertation focuses on the Top down fabrication of rARSS using dry etching. Dry etching or plasma etching is a commonly used method, in conjunction with a masking step, to fabricate periodic or random structures on optical substrate surface. Reactive Ion Etching (RIE) is a type of plasma etching that requires a chamber with two electrodes, powered by a radio-frequency (RF) power supply. The substrate which is going to be etched is placed on the bottom electrode (Cathode) of the chamber, which is evacuated to 10^{-6} Torr, followed by the introduction of small amounts of reactive gases, to achieve a desired pressure inside the chamber, usually in the order of tens of millitorr. The mixture of gases are chosen based on their affinity towards the specific substrate. For substrates such as silicon, typically Fluorine or Chlorine-based gases are used, such as: Sulfur Hexafluoride (SF_6), Octafluorocyclobutane (C_4F_8), Trifluoromethane (CHF_3), or Boron Trichloride (BCl_3), with a mixture of oxygen (O_2) in most cases. When the RF power supply is turned on, the plasma is ignited ripping electrons off the gas molecules, causing multiple collisions between the molecules and the electrons, leading to separation of neutral reactive radicals,

positive ions and electrons. All these chemical species due to the voltage difference between the electrodes are directed perpendicularly towards the surface of the substrate to interact [19, 20]. Above the surface of the samples the elements in the gas molecules that do not interact will remain in the plasma and eventually will be removed from the chamber by the outgoing gas flow. The neutral radicals diffuse through the plasma and eventually reach the surface of the sample. This can result in two possible interactions: a) the neutral radicals impede the etching process or, b) spontaneously react with the material and desorb into a volatile product, that is eventually removed from the chamber though the outgoing gas flow.

The RIE process is highly anisotropic in comparison to wet etching, due to the directed flow of positive ions in the plasma to the surface of the substrate, caused by the voltage difference between them. The flowing positive ions bombard the surface and can result in sputtering the surface of the substrate through the transfer of momentum, or provide the energy needed to allow the neutral radicals to react with the surface of the substrate. The promotions of the reactions between the radicals and the substrate is called ion-etching. This process in general is faster than spontaneous reactions and does not result in redisposition on the surface. There are multiple variables that can be used to achieve desired etch results, such as chamber pressure, bias power, gas composition, flow rates, temperature of the substrate and etch time [21, 22].

Fabrication of rARSS using top-down methods can be divided into three major categories. The first method requires an initial metallization masking step, in which a thin discontinuous layer of metal (such as gold) is deposited on to the substrate, followed by plasma etch to fabricate randomly distributed nanostructures on to the substrate as shown

in Figure 6. Another variant to this technique is to deposit a dialectic layer and overcoat with a metal layer. This metal layer is then thermally annealed and followed by plasma etch [23]. A second method utilizes active masking, where a two-cycle plasma etch is used. The 2-cycle plasma etch incorporates an etching step and a passivation step, where a polymer layer is allowed to grow on top of the substrate surface effectively creating its own mask [24]. The third method involves etching a bare substrate with reactive ion etching (RIE), with or without inductively coupled plasma (ICP) etching process. Fabrication of rARSS has been reported on borosilicate glass, fused silica, plastic and silicon for visible wavelengths and Zinc Sulphide (ZnS or Zerodur), Germanium (Ge) and Gallium Arsenide (GaAs) for near and far infrared wavelengths [11, 25-26]. In this dissertation fabrication of the rARSS has been restricted to the first method due to the choice of substrates, the application wavelength band, and its simplicity.

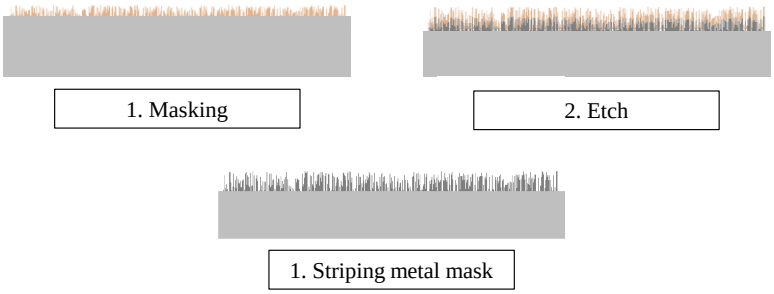

Figure 6 : Schematic of rARSS fabrication process used in this dissertation using reactive ion etching (RIE).

1.3 Characterization of anti-reflective structured surfaces on optical phase elements

As many experimental techniques have been reported in the literature to quantify the anti-reflective properties of subwavelength structured surfaces periodic or random, of which transmission measurements over a range of wavelengths for varying AOI and

polarizations states are the most common. These measurements are important because they can validate the anti-reflective properties of the subwavelength structured surfaces, as an increase in the specular transmission power throughput, which in turn implies a reduction in the reflection. Reflection measurements alone on the other hand are not conclusive, as reduction in reflection can be a result of increase in specular transmission or increase in scattered light, which could be detrimental for most applications [27]. For applications of rARSS on optical components with curved surfaces, such as lenses, or segmented phase profiles, such as gratings, rather than optical flat windows, it is important to study the effects of rARSS on the optical functional performance of the components as well. For lenses these are focusing parameters, aberrations, and diffraction-limited spot sizes, and for gratings are diffracted-order efficiency distributions and angular separation.

Previous work done by the members of our lab have shown rARSS are not limited to planar substrates, and can also applied to continuous and segmented phase profiles of optical elements as shown in the Figure 7. Through transmission measurements in the axial direction, broadband transmission enhancement properties, transmission enhancement for variable AOI, and polarization insensitivity at higher AOI for optical windows, were demonstrated [12, 13]. In Dr. C. Taylor's dissertation, fabrication of rARSS on 1-inch diameter lenses and detailed analysis on the effects of rARSS on curved surfaces was presented [28-30]. The work done by Dr. A. Peltier-Eckert was an extension of previous work on lenses, concentrated on fabrication of rARSS on microlens arrays (MLA), with a thorough study on the effects of rARSS on MLA beam profiles [31]. Dr. K. Kunala's work on the other hand was focused on segmented phase profiles, such as near-wavelength gratings, completely characterizing the variations in transmission and reflection

performance for varying AOI, at multiple wavelengths, due to the presence of rARSS [32,33].

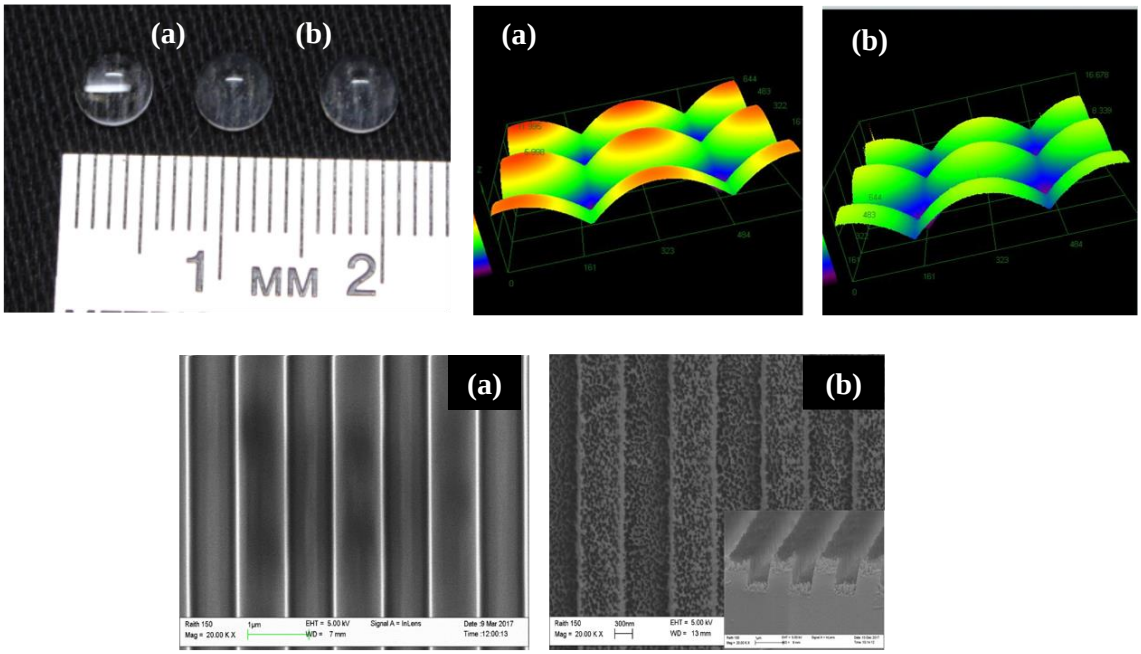

Figure 7 : (a) Unprocessed and (b) rARSS-processed. (Top-left) 5mm diameter lenses, (Top-right) 300µm diameter micro lenses and (Bottom) 1.595µm period gratings.

Computer generated diffractive optical elements (DOE) like spot array generators, beam shapers and controlled angle illuminators as shown in Figure 8 have various applications like multi-focal microscopy, multiple coherent splitting or recombination, and

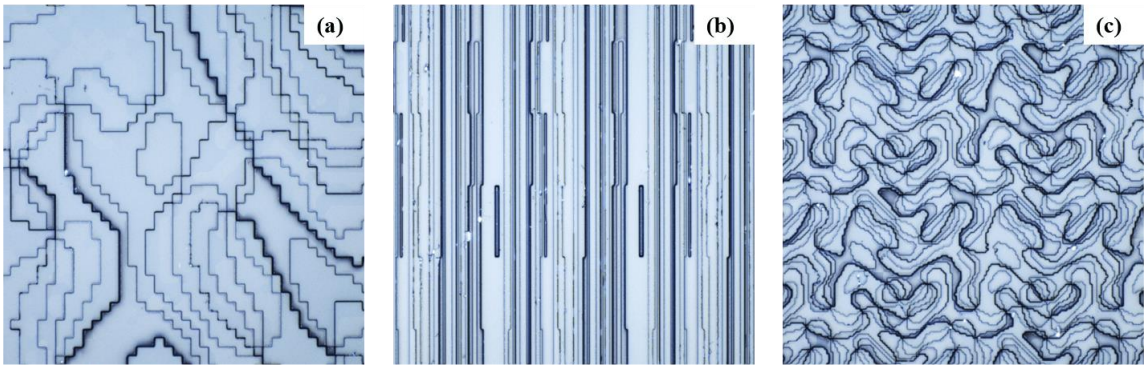

Figure 8 : Various diffractive optical elements: (a) 2-Dimentional Spot array generator and (b) 1-Dimentional Spot array generator and (c) Controlled angle diffuser.

camera calibration for imaging and sensing [34, 35]. The use of DOE is becoming more and more common in various optical systems and they also suffer from performance degradation because of the optical feedback from front and back surfaces due to Fresnel reflections.

Suppression of reflections from DOE surfaces can be achieved by implementing thin film coatings by a variety of deposition techniques, such as: ion-beam sputtering (IBS), atomic layer deposition (ALD) [36-38], layer by layer assembly [39], plasma-enhanced chemical vapor deposition (PECVD) or physical vapor deposition (PVD) [40, 41]. The coatings vary from conformal to non-conformal depending on implemented techniques such as atomic layer deposition or physical vapor deposition, shown in Figure 9. Compared to simple phase optics, coating DOE with complex multi-phase level topographies is challenging and to function as intended, the coatings must be included in their original design specifications, further increasing the complexity of designs and fabrication steps.

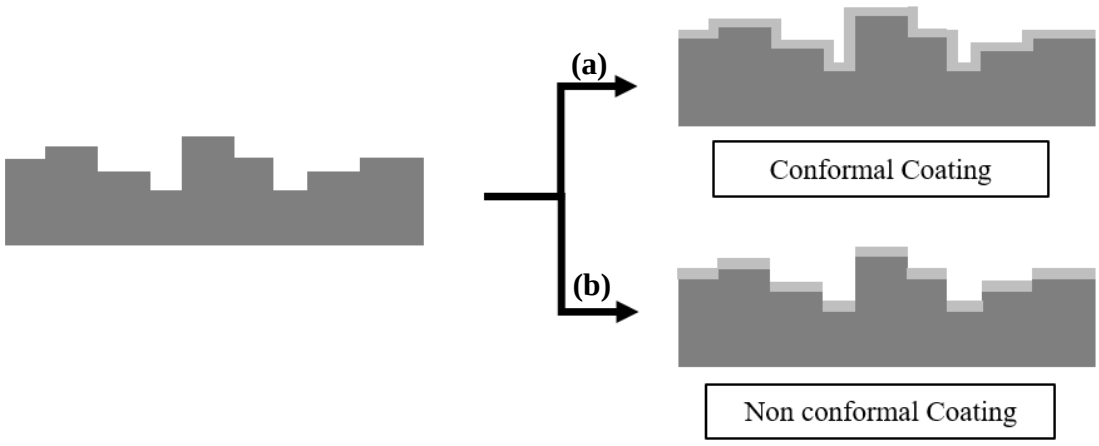

Figure 9 : Graphical depiction of AR-thin film deposition techniques: (a) Conformal AR coating and (b) Non-conformal AR coating.

To-date no studies were found in the literature describing the application of periodic or random structured surfaces as an AR treatment on complex multiple-phase level DOE. Few reports are available in literature on the application of periodic subwavelength nanostructures (tapered or regular cones) on the microscale diffractive grating surfaces [42]. While they were able to successfully demonstrate the suppression in reflection and enhancement of transmission with periodic subwavelength nanostructures, the fabrication process of these periodic AR structures integrated on a simple DOE such as diffractive gratings involve multiple steps and much harder to realize such AR structures on a multi-phase level DOE's with complex topographies. Random nanostructured surfaces on prefabricated binary gratings, have successfully demonstrated reduction in Fresnel reflectivity without perturbing their performance and can be a potential solution as effective AR treatment for complicated phase-profile DOE.

In order to establish rARSS as an effective method to suppress reflections, the performance of the DOE should remain unaltered after the addition of rARSS. Unlike simple optical elements (lenses), the performance of DOE cannot be characterized by total transmitted power efficiency using a single photodiode sensor or beam profiler measurements. In this dissertation a scatterometer was used, with a large dynamic detection range at a wavelength of 633nm, to measure the Angle Resolved Scatter (ARS) in transmission and reflection. This was done to completely quantify any variations in the far-field diffraction intensity distributions of the DOE, and the presence of non-deterministic scatter due to the fabrication of rARSS on the prefabricated DOE surface profile. To quantify the dimensions of the structures on the surface, a UV confocal microscope and profilometry was used, to measure the bearing curve and nano-structure heights, using

parameters such as rms roughness (R_z), to analyze variations in the gradient optical index with varying surface topography and compared the results with similar measurements on flat substrates.

Finally, it is important to study surface feature distributions of the rARSS in the transverse plane, and relate their effects on surface transmission properties. The random subwavelength structures have extremely small geometric cross-sectional dimensions (diameters from 50 to 100 nm), well below the resolution limits of profilometric and microscope measurements. To analyze the transverse feature distributions, high resolution scanning electron microscope (SEM) images of the processed surfaces were taken and analyzed using granulometry. Granulometry is a technique, which uses numerical image processing such as erosion and dilation, opening and top-hat transforms, to identify transverse-feature boundaries in top-down SEM images [43]. Predefined scaled structure features, along with image filtering techniques such as salt and pepper filtering, ASF (Alternative Sequential Filtering) remove instrument noise from SEM images. Using this technique top-down SEM images can be scanned to group physical nanostructures crossections into similar size groupings and yielding statistics of surface transverse feature dimensions.

1.4 Dissertation Overview

This dissertation broadly focuses on the application of random antireflective structured surfaces (rARSS) on functional diffractive optical elements and their optical performance characterization. Chapter 2 presents a numerical study on the transverse feature distributions effects on their performance of anti-reflective structured surfaces on a

functional diffractive element such as binary gratings. This chapter is divided into two sections, starting with the design of the 1-dimensional anti-reflective periodic subwavelength structured surfaces using Effective Medium Theory (EMT) for both TE and TM polarizations and a collection of transverse feature distributions of comparable parameters to the theoretical prediction were chosen with varying complexity for the study. To investigate the effects of the surface feature distributions on their AR performance independent of other variables the depth of the structures is restricted to a quarter of the incident wavelength. In the second section of this chapter, to analyze and quantify the effects of these structures on a functional diffractive gratings rigorous coupled wave analysis (RCWA) are computed, followed by 2D propagation simulations to understand the energy distributions within the AR structured surfaces.

Chapter 3 expands on the work done previously reported by our group on application of rARSS on optical elements like lenses and gratings to multiphase level deterministic diffractive optical elements (DOE), such as light diffusers. This chapter focuses on characterizing the optical performance of four commercially available fused silica DOE, with rARSS fabricated on them using a process initially optimized for optical windows. The fabricated rARSS on the DOE were characterized using their scanning electron micrographs to study the differences and the effects of the etching process on the surface topography of the DOE pre and post fabrication.

Optical performance of the DOE generated using algorithms unlike simple optical elements such as lenses and gratings are difficult to characterize due to their complex illumination distributions. To study the differences in their optical performance pre and post fabrication of rARSS on both the surfaces, the DOE were tested using a scatterometer,

where the intensity distributions were measured for the normal angle of incidence along the equatorial planes at 633nm incident wavelength in transmission and reflection. Diffractive lenses unlike the rest of the DOE can also function at wavelengths other than the wavelength they are designed for, and to observe the differences in their performances the diffractive lens was tested before and after fabrication of rARSS using a multi-wavelength He-Ne laser. The surfaces are then characterized using granulometry, to observe the differences in rARSS distributions because of varying surface topographies of DOE.

While the rARSS act as AR structures, the nano-scaled transverse cross-sections of these structures may result in increase of uniform non-deterministic scatter, which can be determinantal to the performance of optical elements with rARSS overwhelming any AR benefits due to suppression of Fresnel reflections. To investigate the presence of non-deterministic scatter and its effects, Bi-directional distributions function (BSDF) of optical windows and near wavelength binary gratings were measured and analyzed pre and post fabrication at various angles of incidence.

Chapter 4 of this dissertation contains the final conclusions drawn from the work presented in Chapters 2 and 3. It also discusses potential future work that could be explored to expand on the work presented.

CHAPTER 2: NUMERICAL STUDY OF FEATURE-DISTRIBUTION EFFECTS FOR ANTI-REFLECTION STRUCTURED SURFACES ON BINARY GRATINGS

2.1 Introduction

In this chapter, the effects of feature distributions on the anti-reflection properties of nanoscale structured surfaces, added anisotropically on the profile of a diffractive grating is studied using numerical simulations. In section 2.2, the numerical experiment and the motivation to study the effects of transverse feature distributions using pseudo-random transverse distributions of anti-reflective structured surfaces (ARSS) are discussed. In section 2.3, 1-D period subwavelength gratings were modelled using Effective Medium Theory (EMT) as the starting point. Since random anti-reflective structured surfaces (rARSS) cannot be exactly numerically modeled. Periodic deterministic profiles with pseudo-random feature distributions within the unit cell, such as Dammann gratings, are used as a transition from regular (periodic) phase distributions to quasi-random ones. To methodically control the numerical experiment, Dammann gratings with increasing unit cell complexity, and fill fractions comparable to EMT predicted values, were chosen for both incident light polarization states.

In section 2.4, antireflection performance of selected deterministic distribution designs for ARSS surfaces, superimposed on a baseline binary grating, are presented for 633nm incident wavelength at normal angle of incidence. The deterministic ARSS designs are “surrogate” trial phase-profiles, with increasing feature distribution complexity, to bridge across simple designs to randomized distribution designs. The numerical results are computed using rigorous coupled wave analysis (RCWA). The simulations used 1-D

gratings (linear) because of the overwhelming computational load related to the fine spatial sampling requirement. Since the linear gratings are sensitive to the incident light polarization, the performance as function of polarization is also discussed. Finally, changes in the normalized angular intensity spectrum of the baseline gratings, due to the presence of ARSS, are discussed along with wave propagation simulation results.

Section 2.5, presents the conclusions of the effects of the trial transverse-feature ARSS distributions and their antireflective performance on the functional baseline diffractive element.

2.2 Motivation

As mentioned in Chapter 1, a thin film AR coating (TFAR) is one of the most prominent techniques used to suppress Fresnel reflections from optical surfaces [1-4]. Antireflective structured surfaces (ARSS) periodic or random have been studied extensively during the last two decades as a practical alternative to conventional TFAR, especially in wavelength bands where well-matched optical refractive index materials are unavailable.

Random distributions of nanostructures forming rARSS are often modelled as homogeneous stratified dielectric gradient optical index (GRIN) layers, globally averaging the distributed transverse features to a single optical index fill-factor for each constitute layer [9]. This is a direct consequence of the layered effective medium approximation, which results in loss of continuity between the GRIN layers for some models. The simplest design of the periodic anti-reflective structured surfaces (ARSS) is a binary-phase transmission grating, with spatial period smaller than the minimum of the desired

wavelength band, commonly referred to as a sub-wavelength grating (SWG). Adhering to SLAR thin-film index and thickness design conditions, predicted by effective medium theory (EMT) as shown in Figure 10(b) [7-9], the nanostructured surface "layer" is approximated as having the effect of the equivalent SLAR coating, as shown in Figure 10(a). This greatly simplified methodology is followed by numerical optimization simulations, using a variety of algorithms such as rigorous coupled-wave analysis (RCWA) or finite-element propagation to achieve the desired AR effect [44, 45].

Expanding ARSS design beyond planar substrates becomes more computationally challenging, as the AR-inducing SWG must be applied anisotropically over the underlying substrate's morphology. For example, adding ARSS to the surface of binary gratings yields complicated bi-periodic feature layers, multiplexing the diffractive performance of the SWG-ARSS to the baseline grating performance, as shown in Figure 10. The empirical design rule is to decrease the subwavelength ARSS spatial period (p_x) enough, to yield an increase in AR effect and reduce any perturbations in the baseline grating performance. This approach has practical fabrication limitations, due to challenging critical dimensions for the AR-SWG, and because of the increased numerical simulation complexity, which renders the model computationally intense, especially for two-dimensional SWG.

There is a gap in the understanding of the effects of transverse feature distributions on AR performance for randomly distributed ARSS to periodic SWG-ARSS. Randomness in the nanoscale features of ARSS are usually analyzed using autocorrelations between their optical surface profiles. ARSS are rough in nature compared to optically smooth thin film coatings, and roughness of these structured surfaces can be analyzed using various available optical scattering models. In most scatter model's, randomly distributed surface

features are approximated by a collection of sinusoidal gratings and the AR-surfaces are modeled by linear superposition of their spatial frequencies. This is based on scale approximations, to relate surface roughness and the incident light wavelength dimensions. However, scatter models predict off-axis scatter and not the axial "alignment" of propagation radiation as shown in Figure 11(b) [46-48]. As, such scatter calculations are subtractive and cannot overcome Fresnel losses, due to the change in the optical index when the incident light transitions from ambient to substrate and vice versa. Approaching the scaling problem of random ARSS using the EMT method is not providing a transition model to scatter either [7-9]. The global averaging of the effective index, within the

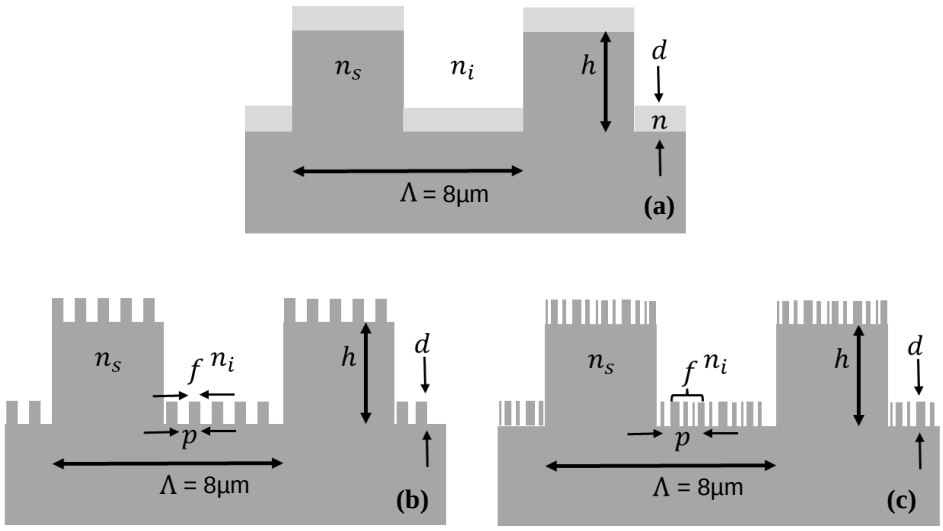

Figure 10 : Graphical depiction of cross sections from three types of surface structures used as AR treatments on a diffractive device. In all cases, a linear phase grating with spatial period $\boldsymbol{\Lambda_x}$ and π-phase depth h is used as the baseline optical surface, the indices are $\boldsymbol{n_i}$ for ambient and $\boldsymbol{n_s}$ for the substrate. (a) Surface crossection with an SLAR of index $\boldsymbol{n}$ and thickness $\boldsymbol{d}$ anisotropically applied to the grating surfaces. (b) A sub-scale periodic grating $\boldsymbol{p_x}$ with fill-factor $\boldsymbol{f}$, multiplexed ten-times across each period $\boldsymbol{\Lambda_x}$, acting as an AR-structure. (c) The AR-structure replaced by a distributed-feature periodic grating, with the same multiplex factor and fill-factor as (b).

transitional layer's as shown in Figure 11 (a), is not sensitive to feature distributions and does not predict scatter. Although the EMT model can overcome Fresnel loses by the directional interference of the wavefront, it has no mechanism to direct light off the axial direction. There is absence of a transitional model, which takes into account the two-dimensional spatial redistribution of features within a chosen unit cell for a given layer effective medium choice.

To investigate the AR and scatter functionality of transitional redistribution of phase nanostructures, from periodic SWG ARSS to quasi-randomized features on a pre-patterned substrate surface, a baseline 50% duty cycle, binary π-phase grating with $h = \lambda_{\circ}/2(n_s - n_i)$ was chosen, onto which ARSS profiles are anisotropically superimposed, to act as antireflective structures. We used two classes of ARSS: conventional, binary single-phase-transition gratings, based on EMT fill-factor requirements (B-series) and a selection of Dammann gratings of various orders (D-series). Dammann gratings are pseudorandom binary grating profiles, with varying optical densities within their spatial-period unit cell,

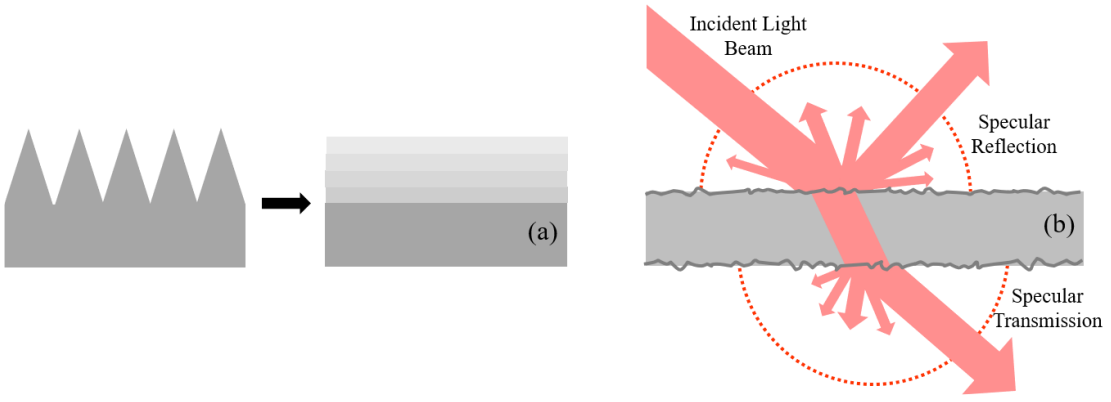

Figure 11 : Graphical depiction of (a) GRIN-EMT approximation of antireflective structured surface (ARSS) and (b) Scatter from optically transparent substrate with rough surface.

designed to generate equal intensity multiple diffraction orders for periods larger than the incident wavelength. As such, Dammann gratings have deterministic profiles based on specific selection rules, which allows a methodical study of optical cross-coupling effects, due to their ARSS periodicities multiplexed on the baseline grating.

In this study, Dammann gratings with increasing feature-distribution complexity and comparable EMT fill-fractions are multiplexed on the baseline binary grating, and their AR performance efficiency is computed using RCWA. The choice of a 50% duty-cycle, π-phase baseline grating, is based on its simplicity and segregation of the resulting angular intensity spectrum. For all incident wavelengths smaller than the baseline grating's spatial period, there will be even and odd propagating diffraction orders. However, the baseline gratings profile choice distributes energy efficiently only to the odd diffraction orders, suppressing the even orders by about two-orders of magnitude as shown in Figure 12. This selection rule allows for segregation of the transmitted intensity spatial distribution to: controlled angles (from the odd orders) and scatter (from the even orders).

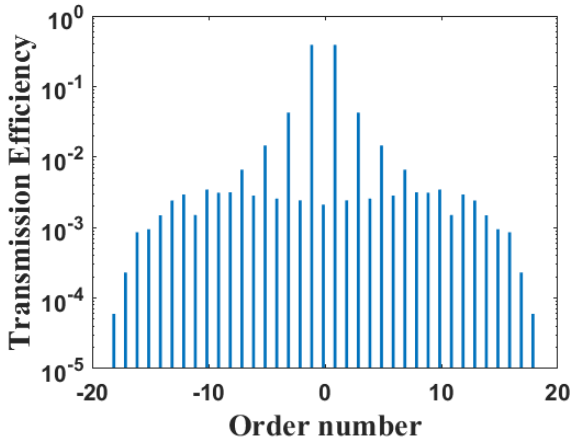

Figure 12 : RCWA-simulations of propagating diffraction order efficiencies for a fused silica baseline grating ($\Lambda_x = 8.00\mu m$, and $h = \lambda_\circ/2(n-1)$).

To illustrate the effects of multiplexing an ARSS SWG on the large period baseline grating. Binary SWG fulfilling the 0^{th}-order EMT criteria with a single-phase transition boundary (represented as B-0), is directly compared the numerical results of a Dammann grating (represented as D-21) that has the same EMT criteria. In Figure 13, the baseline grating even-order suppression averages at a normalized intensity level of $2(10^{-3})$, shown by the blue bars, while the controlled normalized intensity peaks for the ±1-diffraction orders are at a normalized intensity level of 0.390. Perturbations in the baseline grating performance, because of the presence of the SWG-ARSS and the evanescent coupling between the two diffractive elements, can induce undesirable efficiency changes to the baseline grating angular intensity spectrum, including possible reduction of odd order and increase of the even order intensities. This is evident in Figure 13(a), especially for the

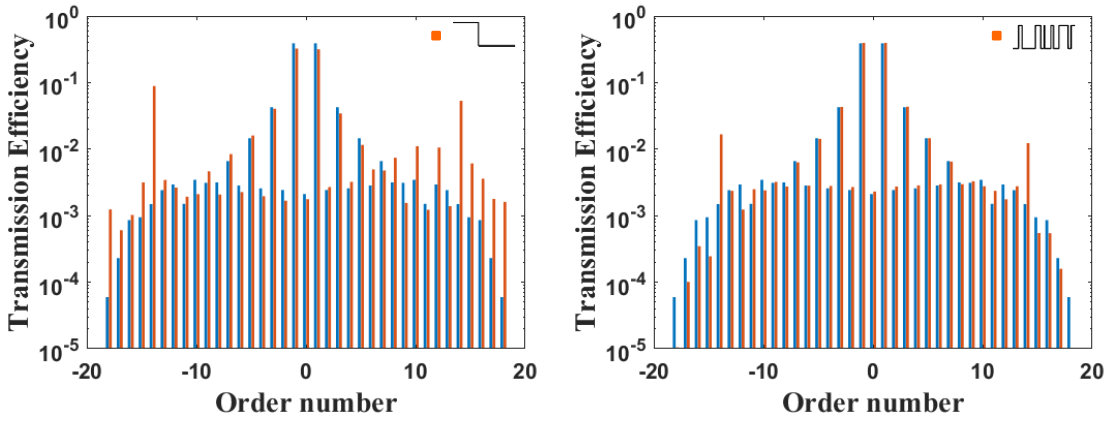

Figure 13 : RCWA-simulations of propagating diffraction-order efficiency for the silica baseline grating ($\Lambda_x = 8.00\mu m$, and $h = \lambda_\circ/2(n-1).$) with AR-structures multiplexed 14-times across the base period ($p_x = 571\text{nm}$), with TE polarization at normal incidence and $\lambda_0 = 633\text{nm}$. The efficiencies for the grating without the ARSS are shown as blue bars, compared to the efficiencies of the grating with ARSS in orange: (a) SWG in air, matched to 0th-order EMT conditions and, (b) a 21-order Dammann grating. In both cases the EMT fill-factor is: $f = 0.406$.

parasitic increase of the ±14th-diffraction orders to a level of 0.100 shown by the orange bars, due to the presence of the B-0 SWG on top of the baseline grating. The controlled ±1 diffraction orders are reduced to 0.325, although overall light transmission is enhanced by 2% over the Fresnel reflectance. In contrast, the effect of the D-21 SWG with re-distributed features on the same baseline grating (Figure 13(b)), produces an intensity spectrum closer to the original, with the ±1 diffraction order efficiency at 0.395 and an overall transmission enhancement of 3%. For both simulation results shown in the figure, the EMT fill-factor is exactly the same $f = 0.406$, suggesting that the layer-averaging EMT method should have the same outcome. In this study, any "parasitic" effects on the original baseline grating performance because of the AR transverse features distributions can be monitored through systematic selection of high-rank Dammann gratings. Further the observed effects on their AR functionality can be related to the calculated surface-feature correlations between the selected Dammann-SWG.

2.3 Numerical Experiment Design

2.3.1 Effective Medium Theory

Random ARSS surfaces are often modelled using the 0^{th}-order EMT for each distributed stratum. For SWG-ARSS profiles, with periods comparable to the incident wavelength and not strictly of sub-wavelength scale, 0^{th}-order EMT formulated using static approximations in relation to incident wavelength, and the periodic boundary profile becomes insufficient. For accurate computations, the use of higher-order EMT analysis becomes necessary. Higher-order EMT takes non-static interactions into consideration

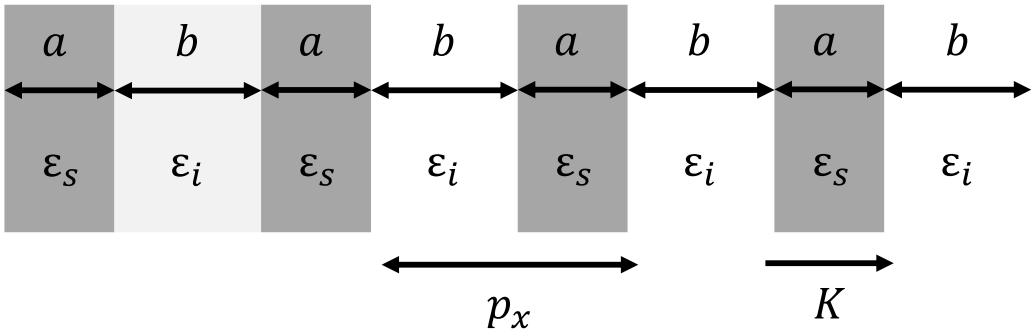

Figure 14 : Graphical depiction of a stratified medium consisting of two distinct materials. The substrate medium has a permittivity $\boldsymbol{\varepsilon_s}$ and the incident medium of permittivity $\boldsymbol{\varepsilon_i}$, the filling factor of the stratified medium is given as $f = a/p_x$ and K is the grating vector.

between the incident field and the effective optical index layers. For this study, the 2nd-order EMT was used to determine the modes of a binary-phase SWG as shown in the Figure 14. The 2nd-order EMT is derived using the Rytov approximation between the polarized electromagnetic waves perpendicular (⊥) and parallel (∥) to the stratified medium grating vector (K) [49]. Considering the periodicity of the AR structures, higher order EMT analysis uses methods similar to guided modes in a slab waveguide parallel to the substrate surface. Due to computational limitations, the numerical experiment was restricted to one-dimensional periodic profile for the baseline grating, with ordered and pseudo-random ARSS-SWG multiplexed on the surface of baseline grating. Because of the design choice, polarization of the incident field has to be taken into consideration, even at normal angle of incidence conditions. The equations of the stratified medium's effective permittivity to a 2nd-order coupling between the spatial period (p_x) and the incident wavelength $(\lambda_\circ)$ are given as:

$$\varepsilon_{E\perp K}^{(2)} = \varepsilon_{E\perp K}^{(0)}\left[1 + \frac{\pi^2}{3}\left(\frac{p_x}{\lambda_\circ}\right)^2 f^2(1-f)^2\left(\frac{(\varepsilon_s - \varepsilon_i)^2}{\varepsilon_0 \varepsilon_{E\perp K}^{(0)}}\right)\right] \quad (3)$$

$$\varepsilon_{E\|K}^{(2)} = \varepsilon_{E\|K}^{(0)}\left[1 + \frac{\pi^2}{3}\left(\frac{p_x}{\lambda_\circ}\right)^2 f^2(1-f)^2\left(\frac{\varepsilon_{E\perp K}^{(0)}}{\varepsilon_0}\right)\left(\frac{(\varepsilon_s - \varepsilon_i)\varepsilon_{E\|K}^{(0)}}{\varepsilon_i \varepsilon_s}\right)^2\right] \quad (4)$$

In equations (3) and (4) ε_0, ε_i and ε_s are respectively the permittivities of free space, superstrate and substrate, f is the filling-factor of the stratified layer, representing the volume fraction of substrate material contained within a spatial period p_x. The expressions of the 0th-order EMT permittivities included in the above equations are given as:

$$\varepsilon_{E\perp K}^{(0)} = (f\varepsilon_s + (1-f)\varepsilon_i) \quad (5)$$

$$\varepsilon_{E\|K}^{(0)} = \left(\frac{f}{\varepsilon_s} + \frac{1-f}{\varepsilon_i}\right) \quad (6)$$

Equations (3-6) represent the EMT permittivities of any SWG for incident light with TE or TM polarizations. The calculated permittivities are approximated to the average values of an equivalent SLAR coating, and do not depend on the relative position of distributed features within the period (p_x), but only on the filling fraction value f. For binary phase profiles designed as an AR-structure, as shown in Figure 10 (b), the effective index of the layer is computed as the square root of the resulting permittivity from the equations above. For an optimal SLAR using 0th-order EMT, the calculated fill fraction is: $f_{B0}^{(TE)} = (1 + n_s/n_i)^{-1}$ and $f_{B0}^{(TM)} = (1 + n_i/n_s)^{-1}$, for TE and TM polarizations respectively. The SWG depth was selected to be equal to that to the quarter-wave depth of the substrate's value, in accordance with SLAR thin-film equivalent conditions. These parametric selections define designs of two candidate EMT layers for the numerical experiment: the 0th-order EMT and, 2nd-order EMT binary-phase SWG, used as AR-structures on the baseline grating and are referred to as B-0 and B-2 in the following text.

To analyze the effects due to variations in transverse feature distributions using the designed numerical experiment for the fused silica substrate, the fill fractions comparable to an SLAR thin-film was estimated using the 0th and 2nd order EMT. Since the 2nd order EMT is a function of the period of the SWG (p_x), the variation of the fill fraction as a function of grating period was calculated for an incident wavelength of 633nm. A decrease in the fill fraction with the increase in the SWG period was observed, with fill-fraction reaching a maximum equal to 0th order EMT predicted value and remaining approximately constant for lower grating periods as shown in Figure 15. However, for the numerical study the smallest period of the SWG-ARSS was restricted to 400nm, due to computational limitations. The predicted fill-fractions from equations 3-6 are for TE polarization 0th order: $f_{B0}^{(TE)} = 0.406$, 2nd-order: $f_{B2}^{(TE)} = 0.334$; and for TM polarization 0th order: $f_{B0}^{(TM)} = 0.594$, and 2nd order: $f_{B2}^{(TM)} = 0.506$.

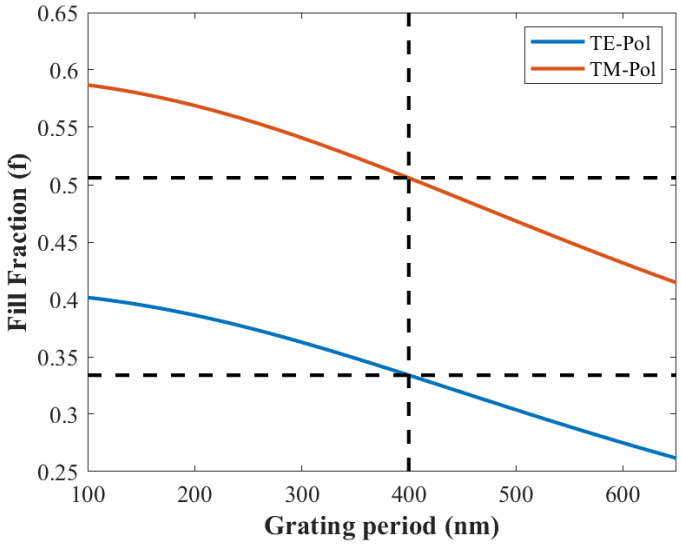

Figure 15 : Calculated fill fraction as a function of SWG period using 2nd order EMT for fused silica substrate at incident wavelength of 633nm for TE and TM polarization. where the dashed line indicates the fill fractions for grating period of 400nm.

2.3.2 Dammann Gratings as AR-layers

Profiles of non-binary ARSS are usually modelled as gradient-index homogeneous sequential layers, with gradual increase of the effective optical index from the ambient to substrate. Randomly structured AR surfaces have various feature profiles and spatial distributions, resulting from differences in fabrication methods, usually initiated and controlled through random masking such as sputtering or annealing, and have been documented to have various corresponding optical performances. To methodically control the numerical experiment, starting at the ordered SWG single-transmission state (binary phase profile), and transitioning to quasi-randomized feature distributions. The volume fill fraction f with the periodic unit cell is redistributed by segmenting and rearranging the segments, within the net sum of values for the respective TE and TM polarizations. A deterministic rearrangement of the of the phase transition locations within the periodic structure can be achieved using Dammann's selection rules [50,51].

Dammann gratings are deterministic binary phase profiles, designed to distribute an incident wave to an array of equal intensity diffraction orders in the far field, provided the optical binary phase depth of the profile is a half cycle (π) [52, 53]. These deterministically designed gratings are ranked with respect to their 2*N*+1 equal intensity orders, and are characterized by the *N* phase-transition points within their spatial period. The 1D-Damman phase profiles $g(x)$ can be described as:

$$g(x) = \sum_{m=0}^{N} (-1)^m \, \Pi\left(\frac{x - \frac{1}{2}(x_{m+1} + x_m)}{(x_{m+1} + x_m)} \right) \tag{7}$$

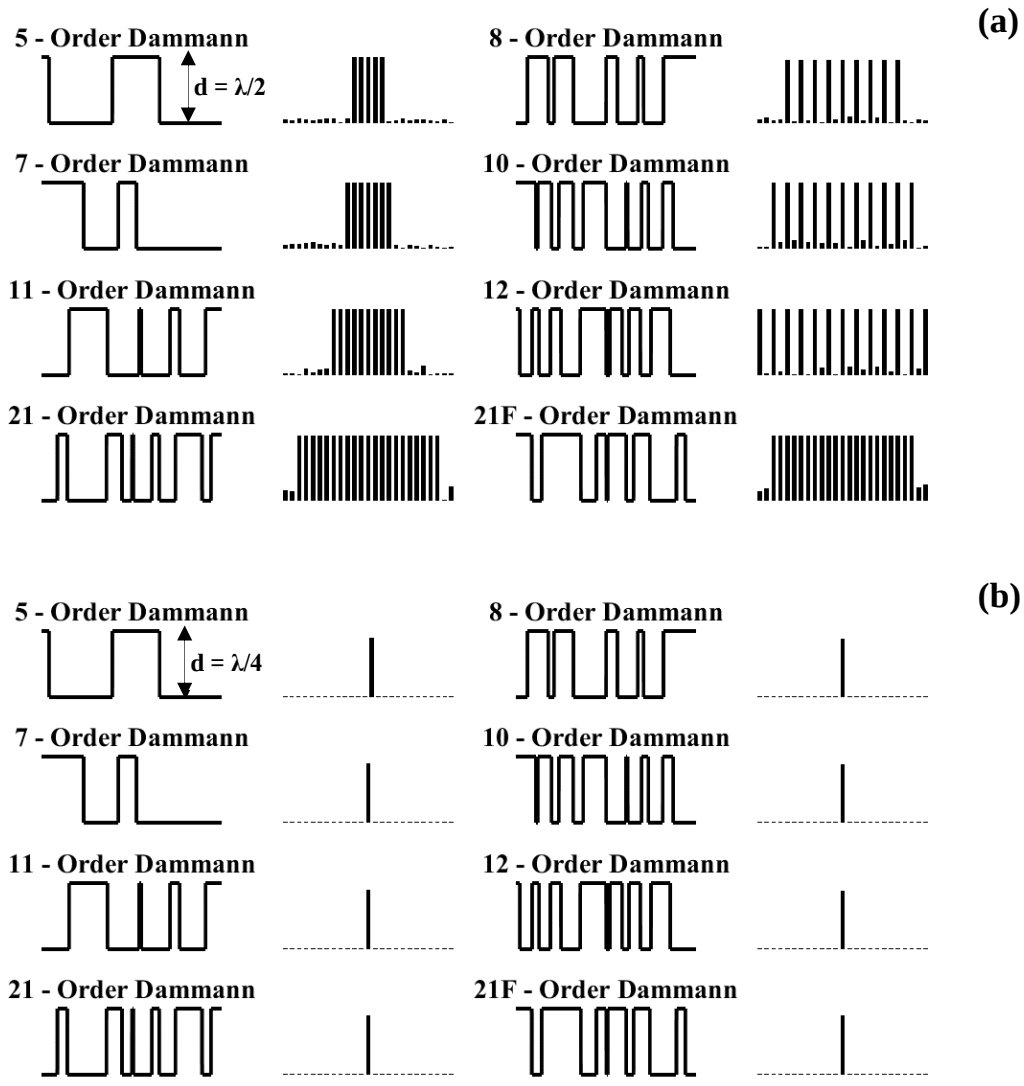

Figure 16 : Cross-Sectional view of 1-dimensional, normalized $\boldsymbol{N}$-order Dammann binary-phase grating profiles, within their periodic unit cell $\boldsymbol{p_x}$, along with their simulated angular intensity distribution for fused silica substrate at half wave depth (**a**) and quarter wave depth (**b**). (Left column): Odd-order Dammann gratings with volume fractions comparable to $\boldsymbol{f^{(TE)}}$ requirements. (Right column): Even-order Dammann gratings with volume fractions comparable $\boldsymbol{f^{(TM)}}$to requirements. The last entry is a reversed-tone grating to match the TM conditions.

Where x_m are the locations of the phase-transition points, and Π is the rectangular 1-dimensional window distribution of width b, centered at the coordinate a (*rect*-distribution

function). In essence, the sum of all the distributed rectangles yields the volume fraction f within a single period (p_x). Figure 16 shows a representative set of 1D-Dammann grating phase distributions. For gratings of increasing order-*N*, the number of transition points increases and the profiles become more complex. As seen in Figure 16 (a), feature size and width are not simple functions of locations or *N*, due to the far field diffraction intensity selection rules imposed by the scalar Fourier Transform approximation. There are some notable properties of the distributions though. Even-rank Dammann gratings result in 0^{th} diffracted order suppression and considerable reduction of all even diffraction orders intensities. This is a consequence of symmetry, as the 0^{th} order located on-axis will always be unpaired, and therefore the total equalized energy from the diffraction spots will be restricted to odd number diffraction orders. Because of this consequence, the volume fill fraction of the even-rank Dammann gratings is always $f_{EVEN} = 0.500$. There is no such restriction for the odd-rank Dammann, and their fill fractions can in principle span over all possible values of f, however, due to their equal intensity requirement, optimized solutions are restricted to values $0.300 \leq f_{ODD} \leq 0.405$. If the substrate and superstrate reflective index are exchanged (tone reversal) the optimized solutions for the fill-factor are bound by: $0.580 \leq f_{ODD} \leq 0.700$ as shown in figure 17. Considering the EMT fill fraction f values of B-0 and B-2 for TE and TM polarizations, it was observed that even-rank Dammann gratings match very well with f_{B2} for TM polarization and the odd ones can cover a range between the values f_{B0} and f_{B2} for TE polarization. The reversed-tone of odd-order Dammann match closely the range between f_{B0} and f_{B2} for TM polarization.

The depth of the AR-SWG profiles was restricted to a quarter of the incident wavelength ($\lambda/4$) to match perfect SLAR thin film layer thickness. However, since the

profiles of choice are no longer at their functional depth for the equal-efficiency conditions of Dammann gratings, the intensity of the 0^{th} order is increased and all higher propagating orders are suppressed as shown in the Figure 16 (b). The intensity equalized diffraction order (IEDO) and the other propagating orders become evanescent as the period p_x is reduced from near-wavelength to sub-wavelength.

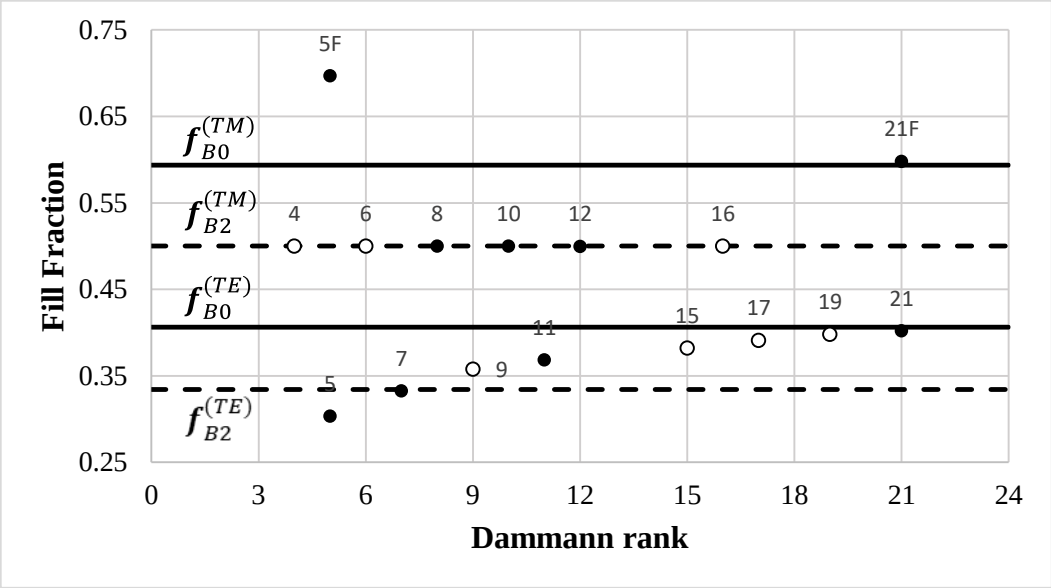

Figure 17 : Fill Fraction variation with respect to Dammann grating rank, shown here as the number adjacent to the markers. The solid and dashed lines represent the calculated EMT 0^{th} and EMT 2^{nd} order fill-fraction. Dammann gratings used in the computations are represented with the black-circular markers and the rest as open-circular markers.

To characterize the transverse feature spatial distributions (complexity) of all phase profiles considered, the normalized spatial autocorrelation of Dammann unit cells was computed, which is a measure of self-similarity for the pseudo-random profiles. For consistency the distance from the center to the first local minimum of the calculated autocorrelation was chosen as the measure for the correlation length, because of the different fill fractions of the Dammann gratings as shown in Figure 18. The calculated autocorrelation lengths, normalized to the period of Dammann grating profiles selected in

the study, have a decreasing trend with increasing Dammann grating rank, for both odd and even IEDO as shown in Figure 19. The increase in the number of phase-transition locations *N* within the Dammann grating unit cells results in increasingly complex profiles for higher ranks compared to lower Dammann ranks.

To analyze the variation in performance of the Dammann gratings as an efficient ARSS-SWG, designs with varying transverse features, with fill fractions spanning the predicted 0^{th} order and 2^{nd} order EMT for each polarization and complexity were chosen, as shown by the solid markers in the Figure 17 and Figure 19. The selected Dammann grating phase profiles along with SWG (B-0 and B-2), were multiplexed on the two-level phase mesas

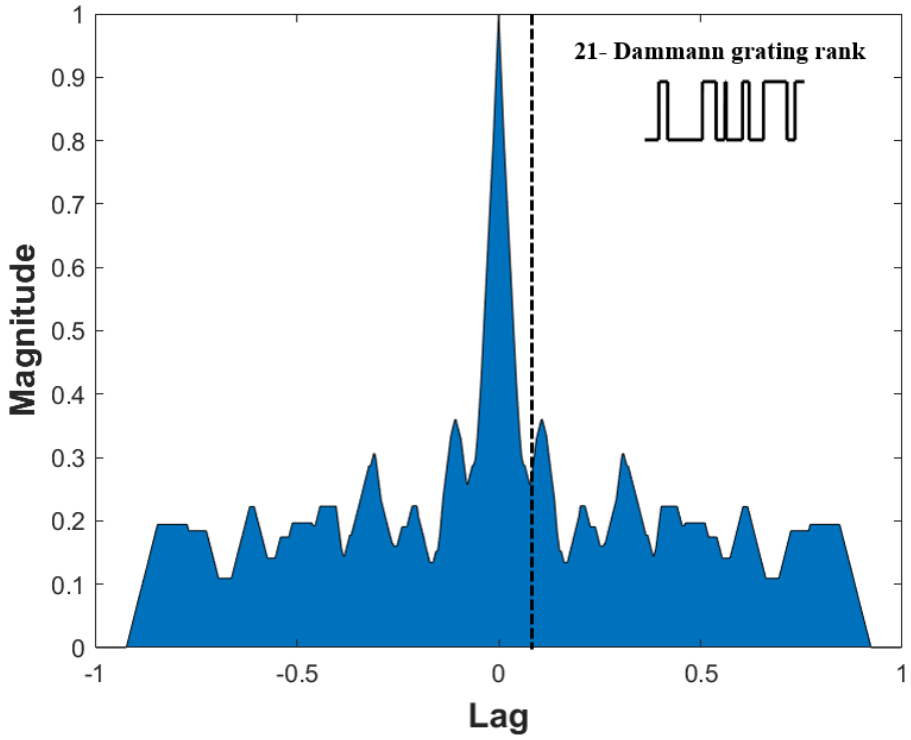

Figure 18 : Normalized autocorrelation of 21-Dammann grating rank unit cell., The dashed line indicates the first minimum along the transverse dimensional axis, used as a reference to measure the profile correlation length. The computation used is serial multiplication, not an equivalent linear transform method.

of the 50% duty cycle, binary, π-phase depth baseline grating. The ratio of the baseline grating period to the ARSS grating periodicity is a measure of the structured AR spatial periodic frequency and is defined as: $k = \Lambda_x/p_x$. For even multiplexed frequencies $k = 2,4,6,\ldots 20$ is the ARRS periods scale from to super-wavelength to subwavelength. The period of the baseline grating is kept constant throughout the computations, as shown in Figure 10, to retain the ability to observe the response of the desired and undesired diffracted orders. The multiplex ratios were restricted to even, to have equalized the total number of p_x on each of the phase levels of the baseline grating.

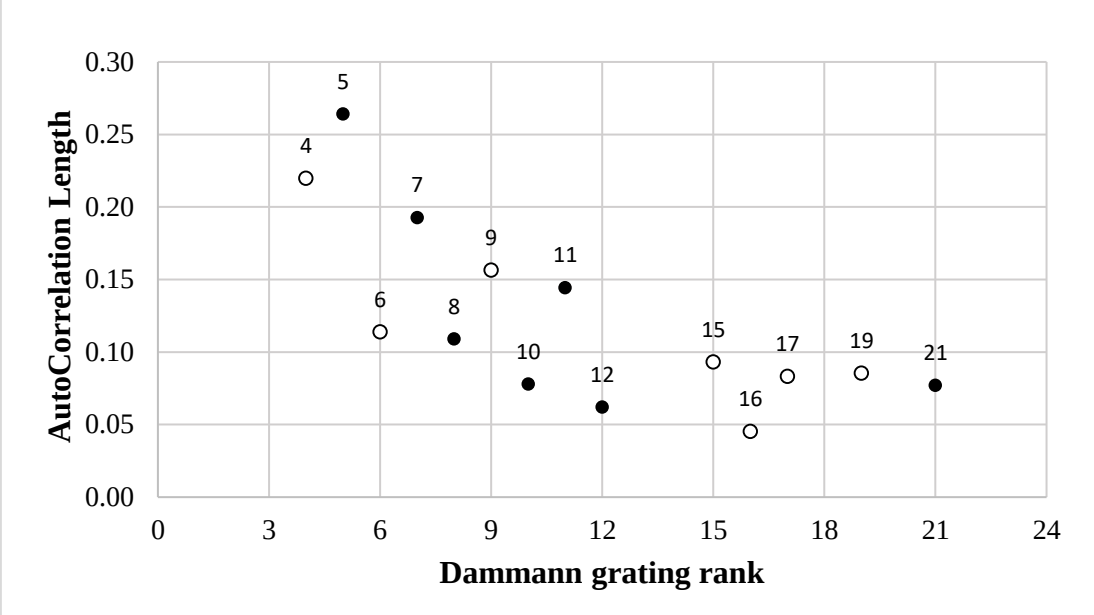

Figure 19 : Normalized autocorrelation length with respect to Dammann grating rank. The measured Dammann gratings are represented with the black circular markers and the rest as black annular markers.

2.4 Numerical Experiment Results

2.4.1 Net Transmission Enhancement

Net transmission enhancement of the baseline grating performance as a function of multiplex ratio *k* was computed using RCWA, for both TE and TM polarizations, shown in Figure 20. The baseline grating is capped by the SWG-binary 0th and 2nd EMT and the corresponding choices of SW-AR-Dammann grating profiles, with volume fractions restricted to the same EMT-layer conditions. The transmission enhancement was calculated, as the fraction of the on-axis transmittance for each diffraction order for the baseline grating with and without the choices of SWG-ARSS, by:

$$\tau_{B,D}^{(TE,TM)}(k) = \left[\frac{\sum_{m=-q}^{+q} \hat{T}_m^{(TE,TM)}(k)}{\sum_{m=-q}^{+q} T_m^{(TE,TM)}(\Lambda_x)} - 1\right]_{\lambda_\circ,\Lambda_x,d} \tag{8}$$

Where B,D stands for the SWG binary identifier (B-X) or the Dammann unit cell identifier (D-XX), m is the spatial diffraction order integer-index spanning the baseline grating's propagating diffraction order spectrum: $-q \leq m \leq +q$; and $T_m^{(TE,TM)}(\Lambda_x)$, $\hat{T}_m^{(TE,TM)}(k)$ are respectively the diffractive order-transmitted powers of the baseline grating without, and with, the ARSS gratings. As mentioned in the section 2.2, diffraction orders up to $\pm 5q$ were retained in the RCWA simulations, to maintain the energy conservation and evanescent order cross-coupling between the baseline grating and the ARSS-SWG choices. The baseline-grating period (Λ_x), the AR-layer thickness (d) and the incident wavelength ($\lambda_\circ$) were kept constant throughout the simulations. The calculated net transmission from the simulations of the baseline grating, which is an independent summation of all

propagating orders, was verified to be equal to the Fresnel-derived intensity for the fused silica substrate:

$$T(\lambda_\circ) = \sum_{m=-q}^{+q} \left[T_m^{(TE)}(\Lambda_x)\right]_{\lambda_\circ,\Lambda_x,d} = \sum_{m=-q}^{+q} \left[T_m^{(TM)}(\Lambda_x)\right]_{\lambda_\circ,\Lambda_x,d}$$
$$= 1 - \left|\frac{n_i(\lambda_\circ) - n_s(\lambda_\circ)}{n_i(\lambda_\circ) + n_s(\lambda_\circ)}\right|^2$$
$$= 1 - \left(f_{B0}^{(TE)} - f_{B0}^{(TM)}\right)^2 \quad (9)$$

In the numerical experiment, at normal incidence values the left side of equation 9 (net transmission for TE or TM incident polarizations) is independent of polarization state because of the summation of all diffracted order contributions from the baseline grating. The right side (Fresnel-derived transmission) is also polarization independent for normal angle of incidence. The result can be expressed in terms of the SWG effective index of 0^{th}-order EMT fill fractions for the perfect SLAR layer.

Fused silica windows have an average normalized transmission of 0.931 across the visible spectrum, with each surface contributing to Fresnel reflectance by 0.035. Since the numerical simulations were restricted to a single surface, the strictly subwavelength regime multiplexed ARSS gratings ($k = 20$) were observed to approach a net enhancement of 3.5% with little to no difference between the incident polarization states. For multiplex ratios $18 \geq k \geq 10$, in the wavelength-scale regime, the presence of higher ARSS grating-induced propagating orders and cross-coupling between the multiplexed gratings, resulted in transmission enhancement decrease. This is evident for B-0 and B-2 ARSS,

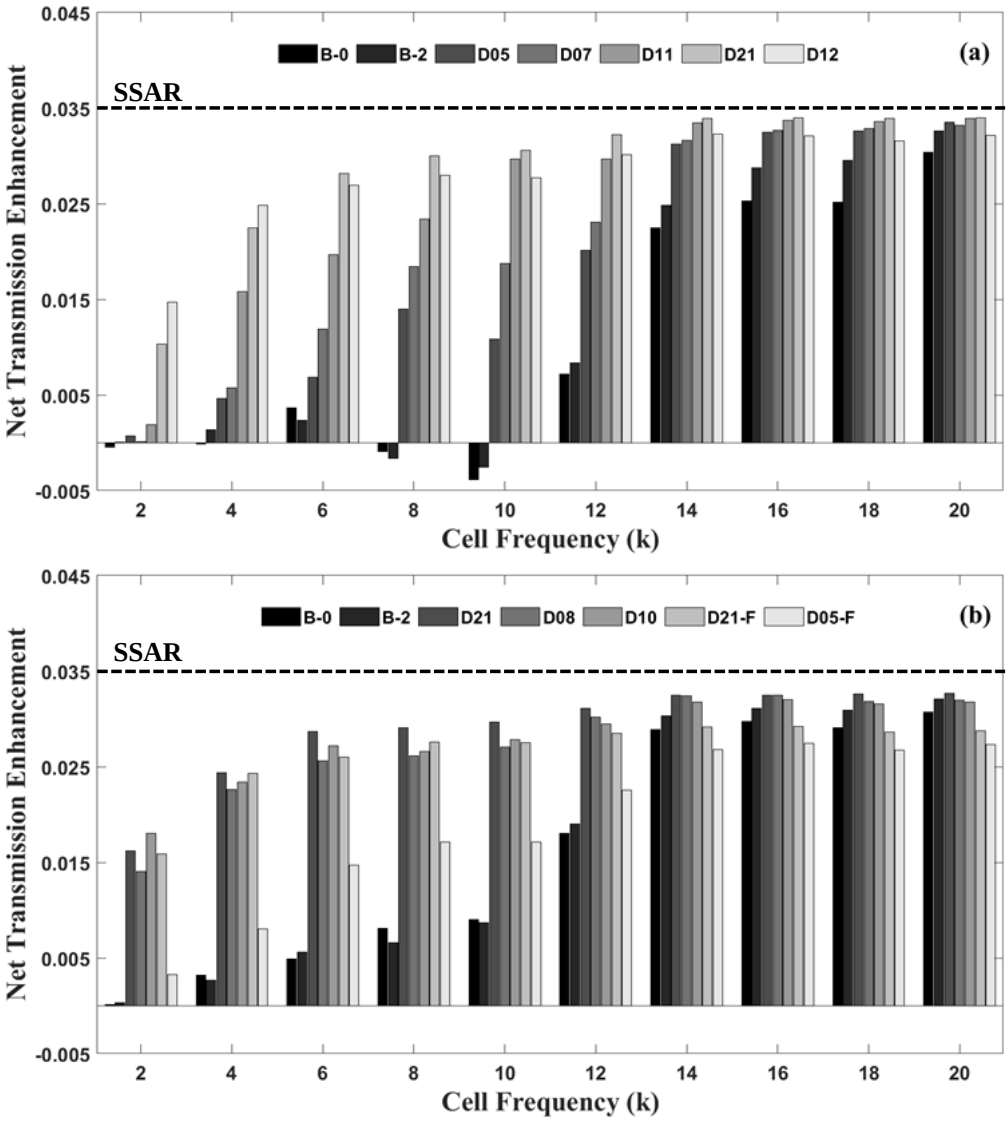

Figure 20 : Net transmission enhancement of fused silica 1-D binary phase, 50% duty cycle grating, with 1-D Dammann gratings acting as ARS surfaces, as a function of the Dammann multiplex frequency k. (a) TE-polarization and (b) TM-polarization for various volume fractions of Dammann gratings, in comparison to binary gratings with EMT-0^{th} and EMT-2^{nd} order approximation. The IEDO are labelled as DXX, based on their equal-order population. The post-script F indicates that the phase was reversed in order to satisfy the corresponding EMT fill-factor upper limit for TM. Negative values indicate transmission losses due to reflection and the maximum enhancement because of single surface AR (SSAR) is indicated by a dashed line.

along with ARSS-Dammann gratings with high value autocorrelation lengths (such as D-05 and D-07), while gratings with smaller value autocorrelation lengths show a consistent enhancement of about 3% for both polarizations. In the super-wavelength regime, for multiplex ratios $8 \geq k \geq 2$, while the gratings B-0 and B-2 show little to no enhancement, gratings D-05 and D-07 show average enhancements of about 1%. Gratings D-11, D-21 and D-12 (for TE) along with gratings D-21, D-21F, D-08 and D-10 (for TM) show better performance with average enhancements of about 2%.

The numerical computation results suggest an enhancement in overall transmission due to the presence of the ARSS-gratings. However, one should be mindful of the baseline grating's performance, which was designed to propagate odd diffraction orders and suppress the even orders, shown previously in Figure 12. Superposition of the AR-gratings perturb the function of the baseline grating, affecting the transmission intensities of both the propagating odd and even orders, strongly dependent on ARSS-grating multiplex ratio choices. To investigate the variations in the performance of the AR-gratings, net enhancement (Equation 10) of the odd-DO transmission is shown in Figure 21, as a function of multiplex ratio for the AR-gratings choices. The directed odd-diffraction orders were considered as contributing to the design desired transmission $t_{B,D}^{(TE,TM)}(k)$, whereas the even-diffraction orders can be considered as a form of undesirable scatter $\sigma_{B,D}^{(TE,TM)}(k)$:

$$\tau_{B,D}^{(TE,TM)}(k) = \left(\left[\frac{\sum_{m=-q'}^{+q'} \hat{T}_m^{(TE,TM)}(k)}{\sum_{m=-q'}^{+q'} \hat{T}_m^{(TE,TM)}(\Lambda_x)} - 1 \right] + \left[\frac{\sum_{m=-q''}^{+q''} \hat{T}_m^{(TE,TM)}(k)}{\sum_{m=-q''}^{+q''} \hat{T}_m^{(TE,TM)}(\Lambda_x)} - 1 \right] \right)_{\lambda_\circ, \Lambda_x, d}$$

$$= t_{B,D}^{(TE,TM)}(k) + \sigma_{B,D}^{(TE,TM)}(k) \qquad (10)$$

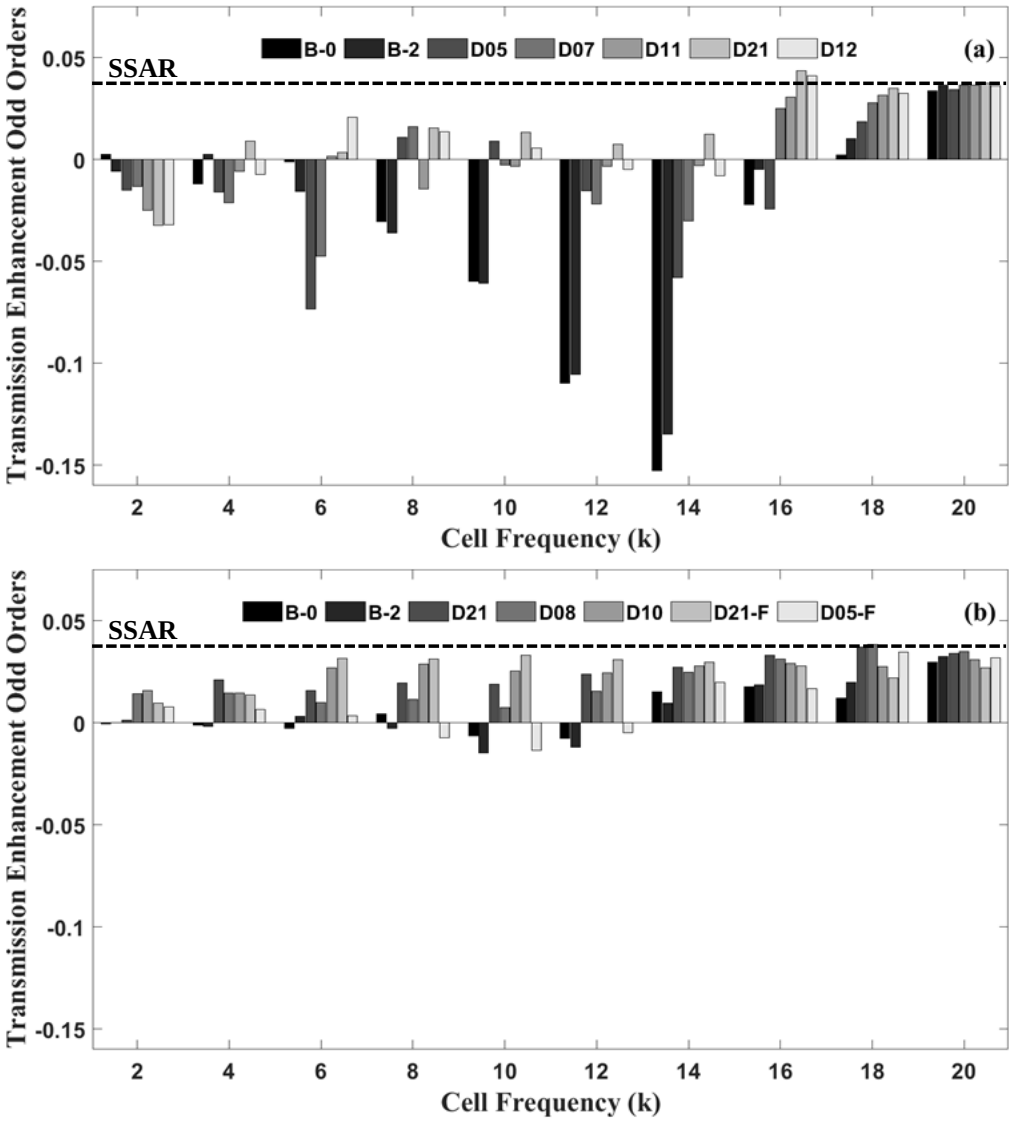

Figure 21 : Odd DO transmission enhancement (directed power) of fused silica 1-D binary phase, 50% duty cycle grating, with 1-D Dammann gratings acting as ARS surfaces, as a function of the Dammann multiplex ratio frequency k. (a) TE-polarization and (b) TM-polarization for various volume fractions of Dammann gratings, in comparison to binary gratings with EMT-0th and EMT-2nd order approximation. The IEDO are labelled as DXX, based on their equal-order population. The post-script F indicates that the phase was reversed in order to satisfy the corresponding EMT fill-factor upper limit for TM. Negative values indicate transmission losses due to reflection or scatter and the maximum enhancement because of single surface AR (SSAR) is indicated by a dashed line.

In equation 10, the summation over q'includes only odd integers, while the q''integers are only even. The scattering term includes the 0th-diffraction order, which incorporates any phase-step perturbation effects due to the presence of the ARSS-layer thickness. In the subwavelength regime $(k = 20)$, for both incident polarizations the transmission enhancement of the odd orders matches in value the net transmission enhancement, while a significant reduction in enhancement is observed in the wavelength-scale regime $(18 \geq k \geq 10)$. For TE polarization, directed transmission scattering losses were observed for all AR-gratings with $(14 \geq k \geq 10)$, except for D-21 which had an average enhancement of about 1%, in contrast to the net transmission enhancement observed in Figure 20(a) for every ARSS-grating type. For TM polarization, the observed net enhancement of odd diffraction orders for every AR-grating follows closely to the trends observed in Figure 20(b), except in the cases for B-0 and B-2. In the super-wavelength-scale regime $(8 \geq k \geq 2)$, there was negligible enhancement for TE polarization in correlation to the near-wavelength regime, whereas, an average enhancement of about 1% to 1.5% for all the AR-gratings other than B-0 and B-2 for TM polarization was achieved.

2.4.2 Transmission Angular Intensity Spectrum

Intensity transmission enhancement for each propagating diffraction order $\tau_{B,D}^{(TE,TM)}(k)$, as a function of the multiplexed AR-gratings B-0, B-2, and the selected Dammann AR-gratings is plotted in Figure 22 and Figure 23. For TE polarization in the subwavelength regime $(k = 20)$ a uniform enhancement of the angular intensity spectrum is observed for D-11, D-21 and D-12 with slight perturbations in the higher diffraction

orders, while for B-0, B-2, D-05 and D-07 the perturbations were observed to be more prominent. This suggests high-angle scatter, even at SWG scales. In the wavelength-scale and super-wavelength regime ($14 \geq k \geq 2$), even though a uniform transmission enhancement of the low-diffraction order is observed for odd and even orders, perturbations of higher orders has increased considerably from the nominal baseline

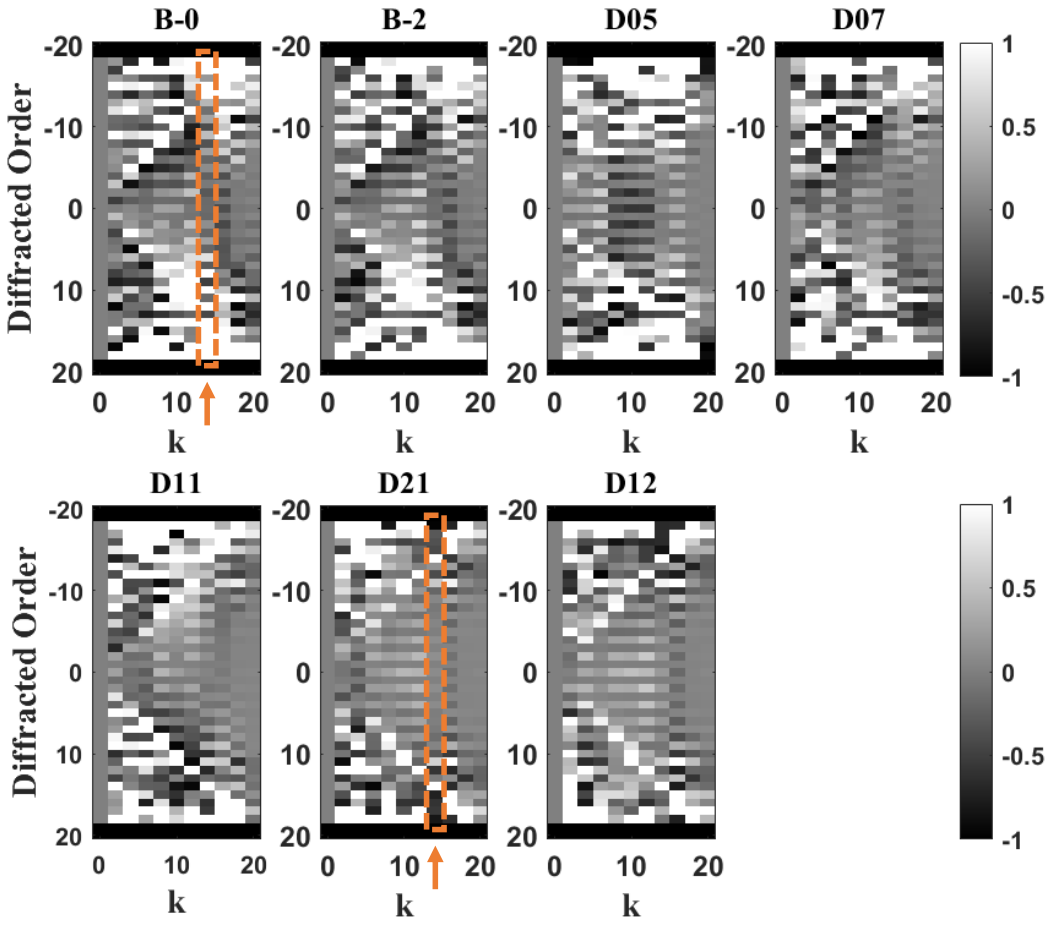

Figure 22 : Transmission enhancement (τ) of all Diffraction orders for incident polarization of TE of a fused silica 1-D binary 50% duty cycle grating, as a function of multiplex ratio k with 1-D ARS surface gratings for the selected gratings. The baseline grating without ARSS is represented by k = 0 and τ = 0. The arrow marked in orange on the TE B-0 and D-21 indicate τ for the data shown in Figure 13.

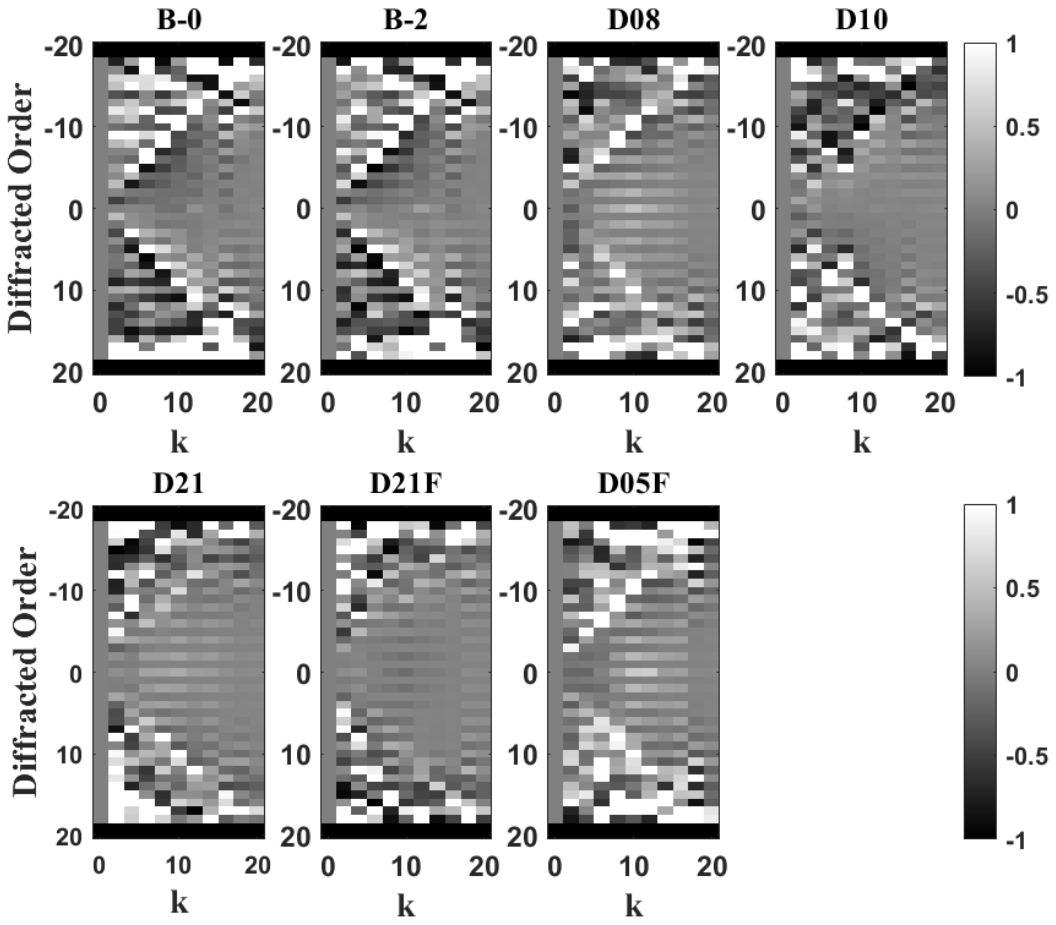

Figure 23 : Transmission enhancement (τ) of all Diffraction orders for incident polarization of TM of a fused silica 1-D binary 50% duty cycle grating, as a function of multiplex ratio k with 1-D ARS surface gratings for the selected gratings. The baseline grating without ARSS is represented by k = 0 and τ = 0.

performance values. This is a direct consequence of the higher-diffraction orders generated by the presence of the AR-gratings. The propagating higher diffraction orders for smaller *k* choices cross couple into the baseline grating angular spectrum, causing the odd and even diffraction order competing performance from Figure 20 and Figure. 21. TM polarization has similar trends with decreasing multiplexed ratios; while in contrast, the diffraction order perturbations in intensity are weaker compared to TE for all the AR-gratings simulated. Variations in the baseline grating diffraction order intensity efficiencies signify

some ARSS-grating transverse-feature distribution dependence beyond the EMT volume fraction values. It is also noted that transverse-feature distribution dependence of the multiplexed AR-gratings with lower autocorrelation lengths, such as D-21, D-12, D-10, result in weaker scatter contributions compared to their larger autocorrelation length counterparts, such as D-5, D-7 or D-8. Other than the numerical results presented here, there are no qualitative indications as to why these trends are as such.

2.4.3 Wave propagation simulations

In order to quantify the feature distribution effects on the directed transmission enhancement $t_{B,D}^{(TE,TM)}(k)$, we simulated the intensity distribution for each polarization state near the baseline-grating's surface. The results for two cases, B-2 and D-21, are presented in Figure 24. Both AR-gratings have a subwavelength periodicity with multiplex spatial frequency $k = 20$. A transverse section of a single period of the baseline grating is shown ($\Lambda_x = 8\mu m$). We note that both AR-gratings have a directional transmission enhancement $t_{B,D}^{(TE,TM)}(k) \geq 0.03$, as seen in Figure 20 and 21. Figures 24(a)-TE and 24(c)-TM show the formation of high-intensity nodes within the B-2 AR-grating layer. The reflected intensity has low contrast fringes, whereas the transmitted intensity has high-contrast regions within the substrate medium, indicating the flow of diffracted energy into the substrate because of the baseline grating performance. The intensity within the D-21 AR-grating layer, in Figure 24(b)-TE, shows considerable reduction in intensity localization within the ARS layer, with lower fringe contrast in reflection. The TM polarization for D-21 (Figure 24(d)) shows localization of intensity within the AR-grating's

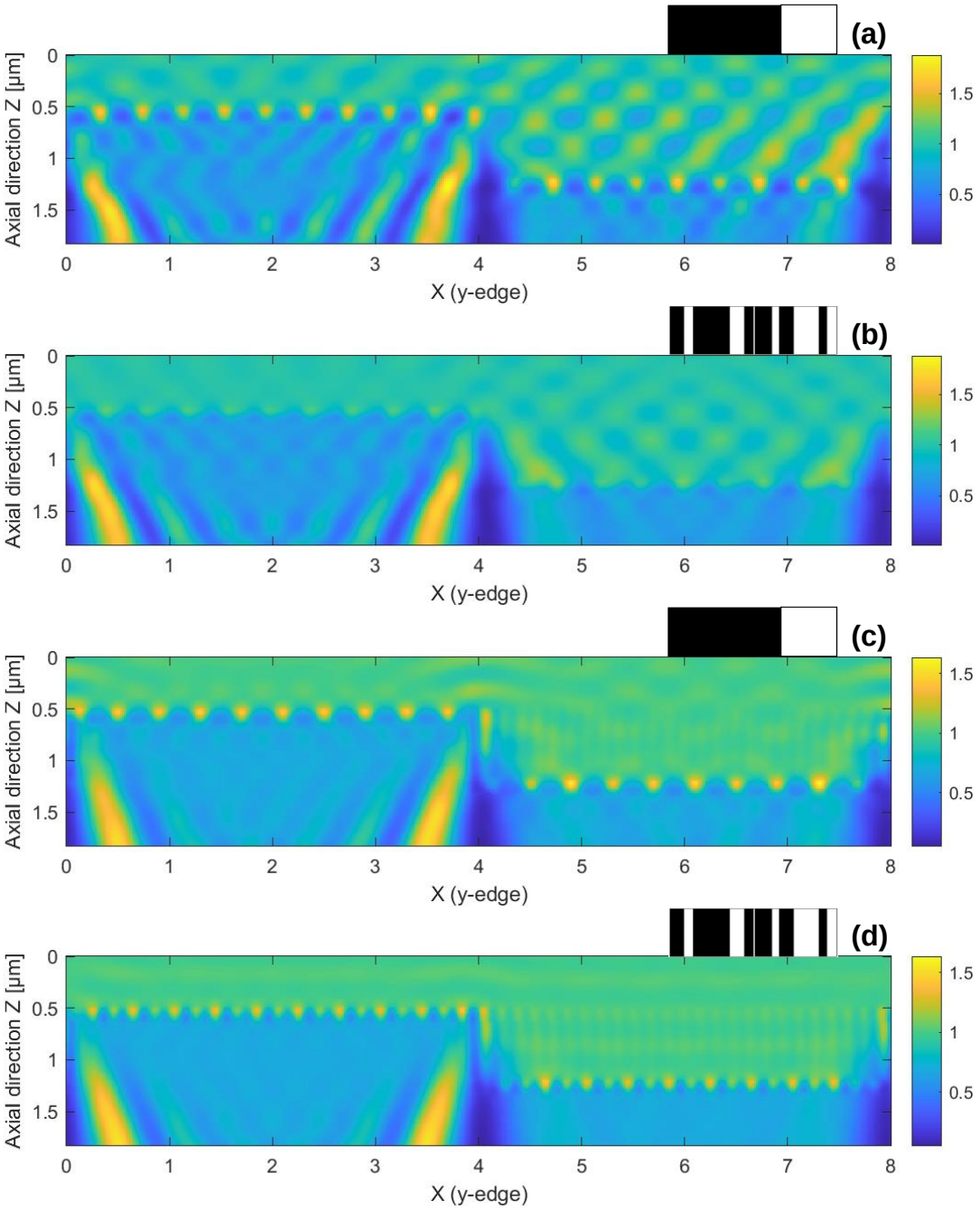

Figure 24 : Simulated intensity distribution in the plane of incidence, near the baseline-grating surface for: (a) TE from B-2; (b) TE from D-21; (c) TM from B-2 and (d) TM from D-21. In all cases k = 20. For comparison, the top-down phase profile of the AR-gratings is shown next to the enumeration. The baseline-grating profile begins at z = 0.5 µm, and extends into the substrate for higher values of z. The color bar is in normalized arbitrary units.

layer, with a doubled spatial frequency distribution compared to Figure 24(c). These results indicate that AR-grating profile feature distributions on the surface of the baseline grating have noticeable effects in the performance of the combined device. More importantly, we note that if 2nd-order EMT is used for the initial AR-grating design, B-2 is a conventionally better criterion match, although D-21 (which matches the 0th-order EMT criterion) is actually performing at or higher AR-efficiency and with less transmission scatter.

2.5 Summary

In this chapter, results from a numerical experiment designed to explore the effects of nanostructured surfaces acting as anti-reflective layers added on the surface of a one-dimensional, 50% duty-cycle, baseline binary-phase grating, were presented. The goal of the numerical study was to determine the degree of agreement between ordered periodic ARSS profiles designed based on EMT refractive index fill-fraction criteria and, pseudo-randomly distributed binary-phase encoded profiles (Dammann gratings) acting as transmission enhancers. In order to differentiate between the simple binary AR-gratings and the AR-Dammann grating profiles, the fill-fraction of the equivalent EMT layer was used, and the ARSS-grating profile autocorrelation length categorized the AR-structures. The depth of the AR-layer was restricted to one-fourth of the light wavelength at normal incidence, to investigate solution possibilities for thin-layered ARSS, which would preserve the form and function of the baseline diffractive element. Transmission efficiency of all propagating orders from the baseline grating, segregating the angular spectrum into directed and scattered diffraction orders were simulated for both the polarizations.

The results presented show that for simple profile AR-gratings, with transverse profile large autocorrelation lengths or just a single phase-transition within their periodic cell, overall Fresnel reflectivity can be suppressed from the structured surface. Perturbative effects on the directed transmission efficiency, due to cross-coupling between the ARSS-gratings and the baseline grating, increase relative scatter. In contrast, complex grating profiles with short autocorrelation lengths tend to preserve the directed power transmission distribution, have significantly lower scatter and, are equally effective in reflectivity reduction. These effects are strongly dependent on the ratio of the ARSS-grating unit cell period to the incident wavelength value, improving anti-reflectivity as the cells become subwavelength in scale. Off-direction scatter is not reduced just by decreasing the size of the ARSS periodic cell, unless periods of the unit cells are strictly sub-wavelength.

The two foundational models used for light interacting with an optical surface are: the effective-medium approximation (EMT) and, subwavelength periodic sinusoidal grating multiplexing (SWGM). The former can match AR-conditions using homogeneous-layer optical index stratification of boundaries, whereas the later accounts for scattering by superposing a large collection of “thin” gratings as the surface profile. These models are complementary in concept, as EMT cannot predict scatter and SWGM cannot suppress Fresnel reflectivity. The presented results from the numerical study show that even at near-wavelength periodic scales and thin single-layer restrictions, a redistribution of the ARSS features can result in high values of light total transmission and directionality. The effects are sensitive to feature distribution and organization, not just to the feature number or density. Based on the tested pseudo-random Dammann grating profiles, we observe that increasing Dammann-order ranks have more stability and consistency in results, as the

periodic cell length is reduced from wavelength-scales to sub-wavelength. This realization suggests that deterministic pseudo-random scatterers can “cooperate”, reducing the optical boundary electromagnetic impedance discontinuity.

The cooperative scattering of the higher-order Dammann ranks is supported by rigorous coupled-wave analysis simulations of the wavefront intensity near the surface, as shown in Figure 24. Simple AR-SWG structures added on a diffractive optical surface were observed to induce high-intensity localization within the ARS layer for both incident polarization states. This is due to the confined superposition of incident and reflected wavefronts, which continue to propagate in the transmission and reflection directions, eventually forming the forward-diffracted orders and, incident-reflected destructive interference conditions respectively. The redistribution of the AR-grating features was observed to have distinct effects for each incident polarization state. In the case of incident TE polarization (Figure 24(b)) the effect is equivalent to an optical impedance match, resulting in transparency of the diffractive boundary, without disturbing the baseline grating performance. For TM polarization (Figure 24(d)), since the polarization vector is in the plane of the AR-grating grooves, a bi-periodic intensity distribution is observed, indicating that there are two counteracting field distributions, responsible for the generation of destructive interference in the reflected direction and constructive superposition in the transmitted direction. For both polarization cases, Fresnel reflectivity was suppressed and directional transmission is unaltered in intensity distribution, with an enhancment in total value. We note that there is no strict subwavelength scale criterion satisfied for cases of high-order Dammann ARSS, as they are very effective for k values as low as 14, which for our experiment is equivalent to a 571 nm periodic cell, and therefore in the wavelength-scale range. The long correlation

length ARSS fail to compete successfully, as for similar periodic scales they scatter strongly and have lower overall transmission enhancement. An underlying feature complexity indicator could possibly quantify the optical impedance matching process with some predictability. Such scale transition studies could bridge understanding of random ARSS, which have multi-periodic features and short surface autocorrelation lengths.

CHAPTER 3: INVETSIGATION OF THE OPTICAL PERFORMANCE OF ANTI-REFLECTION RANDOM NANO STRUCTURES ON DIFFRACTIVE ELEMENTS

3.1 Introduction

Chapter 2 presented the numerical investigation of the AR and scatter functionalities of the transitional-redistribution of phase nanostructures from anti-reflective periodic (ordered) SWG to a pseudo-randomized feature distribution on the surface. The goal was to examine the transverse surface feature distribution characteristics and their effects on the suppression of Fresnel reflectivity. The literature to date has numerous studies on fabrication and testing of the periodic, or random anti-reflective structures (rARSS) on optical flats, because of their straight forward and simpler optical characterization, while few studies are available on non-planar surfaces, such as lenses and binary diffractive gratings. Diffractive optical elements (DOE) such as spot arrays, beam shapers, controlled angle diffusers and diffractive Fresnel lens are optics with surface encoded information, usually generated by iterative optimization Fourier transform algorithms, that redistribute incident light irradiance to generate a desired pattern in the near or far field. DOE have Fresnel loses, and coating them with conformal or non-conformal thin film coatings is challenging due to their complicated surface topography. For a DOE to function as intended, the coating must be included in the original design specifications, further increasing design and implementation complexity. As mentioned in Chapter 1, recent studies on random anti-reflective structures (rARSS), show that an RF-driven reactive ion plasma can be used to fabricate rARSS on flat optical surfaces by etching them. The same technique can be applied to prefabricated phase optics such as lenses, micro lens arrays,

and near-wavelength scale gratings, with little to no perturbations in their respective performance [28-33]. Fabrication of rARSS to suppress the Fresnel reflections on DOE would expand the applications of random nanostructures as an AR treatment.

Because this chapter focuses on the characterization of the optical performance of the rARSS on the multiple phase level deterministic phase diffusion DOE, it is important to thoroughly discuss any similar studies in the literature. While no studies where found on the application of periodic or random AR structures on multiphase level DOE, few studies on their applications as an AR treatment for phase optics such as lenses and binary gratings are available. In most studies for lenses, the data presented was SEM or atomic force microscope (AFM) images of subwavelength structures and their transmission and reflection spectra, comparing respective blanks processed with and without AR structured surfaces [54-56]. Few papers have given a detailed study on the optical performance and the effects of AR structured surfaces on lenses using Strehl ratio and aberrations calculations, focal spot profiles and imaging properties, demonstrating increased brightness because of reflection suppression [57-59]. For microscale binary gratings, few groups were successfully able to fabricate tapered conical shaped subwavelength structures on silicon substrates, reporting a significant suppression in reflections [42, 60].

This chapter primarily focuses on characterizing the optical performance of the multi-phase level pseudo-random fused silica DOE such as spot array generators, controlled angle diffusers, and diffractive Fresnel lens, with rARSS originally optimized for flat optical surfaces. To fully investigate the effects of rARSS on the complex phase profiles, four commercially available DOE with varying topographies and field of views were chosen.

Section 3.2 will present the results of fabrication of rARSS on both sides of fused silica DOE. The scanning electron micrographs along with confocal microscope images are presented to observe differences in the surface topography of DOE, before and after fabrication of rARSS. The top down images show the formation of the rARSS without perturbing the complex topographies of the DOE.

Section 3.3 presents the characterization of the rARSS optical performance on DOE such as spot array generators and a controlled angle light diffuser. Since DOE act as deterministic scatterers, presence of nanoscale transverse AR structures can result in non-deterministic scatter in the light projection direction. A detailed comparison of on-axis and off-axis angle resolved scatter signatures of the DOE, before and after addition of rARSS, in transmission and reflection are presented. The 633nm incident wavelength was along the normal to the DOE surface, and the light polarization state was perpendicular to the plane of detection (*S*-polarization.)

Section 3.4 presents the characterization of the rARSS optical performance on a diffractive Fresnel lens, consisting of a segmented multilevel phase 3D-profile Fresnel zones. Since Fresnel lenses have increasing spatial frequencies from center to edge by design, they are sensitive to any surface perturbations that can affect their performance, such as changes in focal length and focal spot beam profiles, that may result from the subtractive fabrication process (etching) of rARSS. Moreover, as the Fresnel phase boundaries (zones) are designed for specific wavelength criteria, any surface phase-profile impact would be measurable in transmission and refection, especially if the components are tested at five different wavelengths (543nm, 594nm, 604nm, 612nm, 633nm), as presented herewith.

Section 3.5 presents the surface characterization of the rARSS fabricated on complex topographies of DOE from their respective scanning electron micrographs, in comparison to optical windows, using a granulometry technique.

Section 3.6 presents the optical scatter measurements of the rARSS on optical windows and near wavelength binary gratings and their effects on their optical performance.

Finally, Section 3.7 will summarize the results from the previous sections and draw final conclusions about the optical performance of DOE processed with rARSS.

3.2 Fabrication of rARSS on Fused Silica Diffractive Optical Elements

Four commercially available, fused silica substrate, uncoated, multiphase level DOE, were chosen to study the rARSS addition effects: three diffractive diffusers and a diffractive Fresnel lens of dimensions 1 cm x 1 cm. The DOE has different characteristic feature size-groupings and design complexity, from deep to shallow phase steps, and with narrow quasi-one-dimensional structures, as shown in Figure 25. The narrow-angle DOE (Figure 25 (a)) was designed to perform as a 2D spot array generator of 11x7 spots, with a narrow projection full-field of ±1º, with distinguishable deterministic scatter as a result of design optimization constraints and diffraction inefficiency within a field of view of ±5º, excluded from the illumination region. The wide-angle DOE (Figure 25(b)) was designed to perform as a 1D spot array generator of 1x13 spots on a line, with a wide projected field angle of ±5º. The controlled angle DOE (Figure 25(c)) performs as an off-axis segmented annulus projector, with distinguishable zeroth-order at the center of the projected field angle of ±5º.

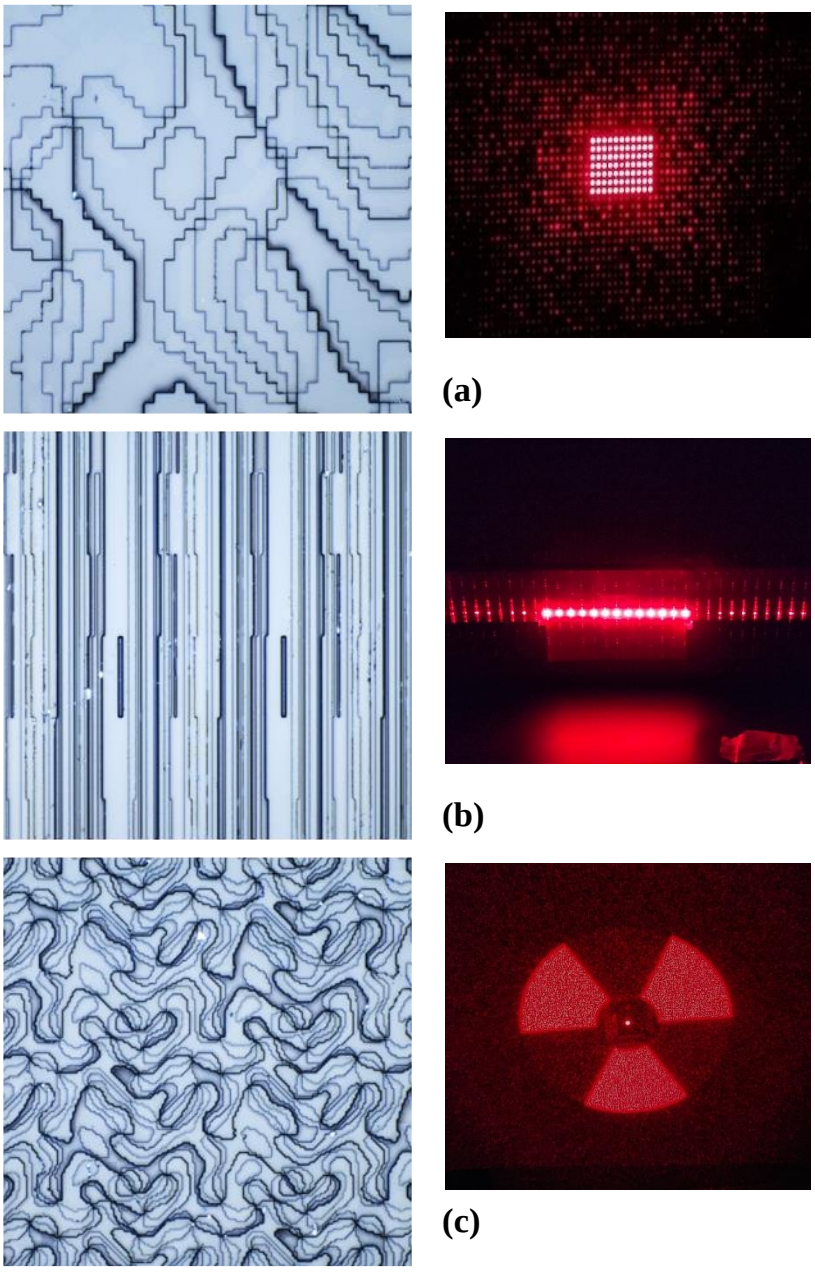

Figure 25 : Top-down UV-confocal microscope images (on the left), and their respective far-filed illumination projection (to the right), of the three multi-phase diffractive optical elements. (a) Narrow-angle 2D spot array diffuser, (b) Wide-angle 1D spot array diffuser and, (c) Controlled-angle diffuser.

The prefabricated DOE were immersed in ethanol for 10 minutes, followed by drying with flowing nitrogen gas. A magnetron driven sputtering deposition tool (AJA 1800-F) was used to deposit a thin discontinuous layer of Au (<20nm) on the backside of the DOE, and the substrate was etched using an STS Advanced Oxide Etcher (AOE). The AOE reactive ion plasma gas mixture had a 50sccm flow rate of sulfur-hexafluoride (SF_6) and 5sccm flow rate of oxygen (O_2), with the platen power at 60W, chamber pressure at 24mT, and chamber temperature at 20ºC. The process etch time was 25 minutes. All DOE, including a fused silica witness flat, were placed in the chamber together to minimize possible variations due to serial processing. The thin non-uniform layer of Au facilitates the initiation of the random etch process, and it is eventually removed by the ballistic action of the non-reactive molecular species bombardment throughout the process. The full process was repeated on the front side of the DOE, using the etching parameters identical to that of the back (flat) surface, in order to evaluate effects of rARSS and process induced topography changes without prior special optimization.

To inspect the fabricated rARSS performance, transmission spectra of the fused silica witness flat was measured. Figure 26 shows the measured transmission intensity spectra of the blank (unprocessed) and single-sided processed witness flat. An enhancement of 3-3.5% was measured for a broad band of 0.55μm to 1.0μm wavelength range.

Scanning electron microscope (SEM) images of the post-processed DOE were taken using a RAITH150 scanning electron microscope. The top-down SEM images of the processed DOE show a uniform formation of rARSS on all phase levels, throughout the surface of the DOE, as shown in Figure 27 and 28. Fabrication of random nanostructures using AOE on the surface of the stepped phase topography did not show any detrimental effects on the

phase features, except the distortion of the side walls for the DOE. These side wall distortions observed for the DOE is because of the reactive plasma action, partially etching the sidewalls during the fabrication of nanostructures. Any alterations to the DOE transverse features sizes and longitudinal phase depth would result in a measurable variation of the designed projection patterns in transmission and reflection. Measurements of these perturbations can give insight into possible undesirable effects of the rARSS on the original DOE profiles.

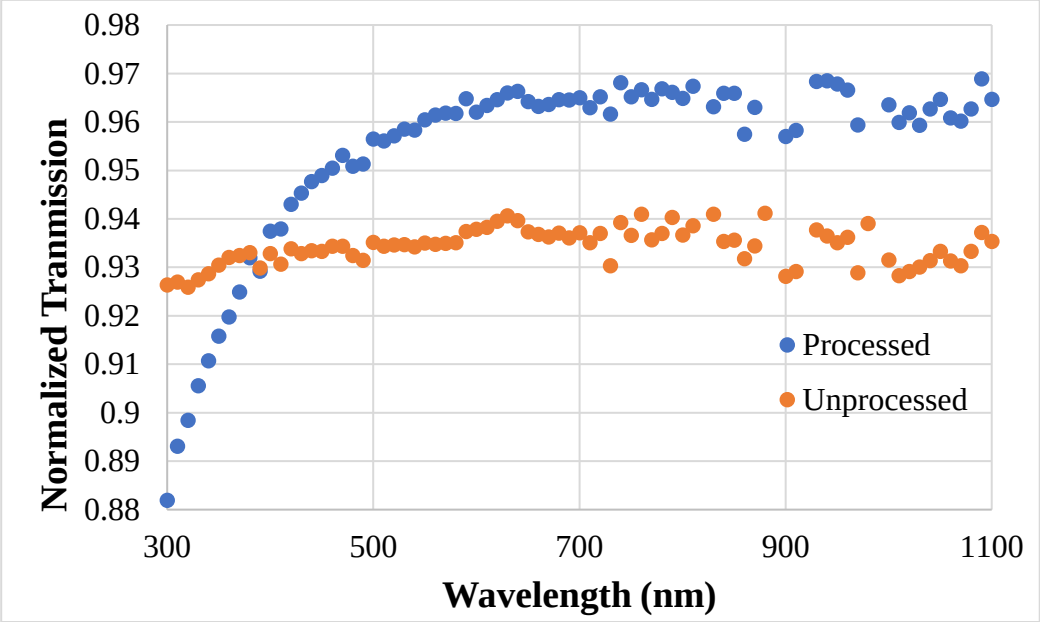

Figure 26 : Measured spectral transmission of a fused silica window before and after fabrication process of rARSS at normal angle of incidence for 0.3µm to 1.1µm.

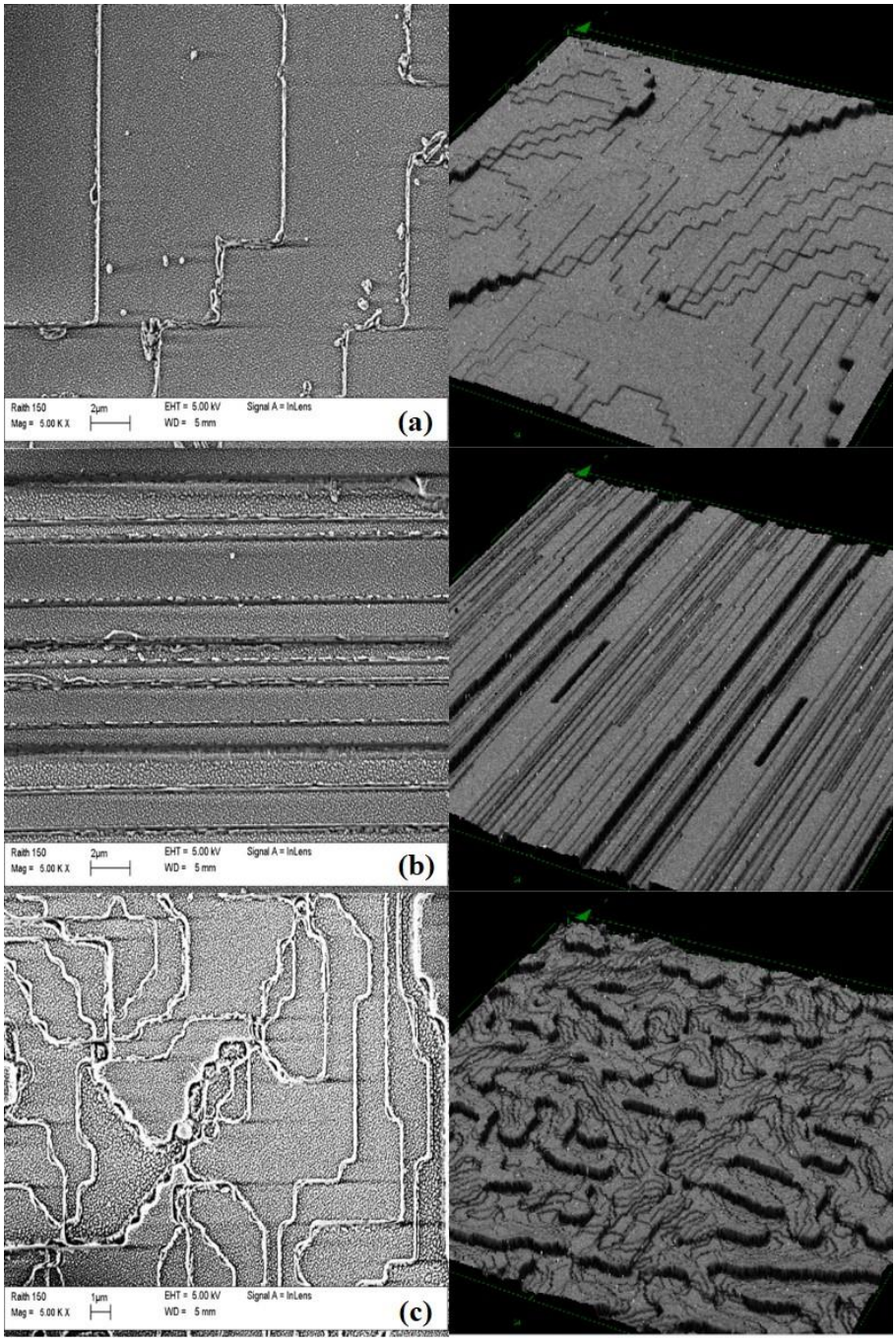

Figure 27 : Top-down scanning electron micrographs (on the left) and UV-confocal microscope stereoscopic images (on the right) of the three multi-phase diffractive optical elements where rARSS have been added. The transverse boundaries are phase transitions between different phase levels which are populated by nanostructures. (a) Narrow-angle 2D spot array diffuser, (b) Wide-angle 1D spot array diffuser and, (c) Controlled-angle diffuser.

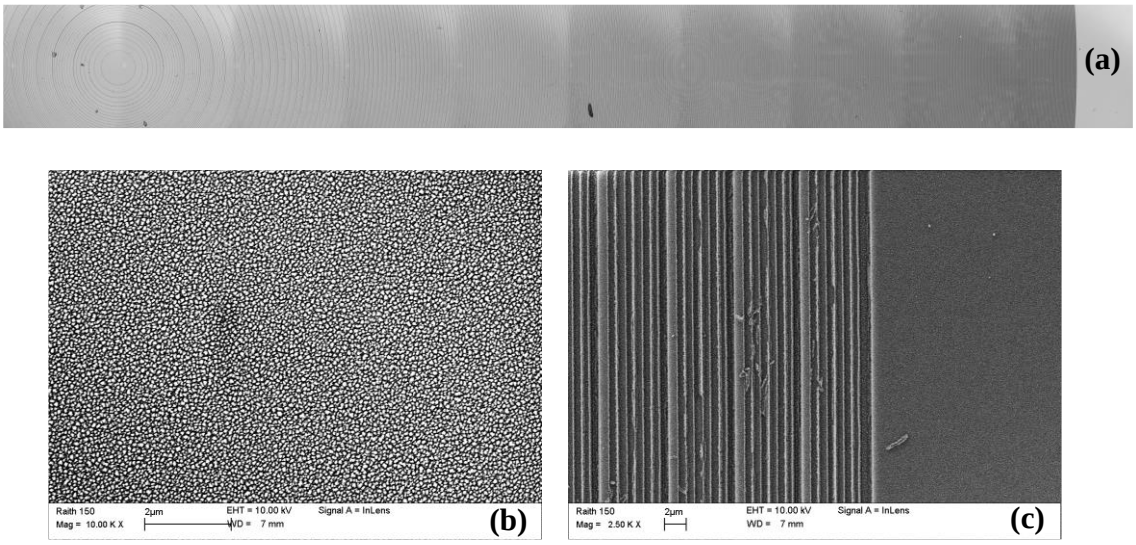

Figure 28 : Top-down scanning UV-confocal microscope image (on the top) and Scanning electron micrographs (on the bottom) of the diffractive Fresnel lens, with added rARSS. (a) Stitched microscope image of unprocessed Fresnel lens from center to edge, (b) Center of Fresnel lens with rARSS and (c) Edge of Fresnel lens with rARSS.

3.3 Performance of Diffractive Optical Elements with rARSS

3.3.1 Introduction

Projection of a specific illumination intensity pattern in the near, or far-field, can be achieved using diffractive optical elements. Such DOE are usually referred to as diffusive-phase illuminators. The radiance pattern is designed by numerically optimizing the phase resulting from a transmitted wavefront, to induce a corresponding diffraction pattern at the desired distance from the optical element. The DOE design process consists of numerical optimization iterations of a candidate phase profile, and the comparison of the computed Fresnel (or Fourier) transforms from the profile with the desired intensity spatial

distribution. This numerical optimization process leads to an incremental diffusion to the desired optical phase distribution. There are numerous adaptive or error-reduction algorithms that have been shown to achieve different levels of fidelity for different desired patterns [61, 62].

Sampling and quantization of the phase profile is restricted by fabrication methods, especially transverse-feature resolution (DOE-plane structure and sampling) and micro-relief height (phase quantization). These restrictions lead to deviations from the designed (computed) profile and result in illumination pattern changes. Any implementation issues, due to the inability to achieve a specified phase profile from the fabrication process, further impact DOE performance. For a pre-fabricated DOE illumination diffuser, it is therefore imperative to preserve the lateral (*x*-*y*) and longitudinal (*h*) morphology of the surface through subsequent processing steps, such as AR thin-film coating deposition or, rARSS nano-structuring. Process-induced height deviations of the DOE profile affect the efficiency of the illumination distribution, whereas transverse feature erosion or dilation changes the radiance distribution. The later increases the undesirable non-deterministic scatter, where the former imbalances the intensity within the projected pattern. In general, the fabricated DOE phase profile $\Phi(x_m, y_l, h_{ml})$ can have the form:

$$\Phi(x_m, y_l, h_{ml}) = \left[\left[\bar{\phi}(x_m, y_l; p_x, p_y, h_{ml})\Pi\left(\frac{x}{c_x}, \frac{y}{c_y}\right)\right] * III\left(\frac{x}{c_x}, \frac{y}{c_y}\right)\right]\left(\Pi\left(\frac{x}{N_x c_x}, \frac{y}{N_y c_y}\right)\right) \tag{11}$$

Where *m*, *l* are DOE *xy*-plane pixel indices, $\bar{\phi}(x_m, y_l, h_{ml})$ is the pixelated quantized phase profile for a pixel size $p_x\ by\ p_y$, $\Pi(x/c_x, y/c_y)$ is the rectangular DOE region that defines

the phase unit cell, $III\left(x/c_x, y/c_y\right)$ is the unit cell replication comb (tiling), $\Pi\left(x/N_x c_x, y/N_y c_y\right)$ is the entire DOE window comprising of *N*-tiled unit cells, and the symbol * indicates the convolution operation. The far-field diffraction intensity pattern of such phase profile is:

$$
\begin{aligned}
I\left(\frac{\sin\alpha}{\lambda}, \frac{\sin\beta}{\lambda}\right) \\
&= \left| K_o \left[\bar{F} \left[\left(\frac{\sin\alpha}{\lambda}, \frac{\sin\beta}{\lambda} \right) \right. \right. \right. \\
&\quad * \operatorname{sinc}\left(c_x \frac{\sin\alpha}{\lambda}, c_y \frac{\sin\beta}{\lambda} \right) \left. \left. \right] III \left(c_x \frac{\sin\alpha}{\lambda}, c_y \frac{\sin\beta}{\lambda} \right) \right] \\
&\quad * \left(\operatorname{sinc}\left(N_x c_x \frac{\sin\alpha}{\lambda}, N_y c_y \frac{\sin\beta}{\lambda} \right) \right) \Bigg|^2
\end{aligned}
\tag{12}
$$

In equation 12 α, β are the planar diffraction angles measured from the DOE surface normal, $\bar{F}(\xi, \psi)$ is the Fourier transform of the DOE phase profile, λ the wavelength of the incident light, and sinc(*z*) is the conventional notation for the ratio of the trigonometric sine function to its argument: sin(*z*)/*z*. The diffraction intensity is expressed using angular variables to relate to directional scatter measured in spherical polar coordinates.

Equation 12 restricts the relations between the physical size of the smallest phase pixel (p_x, p_y), the size of the unit cell (c_x, c_y), and the total spatial extent of the DOE ($N_x c_x$, $N_y c_y$). For a DOE that generates an illumination array of spots, such as the narrow-angle 2D rectangular spot array shown in Figure 25(a), each spot has to be separated by one diffraction order at a minimum, in order to resolve the separation between the spots in the array. The diffraction order separation is controlled by the phase unit-cell sizes (c_x, c_y). The line-shape (point-spread function) of each diffraction order is determined by the total

number of cells repeated within the actively illuminated surface of the entire DOE (N_xc_x, N_yc_y). This is readily shown in Figure 25(b), where 13-diffraction orders are distributed uniformly across a ±5° cone, each having a full-width line-shape of about 0.5°. Lastly, diffraction from each phase pixel (p_x, p_y) will result in the bounding envelop of the angularly distributed intensity. In order to suppress the duplicated diffraction patterns arising from the tiling of the unit-cell, the first null of the diffraction envelop is chosen at or near the boundary of the full diffraction cone. The subsidiary peaks of the point-spread function of the phase pixel dimensions scale the duplicate diffraction patterns. As expected, the relation between the DOE scales is: $p<c<Nc$, and the diffracted angular separation relations are reciprocal: $p^{-1}>c^{-1}>(Nc)^{-1}$. Any disturbance or perturbation of the scale relations mentioned above will result in parasitic orders between the desired choices, or possible reduction of the original efficiency for each order. Etching the DOE existing profile to induce the rARSS nanoscale distribution should not have such undesirable effects. If we consider that the rARSS feature scales could be less than p_x, p_y by at least an average factor of 100, the nanostructures can at an extreme case induce a non-deterministic scattered re-distribution of the projected intensity (halo), that will reduce the transmission contrast performance of the DOE. We note that Fresnel reflection will induce the same diffraction pattern, although much less intense, which will travel to the back surface of the substrate, where upon a second reflection it will return to the DOE surface and multiplex the transmitted pattern.

3.3.2 Experimental setup

To fully characterize the performance of the DOE, unlike simpler diffractive optics such as gratings with multiple diffraction orders, one cannot measure all the propagating orders individually and deduce the effects of rARSS fabrication. To measure the variations in the performance of the DOE, a scatterometer (CASI®, Schmitt Industries Inc.) was used. The schematic of the testing layout is shown in Figure 29 [46]. The scatterometer uses a He:Ne (633nm) laser source, with an adjustable sample mount for variable AOI, and a motorized detector arm capable of full field scans in transmission and reflection. The instrument is capable of measurements at TE, TM, and cross polarization settings, and is equipped with focusing optics and detector varying apertures, calibrated to measure high-resolution scans with a dynamic range of over 8-orders in magnitude. The polarization detection states are defined with respect to the plane of detection. The large dynamic range of the scatterometer

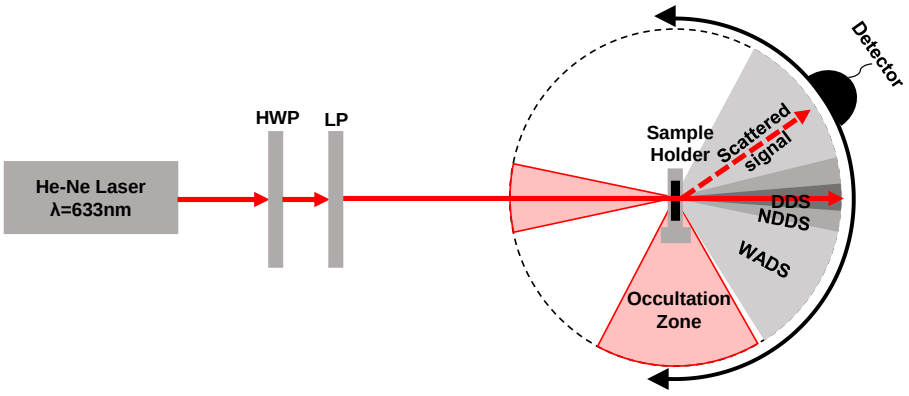

Figure 29 : CASI scatterometer layout. Light from the laser source is directed towards the sample, which is located at the center of the rotating arm apparatus, with the detector scanning over the equatorial plane of the unit sphere. HWP is a half-wave plate, LP is the linear polarizer incidence selector, DDS is the deterministic design spot angular range, NDDS is near design deterministic scatter angular region and WADS is wide-angle deterministic scatter angular region.

results in high-value measure of integrated scatter, which will be discussed in the coming sections. The bidirectional scatter distribution function (BSDF) is defined as a differential ratio of measured radiance to incident irradiance in units of inverse steradians (sr^{-1}) as:

$$BSDF \equiv \frac{dL_c(\theta_c, \varphi_c; \theta_i, \varphi_i)}{dE_i(\theta_i, \varphi_i)} \approx \frac{P_c/\Delta\Omega_c}{P_i \cos\theta_c} \tag{13}$$

Where dL_c, dE_i define the collected differential radiance and incident irradiance; P_c, P_i are the radiant power (from the surface) and incident power on the scattering surface respectively. The angular variables $\theta_c, \varphi_c, \theta_i, \varphi_i$ correspond to the scattered and incident angles, and $\Delta\Omega_c$ is the solid angle of collection subtended by the detector's aperture.

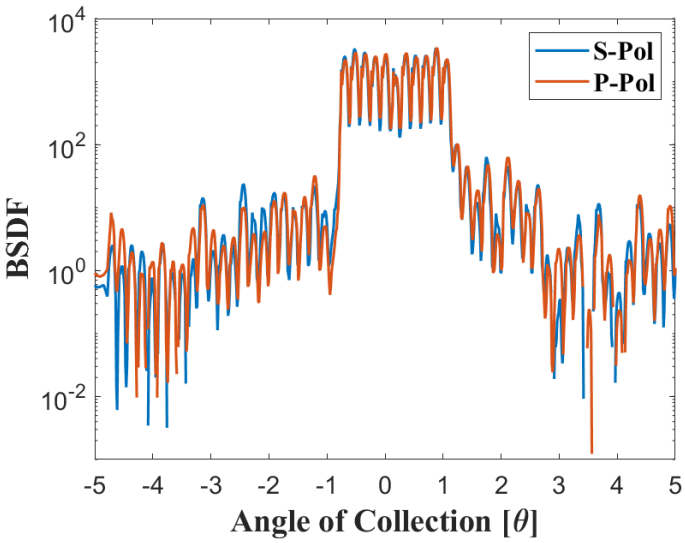

Figure 30 : CASI scatter measurement (BSDF) of the narrow-angle diffuser (2D spot array illumination pattern) for a limited angle (±5°) along the equatorial axis of transmission of the DOE. (Blue) S-polarized and (Red) P-polarized states.

The DOE were tested at normal AOI, as per their application specifications, and since no polarization sensitive behavior was observed (Figure 30), all measurements were limited to the *S*-polarization state.

3.3.3 Transmission and Reflection Measurements

To verify the suppression of Fresnel reflectivity by the addition of rARSS, scatter signatures of the un-processed and rARSS-processed DOE were measured in transmission and reflection. Summing the total transmission and reflection scatter distribution for angles of collection (AOC) off the deterministic projection field of view, is equivalent to the total integrated scatter. The results indicate an overall transmission enhancement and reflection suppression for all the DOE types tested, whereas no significant transmission enhancement was measured along the deterministic projection field of view. In conjunction, because the cross-sectional feature sizes of the nanostructures are 10 to 15 times smaller than the test wavelength, no distinguishable redistributed scatter was observed in the off-specular deterministic directions, with the scatter signatures being nearly identical for unprocessed and processed DOE.

A perfectly matched AR coating (PAR) on both surfaces of a fused silica optical window can yield a relative transmission of ($1/0.93 \approx 1.075$) and relative reflectivity of ($0/0.07 \approx 0$) at 633nm wavelength. To compare the measured transmission and reflection of the unprocessed and rARSS-processed DOE, the data was segregated in three parts: a) the deterministic design region (DDS) for an AOC range of $-1^{o} \leq \theta \leq +1^{o}$; b) the near-angle deterministic scatter (NDDS) for an AOC range of $-5^{o} \leq \theta \leq -1^{o}$ and $+1^{o} \leq \theta \leq +5^{o}$ (excluding the design angular region); and c) the wide-angle deterministic scatter region (WADS) for an AOC range of $-65^{o} \leq \theta \leq -5^{o}$ and $+5^{o} \leq \theta \leq +65^{o}$, excluding both previous scatter angular regions. These regions are illustrated as shaded in Figure 29.

Table 1. Integrated transmission scatter intensity for the original diffusers (Blank) and the rARSS post-fabrication diffusers in design (DDS) and near design specular (NDDS) AOC.

DOE	DDS			NDDS		
	Blank (sr^{-1})	rARSS (sr^{-1})	Enhancement Fraction	Blank (sr^{-1})	rARSS (sr^{-1})	Enhancement Fraction
A	4.71 (10^5)	5.00(10^5)	1.06	3.50(10^3)	3.26(10^3)	0.918
B	4.35(10^5)	3.74(10^5)	0.86	-	-	-
C	3.80(10^4)	6.66(10^4)	1.74	4.70(10^3)	4.20(10^3)	0.885

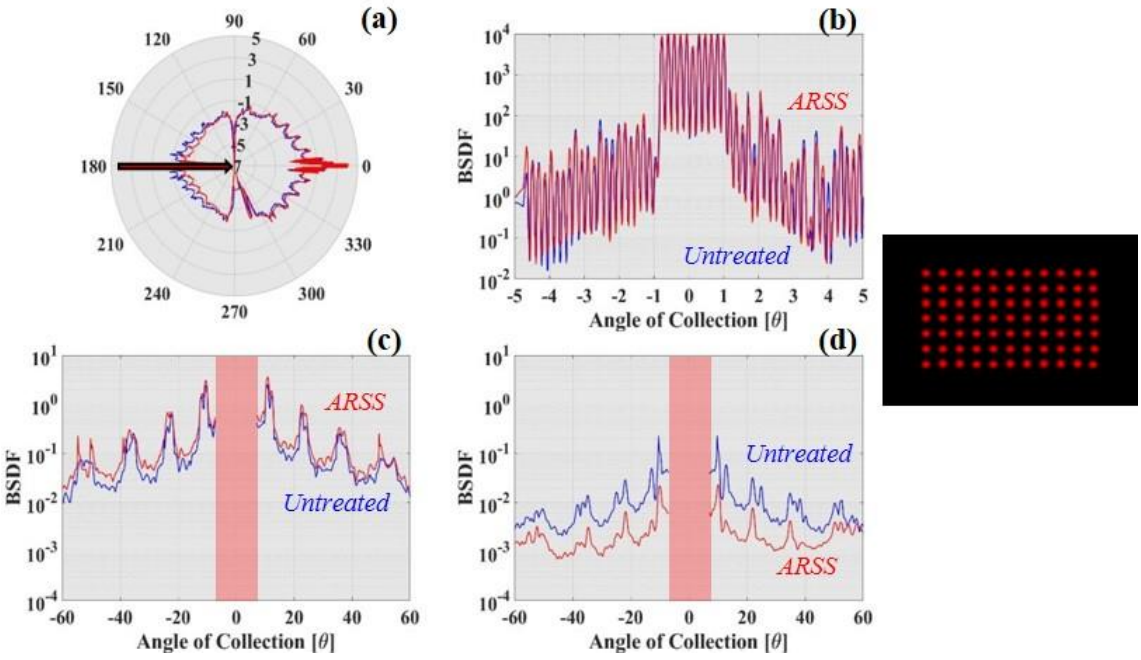

Figure 31 : CASI scatter measurement (BSDF) of the narrow-angle diffuser (2D spot array illumination pattern on the right). (a) Full-polar plot of tested DOE. The DOE to be tested is located at the center of circle. The incident light direction is shown with a dark arrow. (b) Limited angle (±5º) along the equatorial axis of transmission of the DOE, (c) Measured transmission excluding the ±5º values. (d) Measured reflection excluding the ±5º values. The ±5º FOV (DDS+NDDS region), indicated as a shaded band region here, has been removed from the plots (c) and (d) for clarity.

Table 1 lists the angle-integrated normalized transmission of unprocessed and processed DOE, and the relative transmission enhancement defined as the ratio of processed over

unprocessed angle-integrated transmission within the DDS and NDDS regions. The three tested DOE are listed as samples: **A** for the narrow-angle 2D spot array, **B** for the wide-angle 1D spot array and, **C** for the controlled angle diffuser. They show disparate results with a slight enhancement in transmission for **A** in DDS and loss in NDDS region as shown in Figure 31, while for **B** a loss was observed in DDS and NDDS region as shown in Figure 32. For **C** a disproportionate enhancement for the zeroth order in DDS and loss in NDDS region were measured, shown in Figure 33.

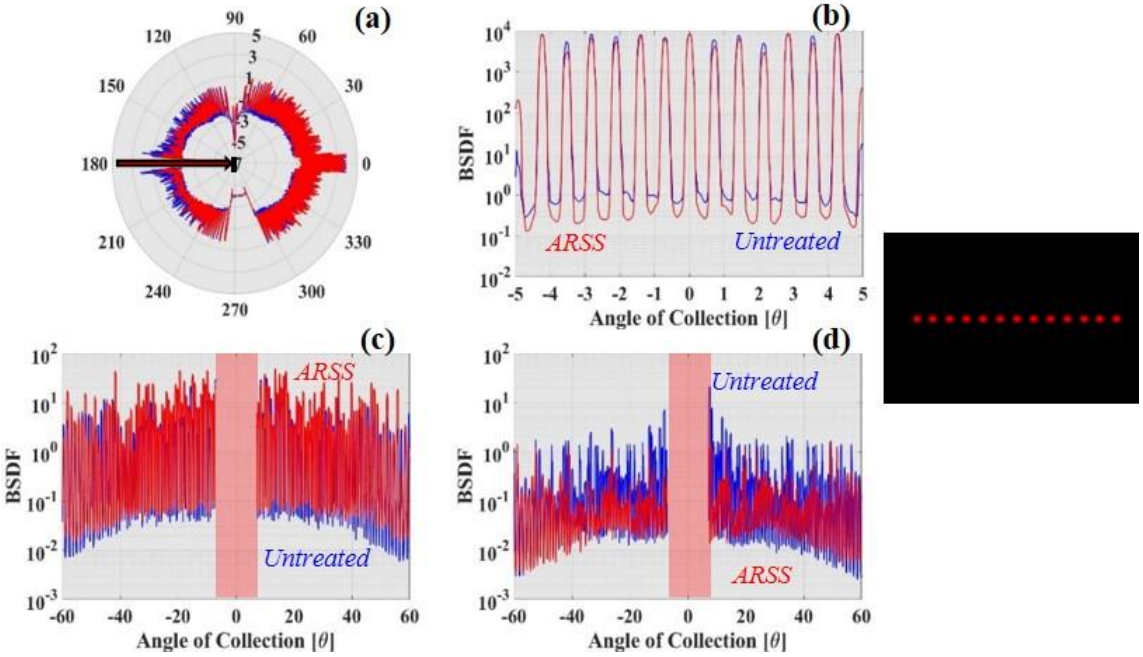

Figure 32 : CASI scatter measurement (BSDF) of the wide-angle diffuser (1D spot array illumination pattern on the right). (a) Full-polar plot of tested DOE. The DOE to be tested is located at the center of circle. The incident light direction is shown with a dark arrow. (b) limited angle (±5º) along the equatorial axis of transmission of the DOE, (c) Measured transmission excluding the ±5º values. (d) Measured reflection excluding the ±5º values. The ±5º FOV (DDS+NDDS region), indicated as a shaded band region, has been removed from the plots (c) and (d) for clarity.

Table 2 lists the angle-integrated normalized transmission and reflection, and relative transmission enhancement and reflection suppression for the unprocessed and processed WADS region. Unlike the DDS and NDDS regions, a clear enhancement in transmission and suppression in reflection was measured for all DOE. For the 2D spot array (**A**) and 1D spot array (**B**), almost half an order of magnitude in transmission enhancement was observed, compared to the controlled angle diffuser (C) which is only a quarter of an order in magnitude. In reflection, a consistent suppression of an order of magnitude was measured in all cases. The deviation in results for the WADS compared to DDS and NDDS regions could be attributed to phase depth errors due to the subtractive nature of the etching process employed for the fabrication of rARSS on the surface of DOE, and not due to the presence of rARSS.

Table 2. Integrated transmission and reflection scatter intensity for the original diffusers (Blank) and the rARSS post-fabrication diffusers in wide-angle deterministic scatter (WADS) AOC.

DOE	Transmission			Reflection		
	Blank (sr^{-1})	rARSS (sr^{-1})	Enhancement Fraction	Blank (sr^{-1})	rARSS (sr^{-1})	Suppression Fraction
A	90.0	$1.27(10^2)$	1.47	6.90	1.42	0.204
B	$5.70(10^3)$	$1.02(10^4)$	1.78	$2.40(10^3)$	$3.55(10^2)$	0.147
C	51.0	65.0	1.28	12.0	1.40	0.115

To compare rARSS effects in transmission and reflection of the deterministic radiance profiles, scatter scans measured pre- and post-etch are shown in the Figures 31, 32 and 33 for the entire equatorial plane. Low radiance angular replicas were detected for all DOE, due to their respective periodic unit cells. It is evident from the polar plots of the DOE scatter signatures that the addition of rARSS has not perturbed the wide-angle deterministic scatter,

and the periodic replicas, which are non-zero due to the finite numerical optimization residuals, are clearly distinguishable at wide angles of collection. In Figure 31(b) the narrow-angle 2D spot array radiance within the designed axial deflection angle ±1°, displays no major deviations in uniformity, contrast and spot sizes, between before and after the nanostructures addition. In contrast, the wide-angle spot array as shown in Figure 32(b), which has diffractive feature sizes and sharp phase transitions compared to the narrow-angle diffuser, effects show significant effects of non-uniformity and increased contrast after

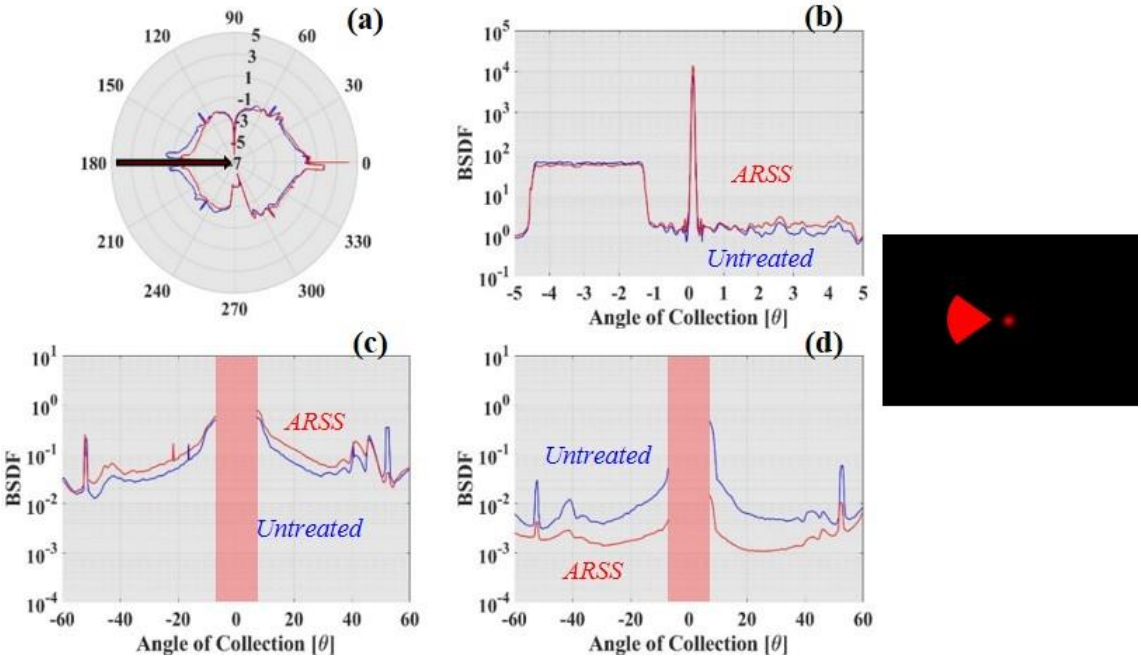

Figure 33 : CASI scatter measurement (BSDF) of controlled-angle diffuser (illumination pattern on the right). (a) Full-polar plot of tested DOE. The DOE to be tested is located at the center of circle. The incident light direction is shown with a dark arrow. (b) limited angle (±5°) along the equatorial axis of transmission of the DOE, (c) Measured transmission excluding the ±5° values. (d) Measured reflection excluding the ±5° values. The ±5° FOV (DDS+NDDS region), indicated as a shaded band region, has been removed from the plots (c) and (d) for clarity.

rARSS addition, for all projected spots, even though the transverse spot sizes have remained unperturbed.

At large angles of collection, rARSS enhanced wide-angle diffuser (**B**) is not as effective in suppressing reflection, compared to the narrow angle diffuser (**A**) as shown in Figure 31(d) and 32(d). The controlled angle diffuser (**C**) has a more complex topographic phase profile compared to the other two DOE (Figure 25), and its transverse feature size dimensions are smaller than the features of **A**, but larger than the features in **B**. For **C**, the measured reflection and transmission at wide-angles of collection has similar performance between the original and rARSS-inclusive element to that of A and B (Figure 33(c), 33(d)). A considerable increase in the 0th-diffraction order intensity was measured for the controlled angle diffuser post-rARSS addition, which indicates an overall DOE phase imbalance, due to post-etching perturbations of the relative depths of the DOE surface (Figure 33(b)).

3.4 rARSS Enhanced Diffractive Fresnel Lens

3.4.1 Introduction

Diffractive phase Fresnel lenses, unlike the computer-generated DOE discussed in the previous section, are a form of spherical-phase inducing elements, which are segmented into zones of quadratic-scale grating periods, increasing the spatial frequencies of the features, from center-to-edge with each zone modulating the incident wavefront by a phase shift of 2π, as shown in the Figure 34. The Diffractive phase Fresnel lens zones are rotationally

symmetric, with the annual radius ($r_{m.g}$) of any number of phase steps in a specific zone given in the small-angle approximation as:

$$r_{m.g} = [2\lambda f(m - 1 + g/L)]^{1/2} \tag{14}$$

Where m is the index of zone number, g is the phase step index number varying from $g = 0$ (for inner radius of the zone) to $g = L$ (outer radius of the zone), λ is the incident light wavelength and f is the focal length.

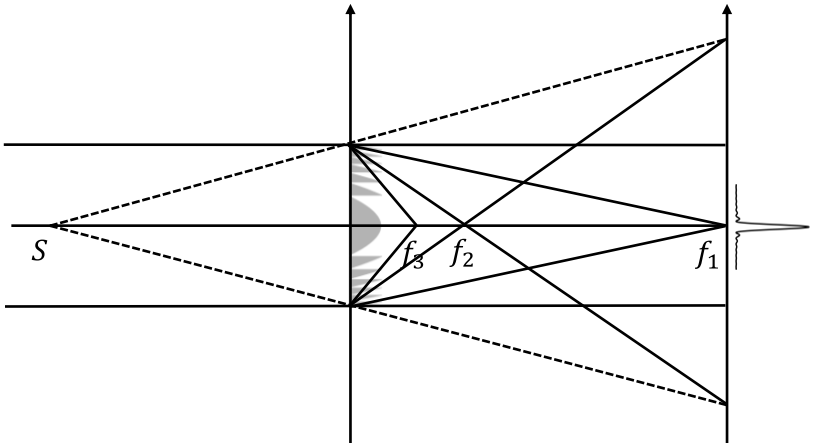

Figure 34 : Graphical depiction of transmitted light distribution through a diffractive Fresnel lens. S is the source, f_1 is the primary focal point and f_2 and f_3 are the secondary and tertiary focal points.

Process-induced deviations, due to fabrication of rARSS on the transverse higher spatial frequency features of the Fresnel lens profile, can impact the spot size of the focused beam, while deviations in the height of the features can affect the efficiency of the illumination distribution for the designed wavelength. In general, the Fresnel lens phase profile is represented as a Fourier series and its far field intensity distribution is given as:

$$f(r^2) = \sum_{n=-\infty}^{+\infty} C_n exp(-i2\pi r^2/r_l^2) \tag{15}$$

$$I(z_n, \rho) \approx |C_n|^2 n^2 \left(\frac{\pi d^2}{4}\frac{1}{\lambda f}\right)^2 \left(2J_1\left(\frac{\pi d\rho}{\lambda z_n}\right)/\frac{\pi d\rho}{\lambda z_n}\right)^2 \tag{16}$$

3.4.2 Experimental setup

To test the Fresnel lens, an experimental setup shown in the Figure 35 was used. The experimental setup consists of multiwavelength He-Ne laser source, which is passed through a pair of half-wave plate and linear polarizer to control the polarization of the input beam. The beam is further passed through a beam expander to produce an expanded beam of uniform intensity, which is incident on the Fresnel lens at normal angle of incidence. A standard silicon photodetector (S120C THORLABS) was used to measure the transmission and reflection intensities, and a CCD detector (BC-106N-VIS) to measure the beam profiles at the front and back focal spots.

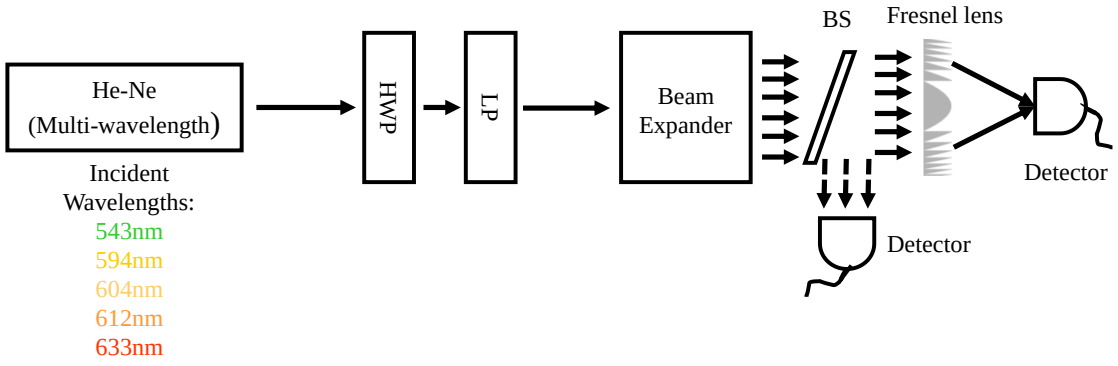

Figure 35 : Layout of the optical setup used to measure efficiency of the diffractive Fresnel lens at various incident wavelengths. Polarization of the incident light is controlled by a pair of Half-wave plate (HWP) and linear polarizer (LP), and a beam splitter (BS) was used for reflection measurements.

The diffractive Fresnel lens tested was designed and fabricated for an incident wavelength of 633nm. Certain performance characteristics of Fresnel lens are wavelength dependent, such as the principal focal point difference $(\lambda f = constant)$. These characteristics separate diffractive Fresnel lens wavelength sensitivity from the diffractive diffuser wavelength efficiency, as shown earlier in this study. Any variations in the transverse spatial frequencies of the phase Fresnel lens, because of rARSS fabrication would result in inconsistencies for the above-mentioned relation, and can be verified through focal distance measurements pre- and post-fabrication of rARSS.

Table 3. Measured focal point distances of the diffractive Fresnel lens pre- and post-fabrication of rARSS at multiple incident wavelengths (543nm, 594nm, 604nm. 612nm, 633nm) and normal angle of incidence.

Wavelength (nm)	Focal point distances	
	Pre-fabrication (cm)	Post-fabrication (cm)
543	5.91	5.91
594	5.46	5.46
604	5.36	5.36
612	5.26	5.26
633	5.11	5.11

Table 3 lists the focal length measurements at various wavelengths pre- and post-rARSS fabrication. Since the phase Fresnel lens is rotationally symmetric, the focal lengths were measured for both *S* and *P* polarizations and averaged. The experimental measurements show no deviations post fabrication, confirming the high spatial frequency regions of the lens have remained unaffected, similar to the DOE shown in Figure 28.

3.4.2 Transmission, Reflection and Beam Profile measurements

To verify the suppression of Fresnel reflections because of rARSS presence, the reflected efficiency of the phase Fresnel lens was measured pre- and post-fabrication, for both polarizations (*S* and *P*) and averaged. The measured transmission and reflected efficiency of the original and the rARSS enhanced Fresnel lens are shown in the Table 4. A significant suppression in reflection, on an average of about half-an-order of magnitude was observed for the rARSS enhanced diffractive Fresnel lens at all measured wavelengths. However, no quantifiable enhancement was observed in transmission for the measured wavelengths. These observations are consistent to the DOE measurements presented in the previous section, where a minimum loss with a relative transmission of 0.911 was observed for 633nm and maximum loss with a relative transmission of 0.857 was observed for 543nm. While the experimental measurements have shown the fabrication of rARSS on the Fresnel lens have not affected the transverse spatial frequencies in the Fresnel zones, the drop in the efficiency of the lenses in transmission could be a result of phase depth mismatches similar to what was observed for the phase diffusing DOE.

Table 4. Transmission and reflection intensity measurement for the original (Blank) and the rARSS post-fabrication Fresnel lens at normal angle of incidence.

Wavelength (nm)	**Transmission**			**Reflection**		
	Blank (mW)	rARSS (mW)	Enhancement Fraction	Blank (μW)	rARSS (μW)	Suppression Fraction
543	86.45	74.16	0.857	25.4	5.29	0.212
594	85.27	74.62	0.875	81.8	18.3	0.224
604	85.43	75.49	0.883	73.6	13.13	0.178
612	87.11	76.17	0.874	129.5	19.6	0.151
633	84.97	77.46	0.911	186	31.9	0.172

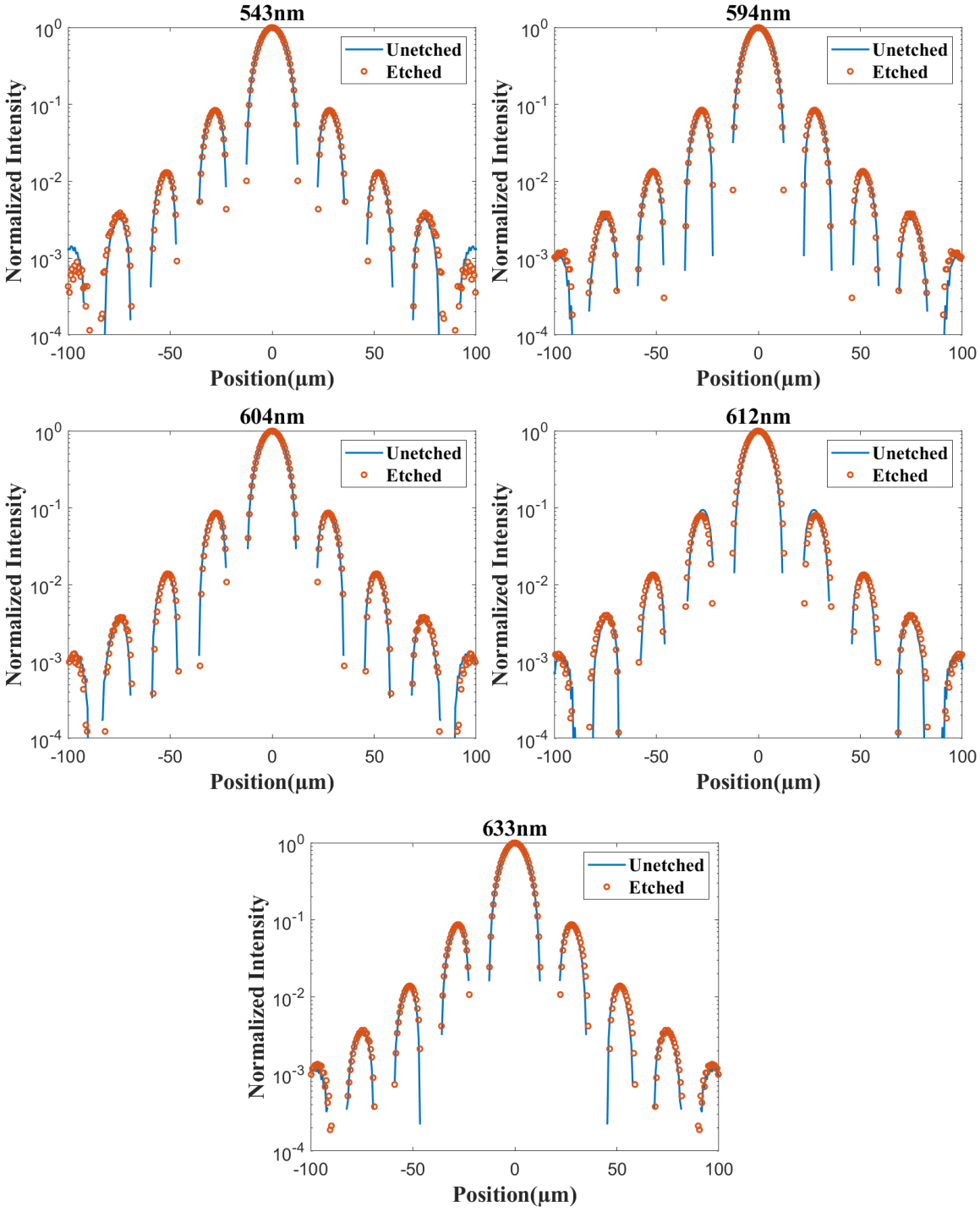

Figure 36 : Measured cross-sectional beam profile of the diffractive Fresnel lens, for five wavelengths at their respective focal points. Solid lines indicate unprocessed and circle markers indicate rARSS processed measurements.

To analyze any variations in the performance of the multi-phase level diffractive Fresnel lens due to the presence of rARSS, Beam profiles of the lenses at the focal spots were measured for the original and rARSS enhanced lens, using a CCD camera beam profiler (BC106N by THORLABS). A beam expander was used to produce an expanded beam of uniform intensity which was incident on the lens, and the beam profiles were measured for 5 different wavelengths at their respective primary focal lengths as shown in Figure 36. No differences in the beam profiles were observed for all the incident wavelengths for rARSS processed lens in comparison to the original performance of the lens.

3.5 rARSS Granulometry

Measurements post-fabrication of rARSS on the DOE compared to the unprocessed originals show some changes in their performance. To investigate further, granulometry was employed to study the distributions of the rARSS nanostructure transverse cross-sectional scales. Since the structures have small cross-sectional dimensions, mechanical contact profile and microscope measurements cannot resolve their structure. Granulometry, a numerical processing technique was used to identify the boundaries and define scaled structure elements from SEM images [43]. Top-down high-resolution SEM micrographs were obtained to calculate the normalized granule pattern spectra $\varphi(k)$, for both islands and voids of diameter k. The granule pattern spectra correspond to the discrete probability distribution function of the respective feature size bound by the condition:

$$\varphi_{islands}(k) + \varphi_{voids}(k) \leq 1 \tag{15}$$

The equality is true only for $k = \infty$, i.e., when all the feature diameters are counted, and a balance of the islands and voids is obtained for each SEM image. The DOE tested have by design varying topographies and 3D-feature sizes, independent of the nanostructures. To verify the effects of the surface topography on the rARSS fabrication process, we counted the discrete probability distribution of rARSS cross-sectional-size populations on the witness flats and all the DOE's using sampled SEM images. The measured histograms, shown in Figure 37, show similar island distributions across all

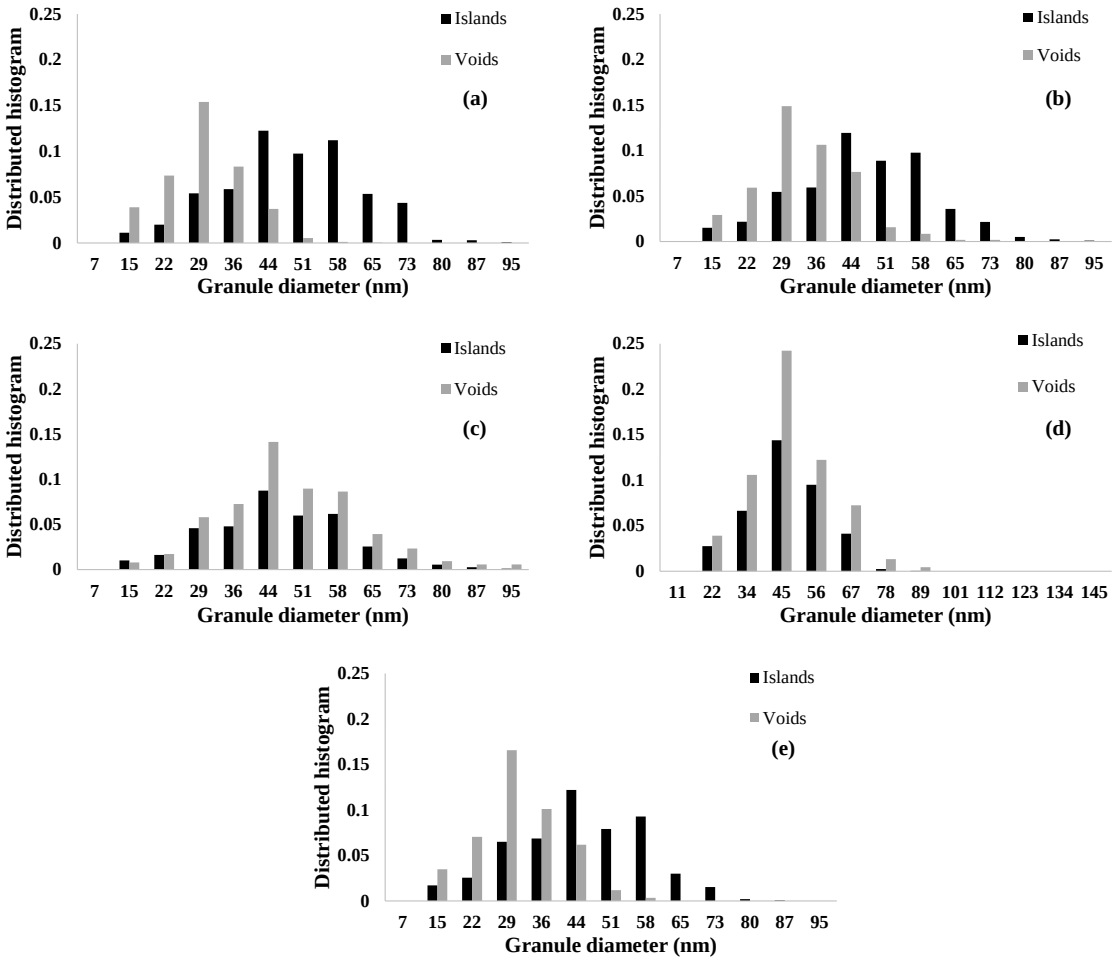

Figure 37 : Distributed histograms of the islands (black) and voids (grey) measured from SEM images using granulometry. (a) Narrow angle diffuser (2D Spot array **A**), (b) Wide-angle diffuser (1D Spot array **B**), (c) Controlled angle diffuser (**C**), (d) Diffractive Fresnel lens and (e) Witness fused silica optical window.

DOE, with feature size mean values of about 45nm. The distributed histograms of voids were observed to be segregated into two groups, with similar distributions for narrow and wide-angle diffuser surfaces, and the controlled angle diffuser and diffractive Fresnel lens populations. A significant deviation of the void-size peak value was detected for the controlled angle diffuser and Fresnel lens (45nm), when compared to the flat witness or the other two DOE, with a corresponding void peak value of 29nm. The measured cumulative distribution of the islands for the witness, narrow-angle diffuser and wide-angle diffuser was calculated to be approximately 51%, whereas for the controlled angle diffuser and Fresnel lens is 40%, indicating differences in the density of the nanostructures fabricated on the surface. The variations in the distributed histograms and cumulative distributions of rARSS signify differences in the fabrication process equilibrium as a function of the DOE existing phase-surface topography.

3.6 Optical Scatter characterization of rARSS

3.6.1 Optical Flats

Anti-reflective structured surfaces although suppress Fresnel reflections, are inherently rough compared to optical quality thin film coatings. While absence of the non-deterministic scatter due to the rARSS on the DOE was observed in the previous sections, a study to understand the scatter effects due to the presence of rARSS is important for their applications as an effective AR treatment. Optical roughness and the effect on incident radiation has been an area of interest for many years, and several studies have been conducted to understand any potential detrimental effects. Traditionally surface features

have been classified by their spatial frequency content: low-spatial frequency structures referred to as figure errors, result in the redistribution of the energy within the paraxial regions causing blurring of the image core; while high-spatial frequency structures, referred to as finish errors, tend to scatter energy from the paraxial region to wide angles, resulting in loss of contrast. Mid spatial frequencies structures fall in between figure and finish errors referred to as mid spatial frequency errors [46, 63-65].

To study the scatter characteristics of rARSS, BSDF measurements of the fabricated rARSS on fused silica optical windows was measured, for the full equatorial field of view at various AOI. The result show that the sub-wavelength AR structure random distributions induce a continuous and uniform distribution of energy for higher angles of collection, when compared to the measurements from fused silica optical blank windows. The BSDF was found to be shift-invariant with respect to the angle of incidence as shown in Figure 38. Since the measured samples where optimized to have high transmission at the measured

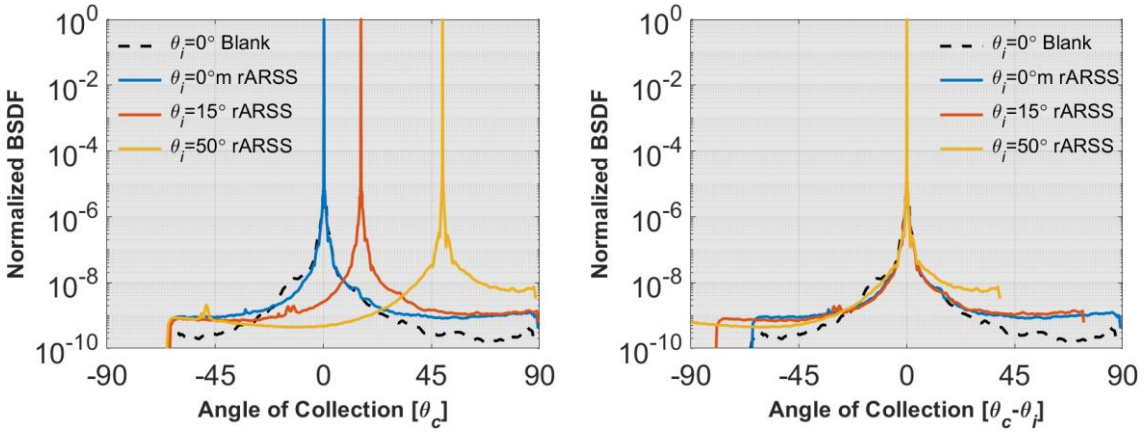

Figure 38 : Bidirectional distribution function (BSDF) measurements at 633nm wavelength. (Left) Optical flat with and without sub-wavelength structures for various angles of incidence and, (Right) shift-invariance relation of the BSDF as a function of the angle of incidence.

wavelength, the measured wide-angle scatter was observed to have high contrast, lower by 9-orders in magnitude compared to the axial transmission value. This high contrast masked any effects on the diffractive diffusers with the complicated illumination patters.

Simulations of propagating diffraction intensity angular spectra for the Dammann gratings show that increasing complexity of the nanofeature distributions improve AR performance, and seem to channel energy into the axial diffraction order. Additionally, the intensity diffracted intensity in the higher orders is detected as uniform, as shown in the Figure 39. These results align with the BSDF measurements of the highly transmissive rARSS samples, indicating cooperative scattering properties of the high spatial frequency

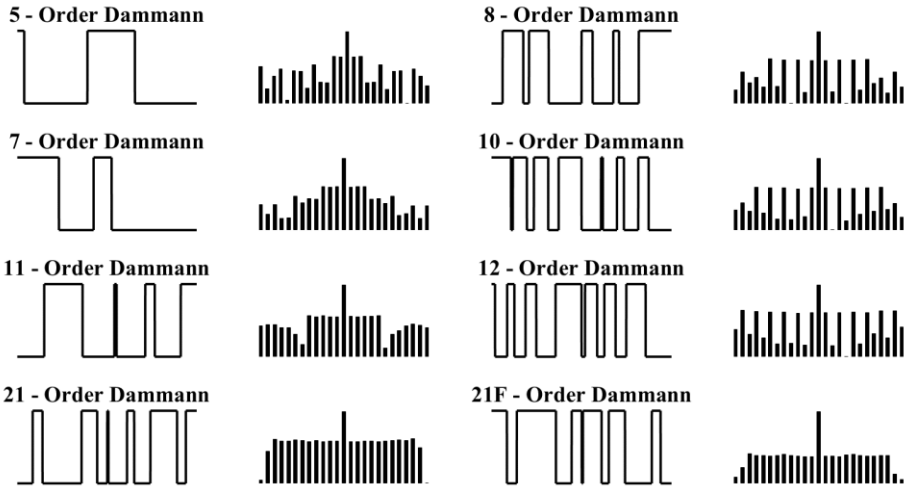

Figure 39 : Cross-Sectional view of 1-dimensional, normalized N-order Dammann binary-phase grating profiles, within their periodic unit cell p_x, along with their corresponding far-field intensity pattern for fused silica substrate in log-scale. (Left column): Odd-order Dammann gratings with volume fractions comparable to $f^{(TE)}$ requirements. (Right column): Even-order Dammann gratings with volume fractions comparable $f^{(TM)}$to requirements. The last entry is a reversed-tone grating to match TM conditions.

rARSS, unlike the non-cooperative scattering resulting in loss of energy from the core (axial-orders) to higher collection angles (higher prorogating orders).

3.6.2 Near wavelength gratings

Results from the previous section show that the presence of rARSS on fused silica optical windows results in reduced uniform scatter at higher angles of collection. Although the scatter effects observed due to the presence of rARSS on the optical windows were minor, it is important to study the effects of rARSS on segmented phase profiles as well. The BSDF of two commercially available, near-wavelength period (1.595µm and 1.166µm) gratings was measured, pre- and post-fabrication of rARSS using the scatterometer. The scans are shown in Figure 29, for normal incidence, 1st Bragg and 2nd Bragg AOI in transmission and reflection. The binary gratings were chosen because their near-wavelength periodicity generates a limited number of propagating orders. Due to larger angular separations between the orders at the far-field, all the propagating diffraction order intensity angular distributions can be approximated with a spectrum of independent plane waves, ignoring the cross-coupling terms between them.

The measured scatter distribution of the near wavelength gratings was observed to match the previously reported intensity suppression and enhancement for propagating orders in reflection and transmission for all the angles of incidence. Comparing the results for both gratings, at all angles of incidence conditions, some similarities in scatter distributions were observed in transmission and reflection as shown in Figure 40 and 41 [66]. The “blank” grating (without rARSS) measurements show order separation by

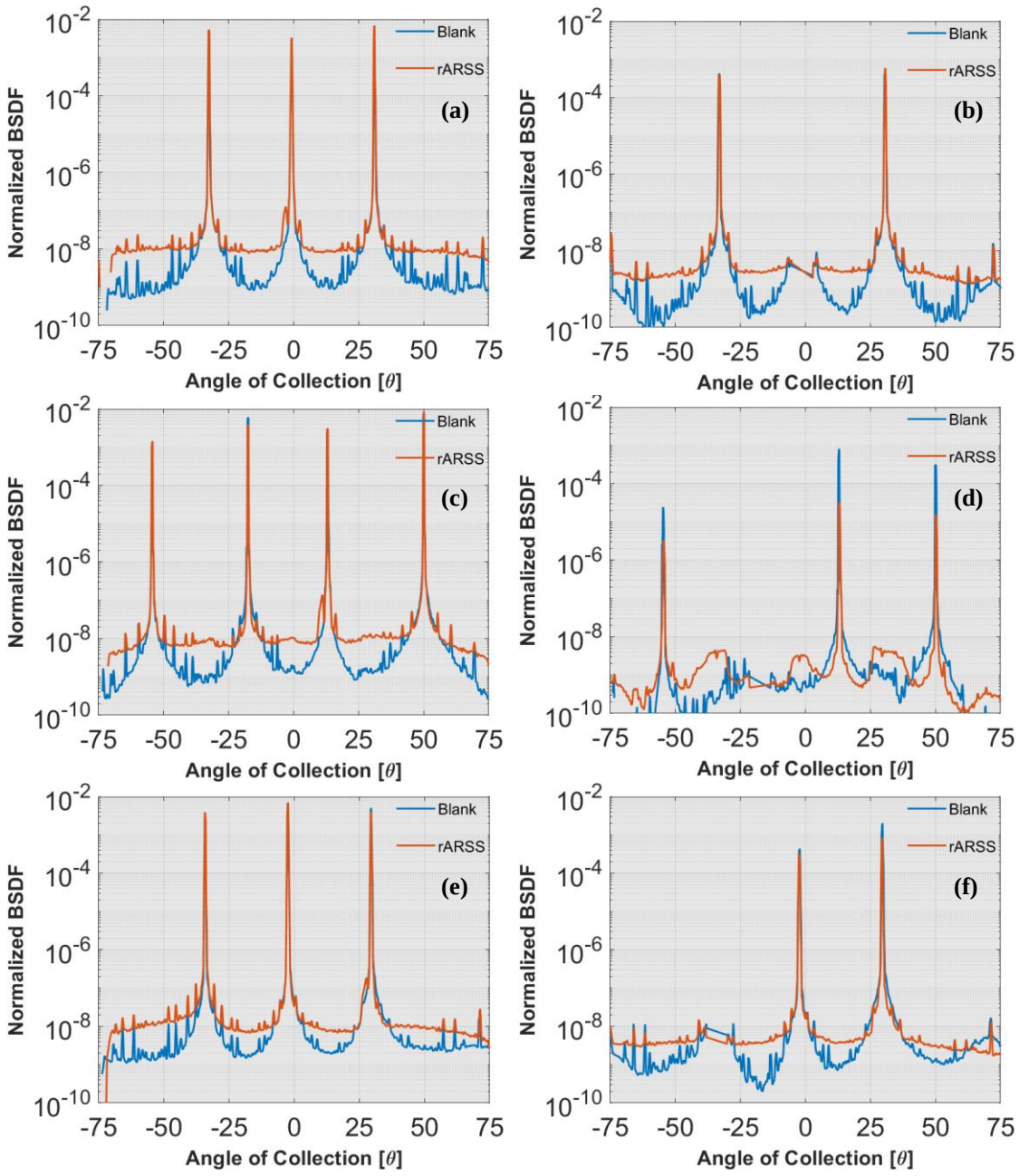

Figure 40 : Bi-directional distribution function (BSDF) measurements normalized to total energy for the 1.166µm period gratings for transmission (left) and reflection (right) represented in logarithmic scales, where the Blank grating represented in blue, the rARSS processed grating is represented in red at various angle of incidences. (a) and (b) normal AOI, (c) and (d) 1st Bragg AOI and (e) and (f) 2nd Bragg AOI.

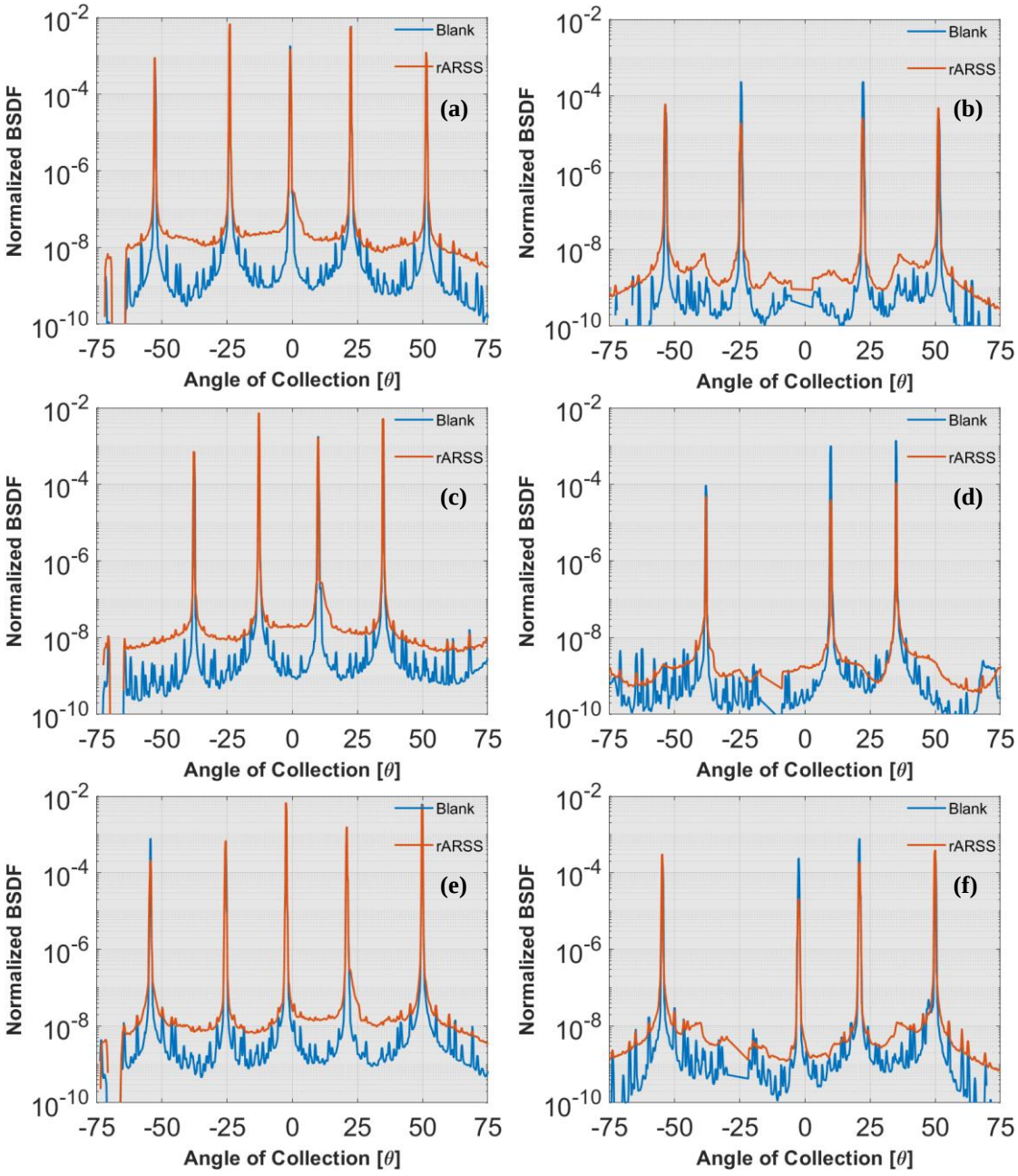

Figure 41 : Bi-directional distribution function (BSDF) measurements normalized to total energy for the 1.595µm period gratings for transmission (left) and reflection (right) represented in logarithmic scales, where the Blank grating represented in blue, the rARSS processed grating is represented in red at various angle of incidences. (a) and (b) normal AOI, (c) and (d) 1st Bragg AOI and (e) and (f) 2nd Bragg AOI.

regions of low intensity, ranging from 10^{-8} to 10^{-9} in magnitude for transmission, and 10^{-9} to 10^{-10} in magnitude in reflection. These regions were observed to have concave radiance spatial distributions, with fine peak structures with considerable contrast to the underlying background, anchored to either side of the propagating diffraction orders. The structured peaks observed between diffraction orders are because of Fresnel induced reflection feedback of the propagating orders from the grating's surface to the planar surface (backside) and back. The contrast of the back reflections was seen to be stronger for the larger period grating (1.595μm), for all angles of incidence compared to smaller period grating (1.166μm). The rARSS-processed gratings show an intensity homogenization within the angular regions in between the orders of about 10^{-8} and 10^{-9} in magnitude for transmission and reflection, similar to what was observed for optical windows with rARSS at higher angles of collection, and result in considerable reduction of contrast between the structured intensity peaks and the diffracted orders, because of feedback from the front and back surfaces. This intensity homogenization is a direct consequence of convolution of scatter characteristics of rARSS with the binary gratings, and can be estimated from the optical fused silica window measurements. Even though the added non-deterministic scatter caused by the rARSS into the optical system is minimal, care needs to be taken for imaging applications, which can be sensitive to multiple scatter between cascaded elements.

3.7 Conclusions

The performance of random antireflective subwavelength surface structures fabricated on the three diffractive diffusers was characterized using a scatterometer. The phase

Fresnel lens enhancement was determined using a beam profiler and power measurements in transmission and reflection. The rARSS were fabricated on these optical components using a two-step process, with an initial masking step followed by reactive ion plasma etching. The measured bidirectional scatter distribution function of the rARSS enhanced DOE show similar signatures compared to unprocessed DOE of the same design, with individual periodic replicas and off-target design deterministic scatter remaining unaltered by the presence of the nanostructures.

The measured integrated wide-angle deterministic scatter intensities for the three diffractive diffusers with rARSS show an order of magnitude suppression in reflectivity compared to the original performance. The integrated deterministic design spot transmission scatter intensity measurement shows an enhancement for the narrow angle and controlled angle diffuser, while a loss results for the wide-angle diffuser post-fabrication. A consistent enhancement in wide angle deterministic scatter intensities was observed for all diffusers. Due to the measured disparities, in transmission enhancement and reflectivity suppression for wide-angle deterministic scatter, compared to the deterministic design spot and near design deterministic scatter, the scatter was analyzed for any detectable diffuse light presence due to the rARSS addition. For the designed illumination patterns, the diffuser with large-size spatial features (such as the narrow-angle diffuser 2D spot array **A**) show no deviations in performance, whereas the wide-angle diffuser (1D spot array **B**) shows an increase in non-uniformity. Significant increase in the on axis 0th-diffraction order was observed for the controlled angle diffuser **C**. Even though differences in the design illumination pattern were observed, no distinguishable non-deterministic scatter was observed, with the design target spot sizes and contrast of the

illumination spots and radiance copies remaining unperturbed. The diffractive Fresnel lens shows similar trends in transmission and reflection, comparing the pre- and post-fabrication rARSS results. A suppression in reflection of about half-an-order of magnitude and loss in transmission for all the measured wavelengths was observed. The beam profiles for the measured wavelengths, at their respective focal points, have remained unchanged with no observable deviations in intensity distributions. These results suggest that variations in the performance of the four DOE tested post-rARSS fabrication, are due to relative phase depth erosion caused by the etching process.

The performance deviations between the four phase diffusing DOE tested, appears to be affected by their dissimilar surface topography interaction with the formation of the rARSS. Granulometry was applied to measure the nanostructure population distributions on each DOE. The distributed population histograms of the islands on various DOE surfaces showed no significant deviations when compared to rARSS fabricated on the witness optical window. The observed differences in the cumulative granule distributions of islands and voids imply dependence of the rARSS formation on the phase surface topography. Even though large differences were not observed in the distributed feature histograms, a noticeable difference in the average lateral feature size of voids on control the angle diffuser and Fresnel lens was measured compared to other phase diffusing DOE.

To fully characterize the scatter properties of rARSS, the bidirectional scattering distribution function of optical quality windows, and near-wavelength period gratings was also measured. Although non-deterministic scatter was not observed for rARSS fabricated on DOE, a uniform scatter intensity of about an order-of-magnitude increase was observed for both optical windows and gratings with rARSS compared to the originals. The

measured non-deterministic scatter because of rARSS was found to be negligible and did not affect the optical performance of under underlying optical element they are applied on.

The results presented in this chapter suggest that the rARSS fabrication process designed for an optically flat substrate is transferable to a variety of existing DOE with complex topographies, successfully suppressing Fresnel reflections without compromising their original functionality. A 10^{-6} measurable increase in angular scatter per steradian results at off-design directions.

CHAPTER 4: CONCLUSIONS

4.1 Numerical study of feature-distribution effects for anti-reflection structured surfaces on binary gratings

In this work, the effects of transverse feature distributions of the ARSS on their anti-reflective performance were investigated. A 50% duty cycle baseline binary-phase grating was used as the platform for the AR nanostructures in the numerical experiment. For the study, ordered ARSS and pseudo-randomly distributed ARSS (Dammann grating profiles) were used as transmission enhancers, and were categorized using their surface feature autocorrelation length. The ordered and re-distributed features within the periodic unit cell of the ARSS had comparable fill fractions, guided by EMT design requirements. The depth of ARSS was restricted to a quarter-wave of the incident wavelength at normal angle of incidence, to analyze the effects due to the feature distributions independent of other parameters. The goal was to show if the AR narrow-band performance of the baseline grating was perturbed by the presence of the ARSS.

The results from the numerical experiment show that ARSS with distributed features can result in suppression of Fresnel reflections, with excellent AR performance, as their unit cell periods are reduced from near-wavelength to subwavelength scales. Perturbation effects on the directed transmission power distribution and an increase in scatter resulted because of cross-coupling between the ARSS and the binary baseline grating. This effect was very prominent for trials of single phase-transition AR-SWG with large correlation lengths. In contrast, deterministically re-distributed feature AR-gratings with shorter correlation lengths, were observed to preserve the baseline grating directed transmitted power distributions and had reduced scatter.

Cooperative scattering along the axial direction from the AR-grating profiles, effectively reduces the electromagnetic impedance discontinuity at the optical boundary, with direct correlation to feature distributions. This is shown by the performance of high rank Dammann AR-gratings with shorter correlation lengths, resulting in more stable and consistent results. The cooperative scattering effect was observed to be supported by wavefront simulations using rigorous coupled wave analysis. The wavefront simulations near the optical surface showed high intensity localization for single phase transition periodic AR-gratings, because of the superposition of transmitted and reflected waves at the boundary for both polarization states. However, re-distributed features within a spatial period of ARSS were able to delocalize the energy without perturbing the baseline grating performance because of better impedance match.

In conclusion, ARSS with complicated re-distributed features within their periodic unit cells, and shorter autocorrelation lengths, show better overall anti-reflective performance compared to simple feature distributions with comparable effective permittivity values within the AR-layer.

4.2 Investigation of the optical performance of anti-reflection random nanostructures on diffractive optical elements

The rARSS fabrication process optimized for fused silica windows was applied to prefabricated phase-diffusing diffractive optical elements (DOE), to test if it can be transferable without optimization, and act as effective anti-reflection treatment for segmented three-dimensional-phase surface topographies. For this study four different DOE were chosen, a 2D spot array generator, a 1D spot array generator, a controlled angle

illumination diffuser and a diffractive lens with varying surface feature sizes and distributions. The rARSS were fabricated on the surface of the DOE using a two-step process, firstly a discontinuous layer of gold was deposited which acted as a seed layer to initiate the random etch, followed by dry reactive-ion etching of the substrate under a directional RF field. The measured top-down SEM micrographs verified the formation of rARSS on all-phase levels of the DOE, without modifying their surface phase topography because of the subtractive fabrication process.

The DOE spot-array generators and the controlled-angle diffuser were tested using a scatterometer at 633nm, over the entire equatorial plane of transmission. Deviations from their original design projection pattern due to the presence of rARSS were measured. The measured integrated wide-angle deterministic scatter intensities for the three DOE showed an order of magnitude in suppression of reflectivity, and half-an-order of magnitude in enhancement in the transmission half-space. In contrast to wide-angle deterministic scatter for transmission, a discrepancy was observed in the measured deterministic design spot scatter. A decrease in intensity was noted for the 1D spot array while an enhancement in transmission was seen for the 2D spot array and controlled angle diffuser.

Since the observed suppression in reflectivity did not result in an equivalent transmission enhancement, the DOE were analyzed for any detectable addition of non-deterministic scatter due to the presence of the rARSS. Although differences in their designed illumination patterns post-fabrication of the rARSS were observed, no distinguishable non-deterministic scatter amplification was observed. The main effect was an increase in the non-uniformity for the 1D spot array, and an increase in the axial 0^{th} diffraction order for the controlled angle diffuser.

The diffractive lens transmission and reflection power measurements pre- and post-fabrication of the rARSS showed comparable results to the rest of the DOE, with a significant suppression in reflection and no enhancement in transmission for any of the tested wavelengths. The measured beam profiles have remained near identical with no observable deviations for all measured wavelengths, indicating the transverse high-spatial frequency zones of the lens were not affected by the fabrication of rARSS. These observations suggest that the imbalances in the design illumination patterns of the measured DOE post-fabrication of the rARSS were because of relative phase depth mismatches, induced by the subtractive nature of the etching process that affected their diffractive efficiencies.

Granulometry was used to measure population distributions of the islands and voids, to characterize the rARSS formation on the dissimilar surface topographies of the DOE tested. While the distributed histograms of the islands for all the DOE were observed to be identical to the rARSS fabricated on planar optical windows, differences in the distributed histograms of voids for the DOE was seen. These differences in the distribution of islands to voids signify a possible impact of surface topography on the formation of rARSS.

Finally, to fully characterize the scattering properties of the rARSS, scatter distribution functions of the optical flats and near wavelength gratings, with and without rARSS, were measured. A uniform scatter intensity of about an order of magnitude for higher angles of collection was observed for both measured optical flats and gratings. Even though the detectable scatter for the samples with the rARSS was observed, the effects were found to be minimal at an absolute level of 10^{-6} Watts per steradian, and did not affect the performance of the optical elements they were applied on.

4.3 Potential future work

The work presented in this dissertation has shown that redistributions and randomization of the nanoscale features of AR-structures can enhance their anti-reflective performance, and can also be applied to pre-existing optical components with complex surface topographies without negatively affecting their performance. This outcome is critical for the design and implementation of a variety of optical elements, indicating that numerical designs and fabrication processes don't have to be exhaustive from the onset. It also indicates that existing un-coated (or unstructured) optical components can be readily processed with rARSS, without loss of functionality. Although the experimental results presented in this dissertation show the scatter effects due to the addition of rARSS were negligible for substrates with low optical index values, such as fused silica, slight inefficiency in their performance could lead to addition of significant scatter into an optical system for substrates with large optical index values. As discussed in the chapters, Both EMT and existing scatter models are limited in their function, and fail to completely explain the full effects of nanoscale rARSS on optical surfaces. A comprehensive model including anti-reflectivity properties of the rARSS with their scatter characteristics, could provide further insights, conceptualizing the electromagnetic interactions between structured surfaces and incident optical radiation, and assist in performance optimization for a variety of applications.

REFERENCES

[1] T. Aytug et al., "Monolithic graded-refractive-index glass-based antireflective coatings: broadband/omnidirectional light harvesting and self-cleaning characteristics," Journal of Materials Chemistry C, vol. 3, no. 21, pp. 5440-5449, 2015.

[2] D. Chen, "Anti-reflection (AR) coatings made by sol–gel processes: a review," Solar Energy Materials and Solar Cells, vol. 68, no. 3-4, pp. 313-336, 2001.

[3] S. Chattopadhyay, Y.-F. Huang, Y.-J. Jen, A. Ganguly, K. Chen, and L. Chen, "Anti-reflecting and photonic nanostructures," Materials Science and Engineering: R: Reports, vol. 69, no. 1-3, pp. 1-35, 2010.

[4] A. Thelen, Design of Optical Interference Coatings. New York: McGraw-Hill Book Company, 1989.

[5] Q. Yang, X. A. Zhang, A. Bagal, W. Guo, and C.-H. Chang, "Antireflection effects at nanostructured material interfaces and the suppression of thin-film interference," Nanotechnology, vol. 24, no. 23, p. 235202, 2013.

[6] U. Schulz, F. Rickelt, H. Ludwig, P. Munzert, and N. Kaiser, "Gradient index antireflection coatings on glass containing plasma-etched organic layers," Optical Materials Express, vol. 5, no. 6, pp. 1259-1265, 2015.

[7] D. H. Raguin and G. M. Morris, "Antireflection structured surfaces for the infrared spectral region," Applied optics, vol. 32, no. 7, pp. 1154-1167, 1993.

[8] D. H. Raguin and G. M. Morris, "Analysis of antireflection-structured surfaces with continuous one-dimensional surface profiles," Applied Optics, vol. 32, no. 14, pp. 2582-2598, 1993.

[9] E. B. Grann, M. Moharam, and D. A. Pommet, "Optimal design for antireflective tapered two-dimensional subwavelength grating structures," JOSA A, vol. 12, no. 2, pp. 333-339, 1995.

[10] H. Kikuta, Y. Ohira, H. Kubo, and K. Iwata, "Effective medium theory of two-dimensional subwavelength gratings in the non-quasi-static limit," JOSA A, vol. 15, no. 6, pp. 1577-1585, 1998.

[11] D. S. Hobbs, B. D. MacLeod, and J. R. Riccobono, "Update on the development of high performance anti-reflecting surface relief micro-structures," in Window and Dome Technologies and Materials X, 2007, vol. 6545: SPIE, pp. 242-255.

[12] G. Sapkota et al., "Characterization of random anti-reflecting surface structures and their polarization response at off-normal angles of incidence," in Nanoengineering: Fabrication, Properties, Optics, and Devices XIII, 2016, vol. 9927: SPIE, pp. 154-161.

[13] A. Peltier, G. Sapkota, J. R. Case, and M. K. Poutous, "Polarization insensitive performance of randomly structured antireflecting planar surfaces," Optical Engineering, vol. 57, no. 3, pp. 037109-037109, 2018.

[14] D. S. Hobbs and B. D. MacLeod, "Design, fabrication, and measured performance of anti-reflecting surface textures in infrared transmitting materials," in Window and Dome Technologies and Materials IX, 2005, vol. 5786: SPIE, pp. 349-364.

[15] P. Lalanne and G. M. Morris, "Design, fabrication, and characterization of subwavelength periodic structures for semiconductor antireflection coating in the visible domain," in Developments in Optical Component Coatings, 1996, vol. 2776: SPIE, pp. 300-309.

[16] S.-Y. Han, B. K. Paul, and C.-h. Chang, "Nanostructured ZnO as biomimetic anti-reflective coatings on textured silicon using a continuous solution process," Journal of Materials Chemistry, vol. 22, no. 43, pp. 22906-22912, 2012.

[17] Z.-P. Yang, L. Ci, J. A. Bur, S.-Y. Lin, and P. M. Ajayan, "Experimental observation of an extremely dark material made by a low-density nanotube array," Nano letters, vol. 8, no. 2, pp. 446-451, 2008.

[18] J. J. Steele and M. J. Brett, "Nanostructure engineering in porous columnar thin films: recent advances," Journal of Materials Science: Materials in Electronics, vol. 18, pp. 367-379, 2007.

[19] C. Cardinaud, M.-C. Peignon, and P.-Y. Tessier, "Plasma etching: principles, mechanisms, application to micro-and nano-technologies," Applied Surface Science, vol. 164, no. 1-4, pp. 72-83, 2000.

[20] D. J. Economou, "Modeling and simulation of plasma etching reactors for microelectronics," Thin Solid Films, vol. 365, no. 2, pp. 348-367, 2000.

[21] R. Hsiao and J. Carr, "Si/SiO2 etching in high density SF6/CHF3/O2 plasma," Materials science and Engineering B, vol. 52, pp. 63-77, March 6, 1998.

[22] M. Schaepkens and G. S. Oehrlein, "A Review of SiO2 etching studies in inductively coupled fluorocarbon plasmas," Journal of The Electrochemical Society, vol. 148, pp. C211-C221, March 1, 2001.

[23] B. Zollars et al., "Performance measurements of infrared windows with surface structures providing broadband wide-angle antireflective properties," in Window and Dome Technologies and Materials XIII, 2013, vol. 8708: SPIE, pp. 158-172.

[24] N. Roxhed, P. Griss, and G. Stemme, "A method for tapered deep reactive ion etching using a modified Bosch process," Journal of Micromechanics and Microengineering, vol. 17, no. 5, p. 1087, 2007.

[25] D. S. Hobbs and B. D. MacLeod, "High laser damage threshold surface relief micro-structures for anti-reflection applications," in Proc. SPIE, 2007, p. 67200L.

[26] L. E. Busse, C. M. Florea, J. A. Frantz, L. B. Shaw, I. D. Aggarwal, M. K. Poutous, et al., "Anti-reflective surface structures for spinel ceramics and fused 108 silica windows, lenses and optical fibers," Optical Materials Express, vol. 4, pp. 2504-2515, 2014.

[27] J. Zhao, H. Qi, H. Wang, H. He, and W. Zhang, "Scattering analysis for random antireflective structures on fused silica in the ultraviolet," Optics Letters, vol. 40, no. 22, pp. 5168-5171, 2015.

[28] C. Taylor, K. J. Major, R. Joshi, L. E. Busse, J. Frantz, J. S. Sanghera, et al., "Optical performance of random anti-reflection structures on curved surfaces," 2015, pp. 935916-935916-8.

[29] C. Taylor, L. Busse, J. Frantz, J. Sanghera, I. Aggarwal, and M. Poutous, "Angle-of-incidence performance of random anti-reflection structures on curved surfaces," Applied optics, vol. 55, no. 9, pp. 2203-2213, 2016.

[30] C. Taylor, "Optical Performance of Random Anti-Reflection Structured Surfaces (rARSS) on Spherical Lenses," Ph.D dissertation, College of Eng. and Sc., University of North Carolina Charlotte, Charlotte, 2016.

[31] A. Peltier, "Optical performance of random antireflection sstructured surfaces on non-vitreous substrates and fused silica microlens arrays," Ph.D dissertation, College of Eng. and Sc., University of North Carolina Charlotte, Charlotte, 2018.

[32] K. Kunala and M. K. Poutous, "Diffraction efficiency performance of random anti-reflecting subwavelength surface structures on prefabricated fused silica binary gratings," Applied optics, vol. 57, no. 16, pp. 4421-4427, 2018.

[33] K. Kunala, "Optical performance of random antireflection sstructured surfaces on optical flats and diffractive components," Ph.D dissertation, College of Eng. and Sc., University of North Carolina Charlotte, Charlotte, 2018.

[34] L. De Sio et al., "Beam shaping diffractive wave plates," Applied optics, vol. 57, no. 1, pp. A118-A121, 2018.

[35] M. D. Himel, M. K. Poutous, J. D. Stack, and J. L. Leonard, "Microfabrication of controlled angle diffusers used for resolution enhancement in microlithography," in Micromachining Technology for Micro-Optics and Nano-Optics, 2003, vol. 4984: SPIE, pp. 230-233.

[36] J. Elam, D. Routkevitch, P. Mardilovich, and S. George, "Conformal coating on ultrahigh-aspect-ratio nanopores of anodic alumina by atomic layer deposition," Chemistry of materials, vol. 15, no. 18, pp. 3507-3517, 2003.

[37] T. Alasaarela et al., "Atomic layer deposited titanium dioxide and its application in resonant waveguide grating," Applied optics, vol. 49, no. 22, pp. 4321-4325, 2010.

[38] T. Weber, T. Käsebier, A. Szeghalmi, M. Knez, E.-B. Kley, and A. Tünnermann, "High aspect ratio deep UV wire grid polarizer fabricated by double patterning," Microelectronic engineering, vol. 98, pp. 433-435, 2012.

[39] H. Shimomura, Z. Gemici, R. E. Cohen, and M. F. Rubner, "Layer-by-layer-assembled high-performance broadband antireflection coatings," ACS applied materials & interfaces, vol. 2, no. 3, pp. 813-820, 2010.

[40] H. Shimomura, Z. Gemici, R. E. Cohen, and M. F. Rubner, "Layer-by-layer-assembled high-performance broadband antireflection coatings," ACS applied materials & interfaces, vol. 2, no. 3, pp. 813-820, 2010.

[41] N. Selvakumar and H. C. Barshilia, "Review of physical vapor deposited (PVD) spectrally selective coatings for mid-and high-temperature solar thermal applications," Solar energy materials and solar cells, vol. 98, pp. 1-23, 2012.

[42] C.-H. Chang, J. A. Dominguez-Caballero, H. J. Choi, and G. Barbastathis, "Nanostructured gradient-index antireflection diffractive optics," Optics letters, vol. 36, no. 12, pp. 2354-2356, 2011.

[43] E. R. Dougherty and R. A. Lotufo, Hands-on morphological image processing. SPIE press, 2003.

[44] M. Moharam and T. Gaylord, "Rigorous coupled-wave analysis of planar-grating diffraction," JOSA, vol. 71, no. 7, pp. 811-818, 1981.

[45] E. Zuazua, "Propagation, observation, and control of waves approximated by finite difference methods," SIAM review, vol. 47, no. 2, pp. 197-243, 2005.

[46] J. C. Stover, "Optical scattering. Measurement and analysis," SPIE Press Volume, 1995.

[47] P. Beckmann and A. Spizzichino, "The scattering of electromagnetic waves from rough surfaces," Norwood, 1987.

[48] S. Schröder, A. Duparré, L. Coriand, A. Tünnermann, D. H. Penalver, and J. E. Harvey, "Modeling of light scattering in different regimes of surface roughness," Optics express, vol. 19, no. 10, pp. 9820-9835, 2011.

[49] S. Rytov, "Electromagnetic properties of a finely stratified medium," Soviet Physics JEPT, vol. 2, pp. 466-475, 1956.

[50] C. Zhou and L. Liu, "Numerical study of Dammann array illuminators," Applied optics, vol. 34, no. 26, pp. 5961-5969, 1995.

[51] H. Zou, W. H. Zhu, J. F. Gong, K. X. Zhang, and H. Y. Xie, "The Study of Various Dammann Grating," in 2010 Symposium on Photonics and Optoelectronics, 19-21 June 2010 2010, pp. 1-4, doi: 10.1109/SOPO.2010.5504438.

[52] J. Jahns, M. M. Downs, M. Prise, N. Streibi, and S. J. Walker, "Dammann gratings for laser beam shaping," Optical Engineering, vol. 28, no. 12, pp. 1267-1275, 1989.

[53] J. N. Mait, "Design of binary-phase and multiphase Fourier gratings for array generation," J. Opt. Soc. Am. A, vol. 7, no. 8, pp. 1514-1528, 1990/08/01 1990, doi: 10.1364/JOSAA.7.001514.

[54] C. Pacholski et al., "Antireflective subwavelength structures on microlens arrays—comparison of various manufacturing techniques," Applied optics, vol. 51, no. 1, pp. 8-14, 2012.

[55] T. Yanagishita, K. Nishio, and H. Masuda, "Anti-reflection structures on lenses by nanoimprinting using ordered anodic porous alumina," Applied physics express, vol. 2, no. 2, p. 022001, 2009.

[56] S. S. Oh, C.-G. Choi, and Y.-S. Kim, "Fabrication of micro-lens arrays with moth-eye antireflective nanostructures using thermal imprinting process," Microelectronic Engineering, vol. 87, no. 11, pp. 2328-2331, 2010.

[57] P.-Y. Baroni et al., "Nanostructured surface fabricated by laser interference lithography to attenuate the reflectivity of microlens arrays," Journal of the European Optical Society-Rapid Publications, vol. 5, 2010.

[58] P.-L. Chen, R.-H. Hong, and S.-Y. Yang, "Hot-rolled embossing of microlens arrays with antireflective nanostructures on optical glass," Journal of Micromechanics and Microengineering, vol. 25, p. 095001, 2015.

[59] H. Jung and K.-H. Jeong, "Monolithic polymer microlens arrays with antireflective nanostructures," Applied Physics Letters, vol. 101, p. 4, 2012.

[60] X. Ye et al., "Formation of broadband antireflective and superhydrophilic subwavelength structures on fused silica using one-step self-masking reactive ion etching," Scientific reports, vol. 5, no. 1, p. 13023, 2015.

[61] S. D. Mellin and G. P. Nordin, "Limits of scalar diffraction theory and an iterative angular spectrum algorithm for finite aperture diffractive optical element design," Optics Express, vol. 8, no. 13, pp. 705-722, 2001.

[62] X. Tan, B.-Y. Gu, G.-Z. Yang, and B.-Z. Dong, "Diffractive phase elements for beam shaping: a new design method," Applied optics, vol. 34, no. 8, pp. 1314-1320, 1995.

[63] J. E. Harvey, "Understanding Surface Scatter: A Linear Systems Formulation," 2019: SPIE/International Society for Optical Engineering.

[64] R. Noll, "Effect of Mid- and High-Spatial Frequencies on Optical Performance," Optical Engineering, vol. 18, no. 2, p. 182137, 1979.

[65] D. M. Aikens, J. E. DeGroote, and R. N. Youngworth, "Specification and control of mid-spatial frequency wavefront errors in optical systems," in Optical Fabrication and Testing, 2008: Optica Publishing Group, p. OTuA1.

[66] P. Gadamsetti, K. Kunala, and M. K. Poutous, "Optical scattering measurements of random anti-reflection subwavelength surface structures on binary gratings," in Optical Components and Materials XVII, 2020, vol. 11276: SPIE, pp. 216-223.

APPENDIX A: Publications & Conference proceedings

[1] **P. Gadamsetti**, K. Kunala, and M. K. Poutous, "Optical Scattering of Deterministic Diffractive Elements with Antireflective Structured Surfaces," in 2019 IEEE 16th International Conference on Smart Cities: Improving Quality of Life Using ICT & IoT and AI (HONET-ICT), 2019: IEEE, pp. 223-225.

[2] **P. Gadamsetti**, K. Kunala, and M. K. Poutous, "Optical scattering measurements of random anti-reflection subwavelength surface structures on binary gratings," in Optical Components and Materials XVII, 2020, vol. 11276: SPIE, pp. 216-223.

[3] **P. Gadamsetti**, K. Kunala, and M. K. Poutous, "Random anti-reflection subwavelength surface structures on deterministic illumination diffusers," in Photonic and Phononic Properties of Engineered Nanostructures XI, 2021, vol. 11694: SPIE, pp. 23-28.

[4] **P. Gadamsetti**, M. E. Testorf, P. Batoni, and M. K. Poutous, "Optical super-resolving phase filters with random anti-reflection subwavelength surface structures," in Optical Components and Materials XVIII, 2021, vol. 11682: SPIE, pp. 159-166.

[5] **P. Gadamsetti**, M. Testorf, D. A. Gonzalez, P. Batoni, and M. K. Poutous, "Implementation of a superresolution far-field spot-generator with 1/5 the diffraction limit," Results in Optics, vol. 3, p. 100067, 2021.

[6] D. A. Gonzalez, K. Vijayraghavan, **P. Gadamsetti**, and M. K. Poutous, "Optical surface absolute specular reflectance measurement using an infrared etalon and interferometer combination method," in Photonic Instrumentation Engineering IX, 2022, vol. 12008: SPIE, pp. 75-84.

[7] M.K. Poutous, H. Cai and **P. Gadamsetti**, “Non-Linear Optical crystal with Anti-reflective nanostructured surface”. U.S. Patent Application US2022004080A1 (Jan 2022).

[8] **P. Gadamsetti** and M. K. Poutous, "Fresnel reflection suppression from deterministic illumination diffusers using antireflection random nanostructures," Optical Engineering, vol. 61, no. 6, pp. 063106-063106, 2022.

[9] **P. Gadamsetti** and M. K. Poutous, "Comparison between effective-medium and structure-distribution models for antireflective nanostructures on functional diffractive optics," in Optical Components and Materials XX, 2023, vol. 12417: SPIE, pp. 77-87.

[10] **P. Gadamsetti** and M. K. Poutous, “Numerical study of feature-distribution effects for anti-reflection structured surfaces on binary gratings”. (Applied optics, Accepted – March 2023)

APPENDIX B: List of Optical Components

Thorlabs Components

Component	Model	Quantity
Photodiode Power Sensor	S120C	1
Power Meter Console	PM100A	1
Graduate Ring-Actuated Iris Diaphragm	SM1D12C	1
Dual Scanning Slit Beam Profiler	BP209-IR	1
CCD camera Beam Profiler	BC106N-VIS	1
Continuously variable ND filter	NDC-100C	1

Other Components

Component	Model	Quantity
Tunable Helium-Neon (He-Ne) Laser	R-30602/R-30603	1